Hearing Through Haptics:
A Planar, Audio-spatial Awareness Device

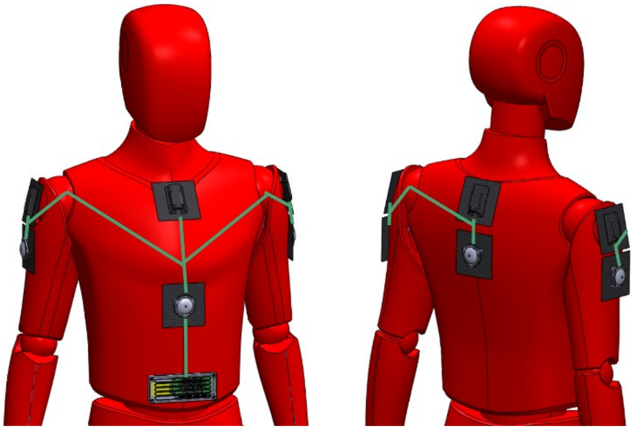

A Major Qualifying Project Report submitted to the Faculty of the
WORCESTER POLYTECHNIC INSTITUTE
in partial fulfillment of the requirements for the Degree of Bachelor of Science

Submitted By:

Colin Ancalmo

Amani Campbell

Yifan Liu

James Van Tronk

Emily Wood

Advised by and Submitted to: Professor Joe Stabile
DEPARTMENT OF MECHANICAL ENGINEERING
May 18, 2020

Abstract

The Deaf and Hard of Hearing community faces challenges identifying audio-based safety and social alerts. Existing options for assistive devices for the hearing-impaired are limited, often costly, dependent on the condition of the auditory vestibular nerve, and can involve invasive procedures. The goal of this project is to develop a portable, planar and non-invasive wearable device that is independent of the vestibular nerve and does not inhibit user behavior. Haptic technology has the capability to bypass mechanisms of traditional hearing for increased assistive accessibility. The device is intended to provide audio-spatial awareness by using haptic vibrations for sensory substitution to sense urgent safety alerts (i.e. alarms, sirens) and social interaction cues. Using three-dimensional arrangements of actuator and microphone pairs and input signal filtering through a microcontroller, sound sources can be identified and directionally located, indicated to the user via actuator vibrations.

Acknowledgements

First, we would like to thank our advisor, Professor Joe Stabile for providing guidance and resources for this project and allowing us the freedom to explore this new territory.

We would like to thank Mitra Anand, the Foisie Innovation Studio Makerspace Technician, who guided us in the 3D printing, laser cutting, and PCB fabrication processes in the initial stages of our project to choose the appropriate materials and techniques.

We would like to thank Ian Alexander Gallo Anderson, the Senior Instructional Lab Technician in Washburn Shops, for his invaluable advice on how to fabricate our planar spring and Dan Sheehan and Carl Kallgren of Bose Corporation for manufacturing these parts on our behalf.

We would also like to sincerely thank Electrical and Computer Engineering students, Tahvorn George and Fivos Kavassalis for their wealth of knowledge, assistance, and guidance in the electrical aspects of our project. Tahvorn George contributed to the Appendix I section of this report. Finally, we would like to thank Barbara Furham for helping us with purchasing parts for this project.

Table of Contents

List of Figures

List of Tables

1.0 Introduction

Currently there are an estimated 466 million people with disabling hearing loss worldwide, which is expected to increase up to 900 million by 2050 (World Health Organization [WHO], 2020). The Deaf and Hard of Hearing (DHH) face daily challenges with interacting and reacting to their environment. Engaging in social conversations, recognizing safety alerts such as car honks, ambulance sirens, fire alarms, traditional alarm clocks; these are all forms of audio-based communication that the DHH community struggles to identifying.

Currently, there are hearing-assistive devices like hearing aids and cochlear implants that are capable of addressing most cases of hearing loss. These devices however are often costly, not covered by most medical insurances in the US, and can involve invasive medical procedures (Jackson, Wegner & Turnbull, 2010). Because of this, only 17% of the DHH community has access to the existing technologies that can aid them, leaving 83% in need of a new aid solution (WHO, 2020). Additionally, both hearing aids and cochlear implants rely on a functioning audio vestibular nerve within the inner ear, offering no aid to those born with a damaged vestibular nerve.

The objective of this Major Qualifying Project was to research and develop new forms of assistive hearing technology to increase aid accessibility to the 83% still in need. The result was an audio-spatial haptic array integrated within a wearable planar shirt device. This team identified haptic technology for its capability of circumventing traditional mechanisms of hearing. Multiple actuator technologies were investigated and analyzed for wearable haptic applications, followed by the design and fabrication of a small-footprint low-profile actuator. A microphone array was created to identify two primary sound types; 1) Urgent Safety Alerts and

2) Social Cues and Interactions. By using the microphone inputs, audio data was then analyzed to determine sound directionality, mapping directly to an array of planar haptic actuators.

2.0 Background

This background section presents an overview of Deafness and Hard of Hearing and a review of traditional and innovative auditory assistive devices. Haptic technology is then analyzed as a mode of communication, followed by types of haptic actuation and audio sensing.

2.1. Deaf and Hard of Hearing

Hearing loss has many causes, levels of severity, and methods to aid those suffering from it. First, types of hearing loss can describe its severity, how it was acquired, and other circumstances related to how it impacts the person. The four main types of hearing loss are conductive, sensorineural, mixed, and auditory neuropathy spectrum disorder. Conductive hearing loss is caused by sounds being prevented from getting through the outer or middle ear. This type of hearing loss can typically be treated with medicine or surgery. Sensorineural hearing loss occurs when the inner ear or hearing nerve becomes damaged. Mixed hearing loss involves a combination of both conductive and sensorineural. Finally, auditory neuropathy disorder occurs due to damage to the inner ear or hearing nerve that prevents them from organizing sound input into something the brain can understand (Center for Disease Control and Prevention [CDC], 2019).

Severity of hearing loss is categorized into four categories, ranging from mild to profound. People with mild hearing loss can hear most sounds but may have trouble hearing sounds below 40 dB (WHO, 2020). Meanwhile, people suffering from profound hearing loss can hear only the loudest of sounds (CDC, 2019).

Table 1: Examples of dB Sound Pressure Levels (European Commission, 2008)

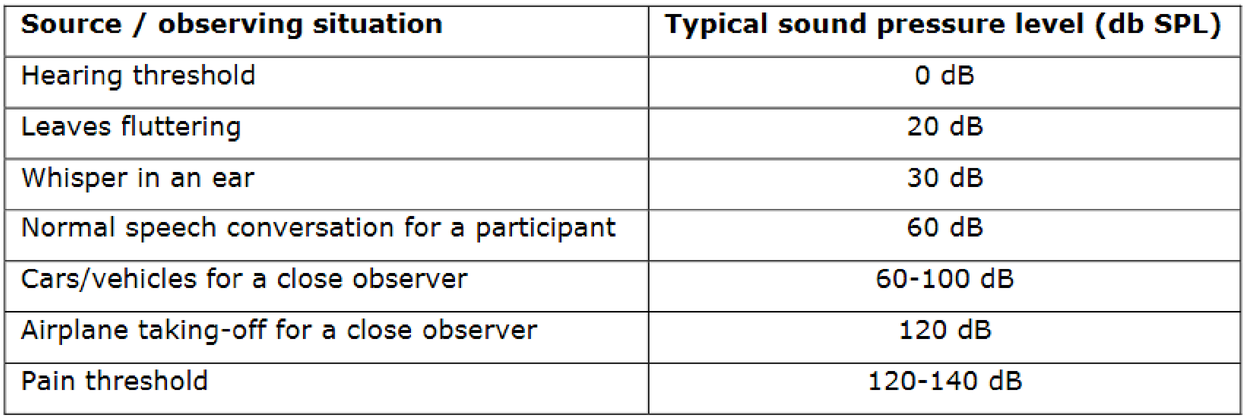

Source / observing situation	Typical sound pressure level (db SPL)
Hearing threshold	0 dB
Leaves fluttering	20 dB
Whisper in an ear	30 dB
Normal speech conversation for a participant	60 dB
Cars/vehicles for a close observer	60-100 dB
Airplane taking-off for a close observer	120 dB
Pain threshold	120-140 dB

Hearing loss has many causes. Congenital hearing loss is present at birth and can be caused by genetics. Other hearing loss can be acquired throughout life through various means either suddenly or over a long period of time. Causes of sudden hearing loss can include traumatic brain injury, exposure to extremely loud sounds, and autoimmune diseases, among others. Progressive hearing loss occurs over a long period of time, and gradually worsens over time. One common cause of progressive hearing loss is constant exposure to loud noises. This type of hearing loss is typically painless and occurs over years of exposure (CDC, 2019). The most common cause of sensorineural hearing loss is Presbycusis, which is most commonly associated with aging. This type of hearing loss occurs as the inner ear changes (loss of hair cells in the ear, or diminished blood flow to the ears are common causes) as the person ages, specifically due to gradual loud noises. Typically, Presbycusis affects the ability to hear higher pitched sounds. For example, while a person may have trouble hearing a higher-pitched voice, they may have no trouble at all hearing a deeper voice of the same amplitude. Presbycusis often occurs so slowly that victims often are unaware that their hearing is diminishing. About 30-35% of people 65 and older have hearing loss, while 40-50% of people 75 and older have hearing loss (National Institute of Deafness and Other Communication, 1987).

It is widely accepted that hearing loss and deafness can have significant effects on the physical and psychosocial health of those suffering. In turn, hearing loss could drastically impact the overall quality of life of individuals. The Journal of Communication Disorders conducted a 2019 focus group study where Deaf and Hard of Hearing (DHH) people defined quality of life and the impact of hearing disorders on their quality of life. Particularly, their main qualms involved a feeling of social isolation from societal and familial interactions. They also expressed general health concerns due to a lack of an essential sensory system. This can impact both physical and mental health (Hitt et al., 2019). Furthermore, it is important to note the importance of assistive devices for the DHH community. The study also explored the priorities of those suffering from hearing loss. Current attempts to aid hearing loss depend on several factors, such as the wearer's severity of hearing loss, linguistic abilities, and therapy to learn the sense of hearing. Additionally, the survey ranked the importance of several different hearing cues that DHH patients often missed. First among them was urgent alerts such as alarms, horns, etc. that may alert them of danger. The next most important was voices directed at the patient (Findlater, Chinh, Jain, et al., 2019). A graph of the rankings is shown below.

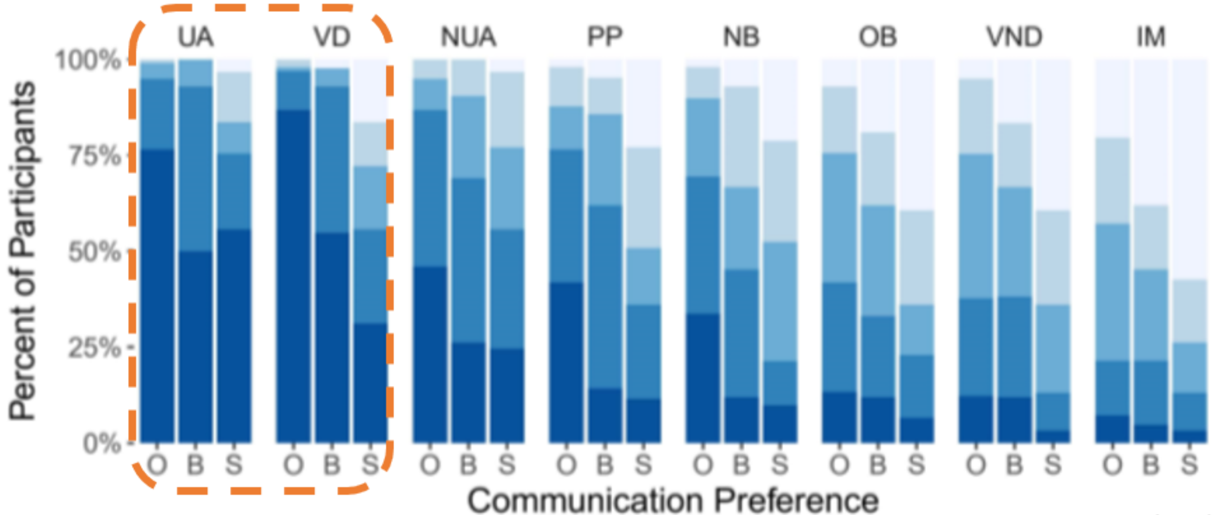

User Communication
Preferences
O – oral
B – both
S – sign

(a) Sound Categories

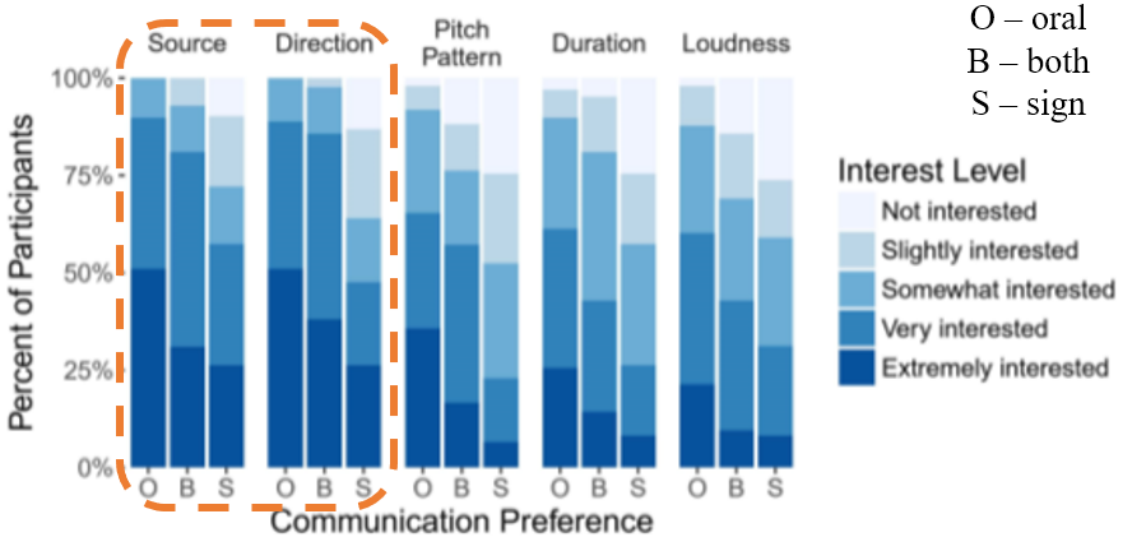

(b) Sound Characteristics

Figure 1: Journal of Communication Disorders study excerpt (Findlater et al., 2019)
Highest sound categories: UA = Urgent Alerts, VD = Voices directed at you; Highest sound characteristics: Source, Direction

Another key point in the study is that many current DHH communication strategies heavily rely on visual cues such as body language, facial expressions, or hand motions such as sign language. This makes is extremely important for DHH patients to be able to see where a sound stimulus is coming from, so they can locate the stimulus visually in a social situation.

2.2. Assistive Devices

The following section highlights assistive devices, both traditional and more innovative, their function, capabilities, and limitations.

2.2.1. Current (Traditional) Assistive Devices

Assistive devices for the Deaf and Hard of Hearing have existed for over a century, known as Hearing Assistive Technologies or HATS (Atcherson et al., 2015). The most common wearable HATS are hearing aids and cochlear implants. Hearing aids function by magnifying sounds that enter the ear (NIDCD, 2017). When sound enters the ear as vibrations against hair cells the vestibulocochlear nerve, or "hearing nerve," converts and sends these vibrations as signals from the inner ear to the brain. The more damage there is to hair cells, the more vibrations need to be amplified in order to be perceived. Hearing aids are limited by the condition of a patient's ear, they cannot counteract damage to the vestibulocochlear nerve or extensive loss of hair cells (National Research Council (US) Committee on Disability Determination for Individuals with Hearing Impairments. 2004).

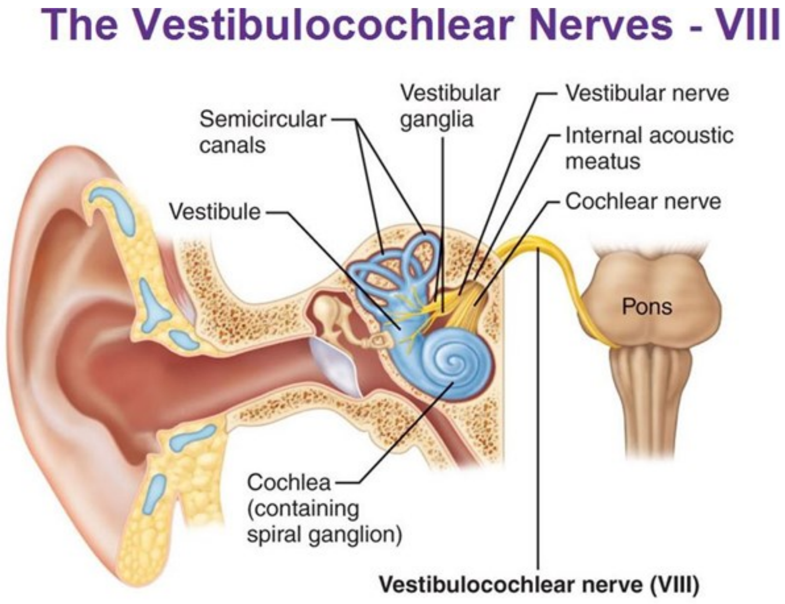

Figure 2: Vestibulocochlear "Hearing" Nerve

Cochlear implants function by directly stimulating the vestibulocochlear nerve, creating signals that the brain perceives as sound (NIDCD, 2017). For people who are almost or completely deaf in both ears, cochlear implants are necessary. However, this does not mean that they are a viable option for everyone. Like hearing aids, cochlear implants depend on the vestibulocochlear nerve being intact.

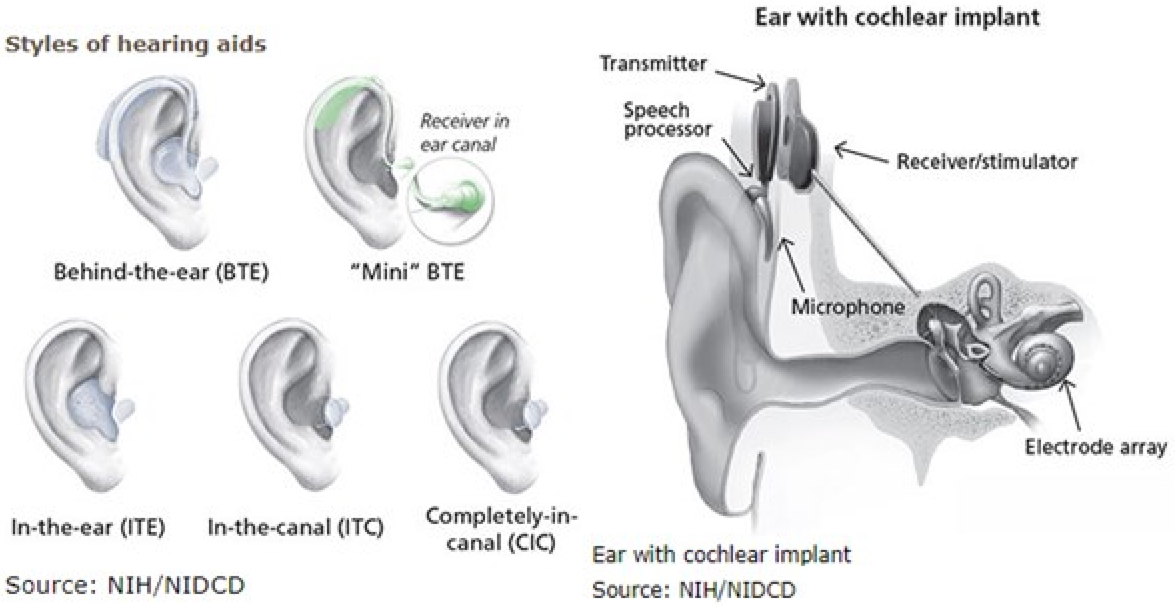

Source: NIH/NIDCD

Ear with cochlear implant
Source: NIH/NIDCD

Figure 3: Hearing Aid and Cochlear Implant Diagram.

Both of these devices are expensive, and in the case of cochlear implants require surgery to install. Hearing aids range from $40 to over $6,000 depending on the lifespan, strength and whether the user needs aids for both ears (Mroz, 2019). After being fitted with HATS, patients can expect follow-up appointments to adjust device fit and for cleanings. The majority of the expenses associated with hearing aids generally are not covered by health insurance. Cochlear implants can cost between $30,000 and $50,000; most commercial health care plans cover cochlear implants, and as of 2004 so do Medicare, Medicaid, and the Veteran's Administration (UCSF Health, 2020). For people who are uninsured, cochlear implants are a major expense. A 2004 report from the FLHSA Deaf Health Task Force on Rochester, NY's Deaf and Hard of

Hearing population, in order to better understand the demographics of the national hearing impaired population, found that 13% of the population was only covered by public health insurance programs. What expenses public programs such as Medicaid will cover varies from state to state. Medicare does not cover hearing aids or exams to fit them, while Medicaid may provide coverage (De Pietro, 2020).

Our team identified a need for a low-cost, low-profile wearable device to provide spatial audio awareness. A wearable haptic device is non-invasive and more affordable than an implant, and once purchased the user should be able to maintain and clean the device on their own. By providing spatial awareness through real-time haptic feedback, the device does not depend on the condition of the vestibulocochlear nerve.

2.2.2. State of the Art Assistive Technologies

NeoSensory is a wearable device developed by neuroscientists to ‘build a non-invasive brain-machine’ that translates environmental noises as touch to gain a sense of awareness. The company’s main focus, according to their website, is ‘sending data streams to the brain via touch’ and is based on the principle of experiencing reality ‘beyond our sensory limitations.’ The wearable device, that closely resembles a wristwatch, captures sounds such as alarm clocks, doorbells, music, dogs barking, voices, laughter, a family member entering the room, a friend calling your name etc. and translates that into vibrations. Another function of the device is to provide a safe environment for the user by detecting emergency sounds such as smoke alarms, sirens, and cars honking (NeoSensory.com, 2016).

While the company does not specify a target group, it appears to be a device that can be optimized by the DHH community and other individuals with impairments but not strictly for this community. Through the testimonials on their website, consumers are able to understand if there is noise in the environment, whether it be a kettle whistling or someone shouting, however, they are not able to accurately discern what the source of the sound is.

Another assistive device the team discovered was Watch IT. It is intended for the deaf and hearing impaired to bridge the gaps in communication and education. It functions by receiving the voice, processing it, and outputting it as a readable text on an LCD screen. Because this device utilizes sight instead of touch to display sounds, it can only display two lines up to sixteen characters each, which does not seem practical for long nor quick speeches especially since the paper lacks research on the response time. It requires a watch and an Android phone in particular to operate and may be biased in the speech recognition technology (Mahamud & Zishan, 2017). There is also no function stated in the paper that indicates how the device operates in emergency situations or how it is capable of recognizing and discerning different urgent safety alerts to alert the user.

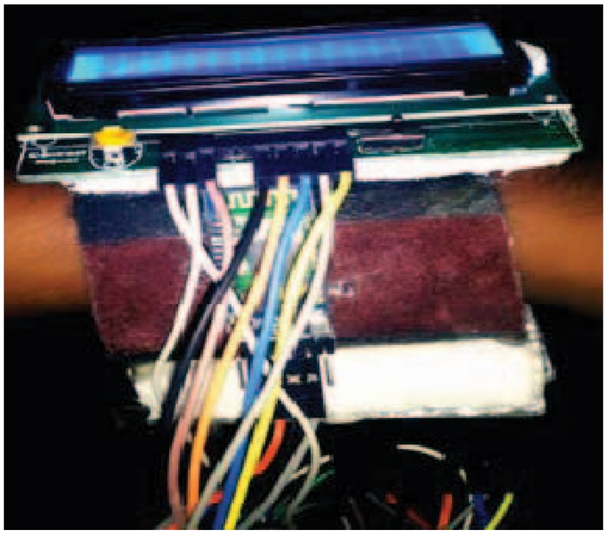

Figure 4: Watch IT prototype technology (Mahamud & Zishan, 2017)

2.3. Haptics and Haptic Actuators

The following section describes the motivations behind haptic technology and methods to evaluate their effectiveness in communicating information. Traditional haptic motors are then highlighted and compared to emerging forms of smart actuator technologies for their haptic potential.

2.3.1. Haptic Technology – Literature Review

Haptic feedback utilizes a user's sense of touch and applied oscillating forces to create a felt response. The field of haptics first arose in the 1950s as a form of control feedback for teleoperation, the remote operation of advanced machinery (Goertz, 1952). Within the last ten years, haptics has grown into a multidisciplinary field covering control systems, robotics, psychology, and neuroscience (Frisoli & Ryu, 2012). This physical form of feedback has been incorporated into consumer devices ranging from mobile phones to alarm clocks to game controllers (Frisoli & Ryu, 2012). When delving into more advanced haptic applications involved in robot-to-human interactions however, the effectiveness of certain haptic implementations come into question. For this, the team looked to the purpose of haptic systems and the advantages they offer.

The primary function of Haptics is transmitting information through the sense of touch. The type of information varies based on the application. A user may want a notification of an incoming mobile phone call without audio disruption, A machine operator may require a feedback once a tool piece has reached its target, or a military drone pilot may need an instant interpretation of a drone's pitch, yaw, and roll. (Frisoli & Ryu, 2012; Eagleman, 2015). Each example requires different information configurations; On/Off, proximity, and 3-degree variables as examples, respectively. Haptic technologies can accommodate multitudes of information types and can often transmit such data more effectively that traditional audio-visual counterparts (Eid & Al Osman, 2015; Massie & Salisbury, 1994). As the complexity of the transmitted information increases however, the haptic device's degrees of freedom must too increase to remain effective (Hoffmann, Spagnol, Kristjánsson, & Unnthorsson, 2018; Eid & Al Osman, 2015).

The most effective modes of haptic information transfer are primarily via the magnitude, direction, overall motion, and duration of the vibration (Eid & Al Osman, 2015; Massie & Salisbury, 1994). While the use of these parameters is critical, a common critique in existing assistive haptic devices is a complexity mismatch in the inputted information and outputted user feedback. This issue was highlighted during an evaluation of a haptic assistive device for the visually impaired in 2018. The design used audio-haptic cues in efforts to substitute a user's sense of sight. The device imprinted a head-mounted camera's image tactically onto a head-mounted haptic motor matrix, with the addition of audio cues for proximity sensing (Hoffmann et. al, 2018). Testing showed the system to improve the obstacle awareness of hard-of-sight subjects. When discussing limitations and improvements for the design, it is noted that the haptic system "*may not have the required spatiotemporal resolution necessary to convey sufficient information*", with emphasis for touch-related applications (Hoffmann et al., 2018). The visual input information from the camera is limited by the 6 by 10 haptic grid output. Additionally, users showed difficulty detecting dynamic objects. While a 3D camera setup was utilized, additional information is lost projecting data onto a 2D haptic arrangement as the audio output sampled a central point depth (Hoffmann et al., 2018). Recommending improvements included a higher resolution haptic surface to better reflect the camera's resolution. From this, the team observes that haptic systems may be more intuitive and effective when the inputs and outputs share greater similarity and synergism.

To enhance haptic sensing, it is also critical to consider the operation frequencies of the driving haptic mechanism. Within human skin, there are two primary nerve groups with higher responses to tactile vibration. These groups: the Meissner corpuscles and the Pacinian corpuscles, each react non-linearly to vibration frequencies between 5 to 180 Hz and 40 to 800 Hz respectively (De Rossi, 2011). Existing research has been done to determine the cumulative peak tactile response in this multi-mode nerve system. Within the lens of haptic notifications for smartphones for bodies in motion (i.e. walking, running), an ideal haptic operation frequency range is between 160 to 250 Hz (Baek, Myung, & Yim, 2006; Yim, Myung, & Lee, 2007). Note however that this range varies in literature based on the application area and operation conditions.

2.3.2. Traditional and Smart Material Actuation

Next, the team looked at the common mechanisms driving haptic motion in consumer products, as well as alternative modes of planar actuation. Most mobile phones and gaming controllers use compact actuators based on wire and magnet-based to achieve 1-DOF oscillating motion. Specific configurations include Eccentric Rotating Mass vibration motors (ERMs), commonly used in game controllers and older “pager” phones, and Linear Rail Actuators (LRAs), found more in recent smartphones. ERMs rely on a DC motor to move an off-center mass, while LRAs use magnetic Lorentz force to linearly oscillate wires or magnets. (Precision Microdrives, 2015). Both ERMs and LRAs fall under the category of Coil and Magnet-based Actuators. They consist of two primary components: A Stator, a non-moving electromechanical component that induces alternating magnetic fields, and a Rotor, a moving component with a magnetic core or field winding that interact the stator’s fields to create forces. While magnet and coil actuators are widespread in their uses and applications, other actuator configurations exist that use smart materials to generate displacement and forces.

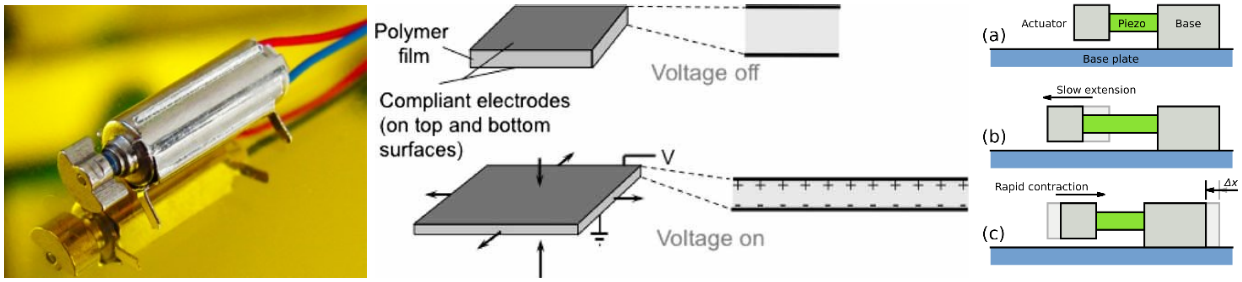

a) ERM Coil & Magnet Actuator b) Dielectric Elastomers (DEAs) c) Piezoelectric Actuators

Figure 5: Types of Actuator Systems (Microdrives, 2015; Brochu, 2009; Gorissen et al, 2014)

Here, the team investigated Dielectric Elastomers (DEAs) and Inverse Piezoelectric Actuators for planar haptic applications. Dielectric Elastomers (DEAs), also known as Electroactive Polymers (EAPs), are built using the principle of a flexible dielectric capacitor laminate. Two electrode layers enclose a central dielectric material. As a large voltage is applied to one electrode, the two electrode layers are attracted to each other causing the dielectric layer to expand in the planar axis (Brochu, 2009; De Rossi, 2011). With techniques such as pre-strain, certain acrylic dielectrics can withstand maximum strains of up to 380% (Brochu, 2009). This planar expansion can then be used to create out-of-plane deflection with the use of kinematic springs. The electrode-dielectric layers themselves are flexible, making them suitable for wearable applications. DEAs however have limited frequency response ranges and the voltages required to induce their extreme strains range from 500 to 10,000 Volts (Brochu, 2009; De Rossi, 2011). Having kilovolts of energy in a wearable device presents the possibility of electrocution from improper protection. This high voltage risk has been addressed in prior works such as a 2011 article from the IEEE Medicine and Biology Society, presenting designs that utilize a hydrostatic isolation layer and localized DC/DC High-Voltage converters at the location of each actuator (Brochu, 2009).

Inverse Piezoelectric actuators are another form of smart actuator, using piezoelectric material structures to convert electricity into mechanical displacement. By flowing high voltages through crystalline structures, the atoms contract and expand. Conversely, applying displacement on the crystal produces voltage. Piezoelectric materials are most used in sensors where planar force measurement is required. Compared to traditional actuators, inverse piezoelectric actuators are capable at applying extremely high pressures at high frequencies. This is done however with a reduced maximum strain, limiting the magnitude of actuator displacement (Brochu, 2009; Gorissen et al, 2014).

2.4. Actuator Input

The following section displays research on sound characteristics of emergency sirens such as the frequency range and sound pressure level, and the effective range for an auditory warning signal. This section also discusses the most effective way to input these signals, process and filter them and output the correct feedback in accordance to the distinct warning signals.

2.4.1 Urgent Safety Alerts

For this report, the team decided to focus on emergency sirens as the main urgent safety alert for the system to detect. The most common siren signals are in the form of a 'Wail' or 'Yelp.' However, both signals have different features such as the range of frequencies and their corresponding amplitudes regarding sound. The 'Wail' is commonly seen at over a period of 4.11s at a sound pressure of 130dB, whereas the 'Yelp' is commonly seen over a period of 0.35s at a sound pressure of 130dB. Both sirens operate within the frequency range of 725Hz and 1600Hz with the exception of the 'Yelp', which may go up to 2000Hz with the Rumbler configurations (Angione, Novak, & Imeson et al., 2016). The average sound pressure of ‘noise’ in urban environments is around 60dB (Madden, et al, 2011). An auditory warning signal of 130dB in a noise-rich environment is effective within the range of 8-12m (Skeiber, et al, 1978). Understanding these characteristics of these signals will allow the team to design a system that is capable of accurately filtering out unwanted frequencies and noise in the user’s environment and responding only to auditory warning signals to stimulate improved awareness in the user.

2.4.2. Frequency to Voltage Conversion

For the sensing part of this project, converting frequencies to certain voltage levels allows the input frequencies to be connected directly with the actuator response.

The team began research by looking at various LED music visualizer projects, in which Devon Crawford’s LED music visualizer project stood out. It utilizes frequency to voltage conversion to convert the audio volume to LEDs’ brightness. It also picks up pitch and converts that to the RGB colors of the LEDs. Arduino is used for the processing of signals. With the aim to filter out certain frequencies to trigger the actuators, a frequency to voltage conversion could benefit the project.

In one simple frequency-to-voltage conversion circuit, connections are straightforward, and it converts the input frequency to voltage in a linear manner with an error of only 1.4% (Mathscinotes, 2014). The circuit is shown in Figure 6.

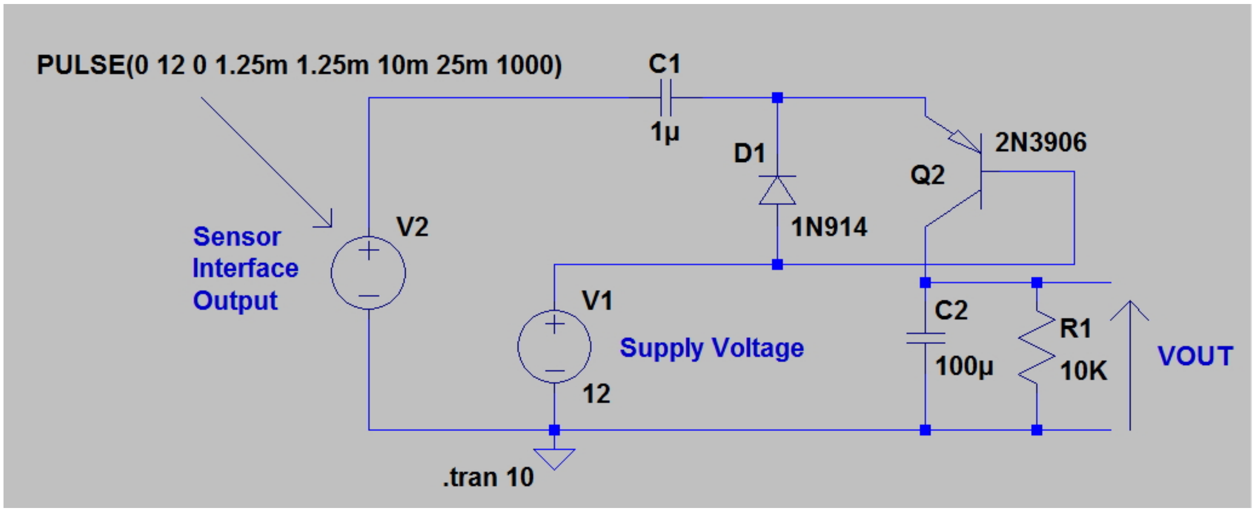

Figure 6: Frequency to Voltage Conversion Circuit (Mathscinotes, 2014)

The testing results show that this circuit converts a bass frequency of around 150 kHz to a voltage of around 5V. It is a great circuit for distinguishing sub bass frequencies, but for the desired application, higher frequencies are also of interest. The team could use the layout of the circuit, but some resistors and capacitors need to be changed in the future.

2.4.3. Microphone Sensing

Directionality is crucial in sound sensing. In this way, the device could inform the user where exactly the sound is coming from. Stereo microphones detect the directionality of sounds, but they are way too bulky for wearable application. An alternative solution is to have an array of mono MEMS microphones all around to each pick up signals.

There are two main types of mono MEMS microphones that could be used for this project's application: analog output and digital output. MEMS microphones with analog outputs allow for a straightforward interface to the host circuit. The analog output signal of the microphone is driven by an amplifier internal to the microphone. Therefore, it is already at a reasonable signal level with a low output impedance. On the other hand, utilizing pulse density modulation (PDM), MEMS microphones with a digital interface is a little more complicated.

With PDM the analog signal voltage is converted into a single bit digital stream containing a corresponding density of logic-high signals. PDM allows for better noise immunity, higher bit error tolerance, and a simpler hardware interface (Mathscinotes, 2014). Analog output has its advantages as well, such as lower power consumption due to the lack of ADC, and they are available in smaller packages than digital microphone. An analog microphone can be in a package with dimensions 2.5 × 3.35 × 0.88 mm or smaller, while PDM microphones often come in a 3 × 4 × 1 mm package, an increase of 62% in package volume. (Lewis, 2013).

3.0 Methodology

This section documents the objectives and scope used during the device design process. The methods used for design analysis, fabrication, and hardware validation are then discussed.

3.1. Design Scope & Ideation

Design goals and Functional Definition

The goal of this project was to develop a non-invasive wearable, planar device to provide sensory substitution through haptic vibrations in order to assist the Deaf and Hard of Hearing in perceiving and identifying the direction of sounds from safety alerts and social interactions. Limitations in current hearing assistive technologies were identified as lack of directionality, high costs, requiring invasive procedures for use, and dependency on the condition of the vestibular (hearing) nerve. In order to design a device that addressed these limitations, the following functional requirements were identified:

1. The device's ability to function is independent of the condition of the vestibular nerve.
2. The device provides a sense of audio spatial awareness, which allows the user to identify the direction a sound is coming from.
3. The device does not inhibit user behavior neither physically nor socially.
4. The device can detect and distinguish urgent safety alerts, and social cues in more noise-controlled environments.
5. The device is designed for daily use.

To fulfill the functional requirements outlined, the following design solutions were specified:

1. Haptics and vibrations generated by an actuator will function as a tactile sensory substitution for hearing.

2. A three-dimensional array of sensory triggers is used to provide directionality to the feedback system.
3. The components are lightweight, low-profile, and contained in a wearable housing.
4. Microphones and a microcontroller are used to input and process sound.
    a. The microphone receives sound data from the microphones and determines whether there is an urgent safety alert or social interaction cue based on the harmonic frequencies and their corresponding amplitudes.
    b. Input received by microphones is compared to determine direction of sound based on the loudest input.
5. The system is comfortable and has a durable construction.
    a. Mechanical components are contained within housings.
    b. Electrical components are contained in housings with no exposed wires.

A wearable device that utilizes haptic vibrations to alert the user to sounds can function independent of the vestibular nerve by relying on the user's sense of touch. The wearable device used a t-shirt design to create a three-dimensional array of microphones and actuators on the user. Four microphones were placed around the collar of the shirt at the front, back and sides to receive sound from multiple directions, and actuators placed on the chest, back, and shoulders of the shirt. To prevent multiple actuators from vibrating at once, the sound signal was processed to identify which microphone received the loudest input to then trigger the corresponding actuator.

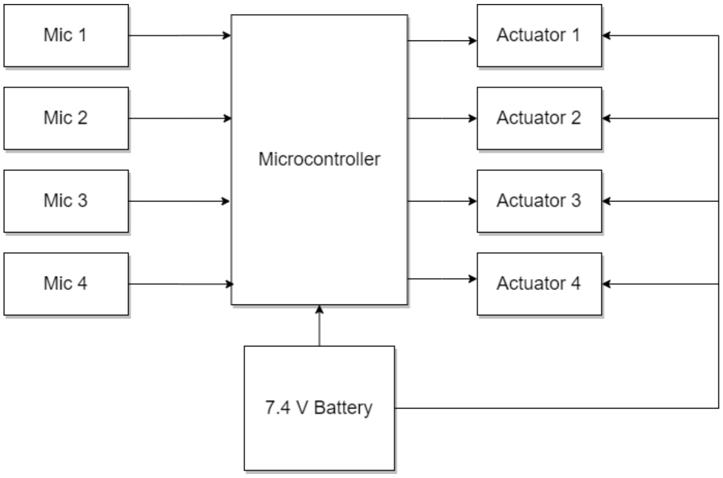

Figure 7: Block Diagram of system

A shirt was used as a base for the wearable in order to place the actuators and microphones around the upper torso, back and shoulders of the user. A common way people get the attention of others is by tapping them on the shoulder, and so the most intuitive placement for the feedback mechanisms is near the shoulders. When someone feels a sudden sensation, their instinct is to look toward the source. Having haptics mimic a familiar social signal that already utilizes the sense of touch will make it easier for new users to acclimate to the device.

Pockets and temporary fasteners were used to attach the components to the shirt. A front zipper pocket at the bottom of the shirt, similar to the ones found on pullover sweaters, held the power supply. Hook-and-loop tape was used to affix the actuators on the shirt. Elastic rings, attached to fabric coverings with a plastic shell inside, were arranged around the shirt collar; the elastic could be lifted to slide the microphones into the shell to hold them in place around the collar. Long hook-and-loop tape strips were used to contain the wiring running along the shirt.

3.2. Analysis Methods

The following software was used to perform preliminary analysis on design performance prior to fabrication.

3.2.1. FEMM and OctaveFEMM

FEMM is a finite element magnetic analysis software that solves axisymmetric 2D electrostatic systems for magnetic parameters including flux and Lorentz force. Working within 2D systems allows for rapid solution results and simple geometric changes. Due to limitations of using Lorentz force, forces are measured on excitation sources rather than permanent magnets. OctaveFEMM is a built-in extension that enables command interactions between MATLAB and FEMM. MATLAB code can be used to generate and define a system’s geometry and properties, as well as record solution parameters. Iterative geometric analysis can be performed with the inclusion of while-loops via this method. This mode of iterative analysis was used in sections 4.1.3 and 5.2.1.

3.2.2. Ansys Structural

Ansys Structural is finite element analysis tool for conducting multiple 2D and 3D structural analyses on imported geometries. The relevant analysis types used in this report include Static Structural for geometry deflection and stress, Modal Analysis for identifying vibrational modes, and Harmonic Response for probed displacements and accelerations across a frequency range.

3.2.3. Ansys Maxwell

Ansys Maxwell is a comprehensive electromagnetic field analysis tool for both 2D and 3D systems. The relevant program solvers used in this report are the magnetostatics solution systems, including permanent magnets and fields from excited electrical wires. Unlike FEMM, Maxwell measures magnetic forces on all system objects including permanent magnets. By defining a solution boundary volume, 3D representations of B and H fields can be generated to better analyze the spatial magnetic behavior surrounding the system.

3.3. Prototype Manufacturing

The following tools were used for the manufacturing of design components.

3.3.1. Prototype Manufacturing: 3D Printing, Laser Cutting, Water cutting

Numerous methods were employed to generate prototype components for the actuators, housings, and manufacturing processes.

The first was 3D printing. Typical 3D printers utilize a gantry system to guide a filament nozzle around a generated tool path as heated filament is dispensed. As the filament cools, it hardens, forming the part. Filament materials used during this MQP included nylon and PLA plastic of various colors. One important aspect of 3D printing is ensuring the tolerances of the particular printer are met. Careful research of the printer's capabilities must be conducted to ensure features can be created by it. Features that are too small will have difficulty printing because the stepper motors driving most printers will not be able to make steps small enough to define the feature, while the filament from the nozzle may have difficulty adhering to a small enough structure. Other key issues include overhang. For example, 3D printers often have difficulty printing without a surface, and as a result parts must be oriented, so that the filament is laid onto a solid surface. Each printer has its own tolerance for overhang, so some is allowable if the filament is being laid onto a slanted surface. The team primarily used the Ultimaker 3 3D printer for most prototyped parts. It had relatively tight tolerances and could handle moderate overhang. Since most of the components used in this project were relatively small, this made the Ultimaker 3 the ideal candidate for the team.

Laser cutting was another major implement for fabricating springs for the actuator. Laser cutting uses a high-power laser combined with a 2D toolpath to cut material from stock. Common laser cutting material includes acrylic, wood and wood derivatives, and various plastics. One major consideration with laser cutting is ensuring that no toxic biproducts are created in the process of cutting material. This becomes especially important when cutting certain types of plastic where cyanide may be produced. Like 3D printing, tolerancing is also a concern. As the power of the laser is increased the tolerance on parts is lowered. Likewise, higher powered lasers can cause burn marks on the material, which may be an aesthetic issue. However, certain power levels of the laser are required to cut through material. Therefore, laser cutting may prove to have several tradeoffs that may need to be considered. Over the course of the project, the team employed two printers: A Full Spectrum P-Series 48x36 Laser Cutter and a Coherent Laser cutter courtesy of Bose in Framingham Massachusetts.

Water cutting is another useful implementation where laser cutting cannot be used. This may be due to material properties or capabilities of the laser. As the name implies, water cutting uses a high-pressure jet of water to slice through material. Water cutting was used to cut spring steel planar springs in place of a laser cutter, which lacked the power to slice the metal. Like laser cutting, the stream of water is a non-zero dimension, so tolerances may become an issue as the jet cuts through the material. Therefore, considerations must be made in the design to allow for some flash from the jet. If the design is too small, the water jet may cut through certain features. Additionally, when water cutting, considerations must be made for proper disposal of wastewater containing scrap swarf. Proper handling of waste is an essential part of this process, like any manufacturing process.

3.3.2. PCB Etcher - LPKF ProtoLaser

The LPKF ProtoLaser S4 is a PCB Etching machine used for creating circuit board connections on single and double-sided copper clad PCB stocks. The machine was investigated and used for its potential for processing the smart material “Pyralux” (AC 352500EY), a flexible copper-clad material with a layer thickness of 60 um. The machine uses UV lasers to etch away the surface coating layer to allow for surface connectivity, the copper layer to separate circuit paths, or grounding layer for board mounting through-holes. Programs such as Eagle CAD are required for creating and programming the etching paths. Due to the micron-level dimension scale between PCB layers, it is critical that the etching material is correctly positioned to micron-level accuracy in the vertical axis, with a uniform material surface height.

Figure 8: LPKF ProtoLaser S4 - PCB Laser Etching

3.4. Test Methods and Validation

The following instruments and methods were used to validate mechanical and electrical designs.

3.4.1. Polytec Scanning Vibrometer (PSV-400)

Vibration testing is important to many fields of product design and engineering, ranging from automotive to acoustics. Vibrometers can be used to sweep for resonant frequencies, find displacements, velocities, and accelerations of components.

Laser scanning vibrometers allow for no-contact analysis of component vibrations. This ensures results are not influenced by any masses that may need to be attached using other analysis methods. Laser scanning vibrometers can be used to sweep across a range of frequencies to find natural frequencies and set to a single frequency to find displacements and velocities at that frequency. The team tested the resonant frequency of planar spring components and compared them to simulated results. This experiment verified whether the developed prototype matched the theoretical design of the device. To test the harmonic response of the planar spring, the team utilized a Polytec Scanning Vibrometer (PSV-400) that swept across a range of frequencies to find resonance frequencies and modes. From there, the team could analyze the motion of the planar spring at desired frequencies.

3.4.2. Instron

Tensile testing is a widely used practice to find the material properties of different samples, allowing engineers to select the optimum material for specific applications, as well as establish a known catalogue of material properties across materials. Typically, a sample of a material is placed in the tensile testing device, and a tensile load is incrementally applied. The sample’s physical response to loads can then be discerned and analyzed. A well-recognized analysis typically found by tensile testing is a stress-strain curve, which analyzes a material's change in stress as it strains or changes in length. An example of a stress-strain curve is shown below.

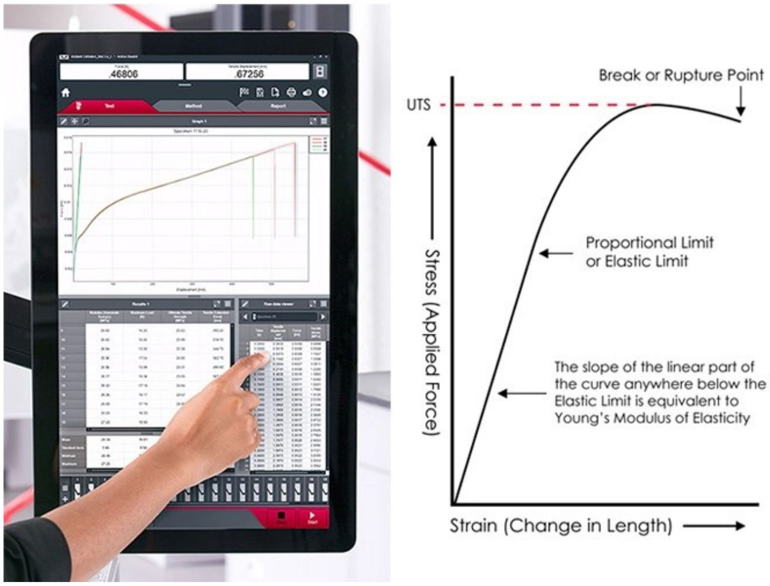

Figure 9: Example of Tensile Tester with Stress-Strain curve, (Instron, 2020)

Since the team was unsure of the true material properties of the planar spring, an Instron tensile testing device was used to find these results. The team intended to use these results to predict why the behavior of the physical planar spring was inconsistent with that of the simulated spring.

3.4.3. Actuator Electrical Characteristics Experiment

The team decided to design an experiment to calculate the impedance of the actuator prototype at resonance frequency as well as measure the current draw in the final circuit design. Another electrical design goal the team discussed was to operate the system at resonance frequency to maximize efficiency. Because the team modeled the actuator design based on an LRA which is a spring-mass system, driving at resonance frequency will result in no wasted energy, and the best vibration and startup performance. As the frequency approaches resonance, as seen in Figure 10, the back EMF and phase of impedance approach maximum inductive reactance (Lewis, 2018). If the frequency varies by a few Hertz from the resonance frequency and the same performance is expected, the mechanical spring force will oppose the magnetic force of the driver and result in wasted energy (Burk, 2013). With a difference of 2.5 Hz from the resonance frequency the vibration performance of the actuator is also compromised by 25% as depicted in Figure 11 (Wang, 2014).

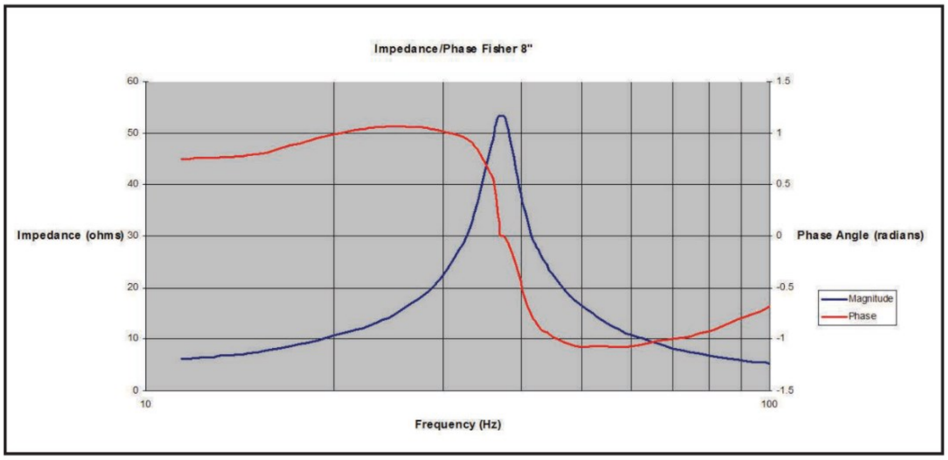

Figure 10: The Impedance Curve of a Fisher Woofer (Lewis, 2018)

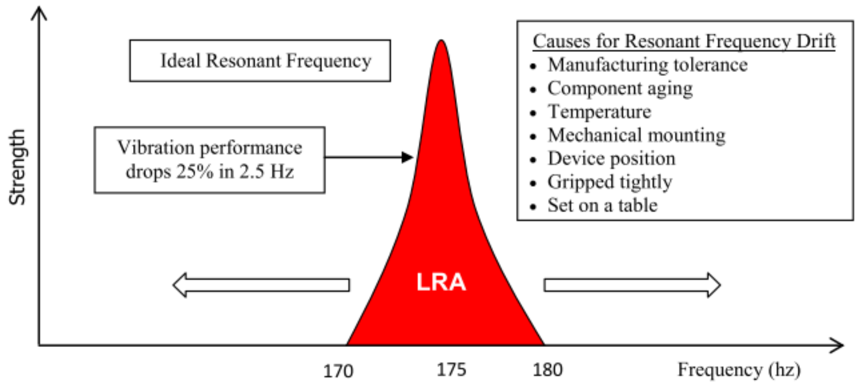

Figure 11: LRA Resonant Frequency Drift (Wang, 2014)

The experiment set-up for the impedance test is depicted in Figure 12. The actuator was connected to a 100 Ω resistor as a reference and a 169 Hz sine wave was the power source from the frequency generator. The governing equation used to calculate the impedance of the actuator is as follows:

$$Z = \frac{V_{A2}}{I} = \frac{V_{A2}}{V_{A1} - V_{A2}} R_{ref}$$

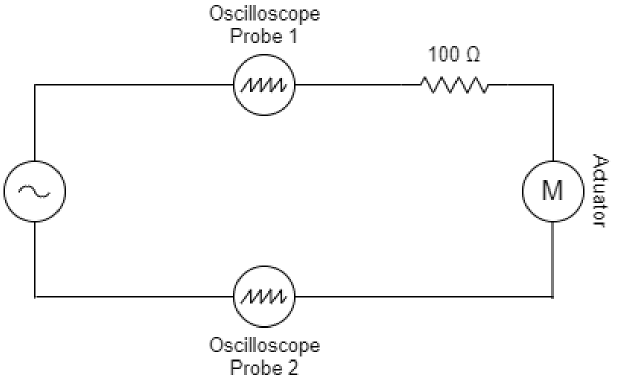

Figure 12: Experimental Setup to Measure the Impedance of the Actuators

In this case, R_{ref} is 100 Ω, V_{A1} is measured from the Pk-Pk value on the oscilloscope for channel 1, and V_{A2} is measured from the Pk-Pk value on the oscilloscope for channel 2. From this same equation, the current consumption of each actuator was determined.

For the second experiment, 7.4 V was supplied to the circuit from the Digital Multimeter (DMM) and the current measured at two instances as depicted below in Figure 13. The current leaving the PWM pins of the microcontroller were measured at point 1 to ensure that the value remained below the 40mA capacity to protect the pins and the current passing through the actuator at point 2 was also measured and recorded. This procedure was to measure the total power consumption of the system as well as the current consumed by the actuator with the intent of making the components and systems more energy efficient.

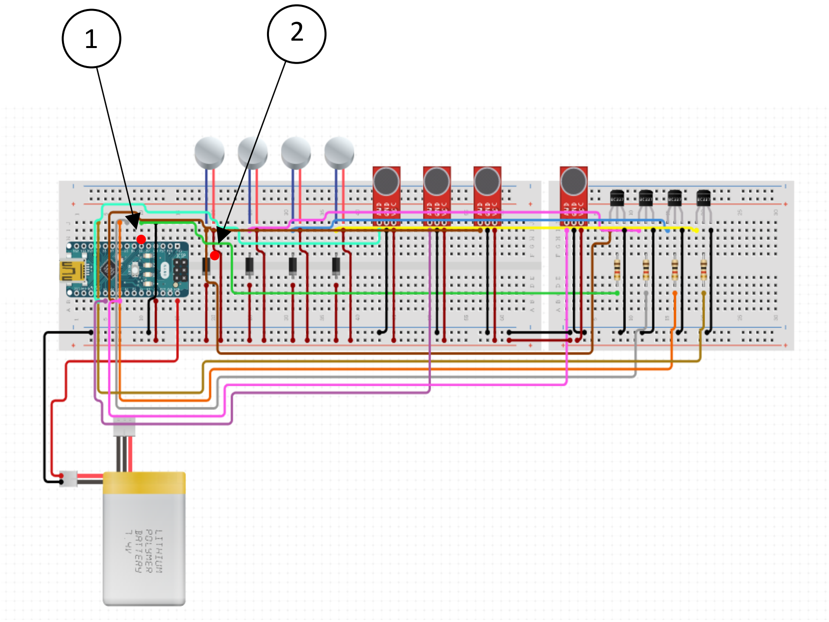

Figure 13: Diagram Depicting the Points of Current Measurement

Note: Each red dot symbolizes one ammeter connected in series at that point in the circuit as explained above.

3.4.4. Microphone Testing

As a control, microphone testing and calibration is normally conducted at a 1kHz sine frequency of 94dB at 1m distance from the sound source. The sound pressure level (SPL) of the room when it was ‘quiet’ was measured and the microphone was connected as shown in Figure 14. A distance of 1m between the receiver (microphone) and the source (dB output) was measured. The circuit was turned on and the MATLAB and Arduino programs, as depicted in Appendix II and III, were run. The team emitted a 1kHz sine signal at 94dB SPL to the receiver and listened for at least 20s. This was conducted as a golden standard to compare the data to the other signal inputs as these are the parameters used to calibrate a microphone.

The Arduino code was reading and writing the microphone readings to the serial port through 5kHz interrupts while the MATLAB code was responsible for reading the serial port and storing the data in order for us to plot and manipulate the data as input for the spectral analysis. This procedure was repeated with the microphone at 45°, 90°,135°, 180°, 225°, 270°, and 315° from the sound source with a 'Wail' and 'Yelp' siren input at 130dB, and white noise at 66dB for distances 5m, 10m, 15m and 20m.

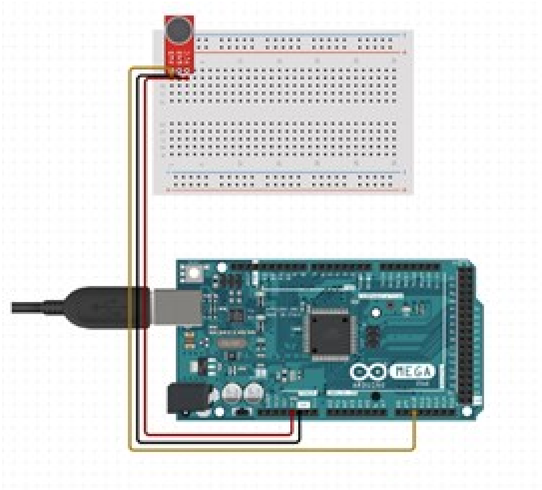

Figure 14: Microphone Test Setup

3.4.5 Spectral Analysis

Once the microphone testing is completed, the spectral analysis can be conducted. The Fourier transform expresses a signal as a superposition of sinusoids as is depicted in Figure 15 (Kulkarni, 2002). The Fourier transform is a great tool to analyze data in the time domain and convert it to the frequency domain.

General Expression for a sinusoid at frequency ω:

$$x(t) = \mathrm{asin}(\omega t + \varphi) = \mathrm{asin}(2\pi f t + \varphi) \ldots (1)$$

where x(t) indicates the changes in air pressure as a function of time.

Fourier Transform equation:

$$\hat{f}(\omega) = \int_{-\infty}^{\infty} f(t)\, e^{-2\pi i\omega t} dt \ldots (2)$$

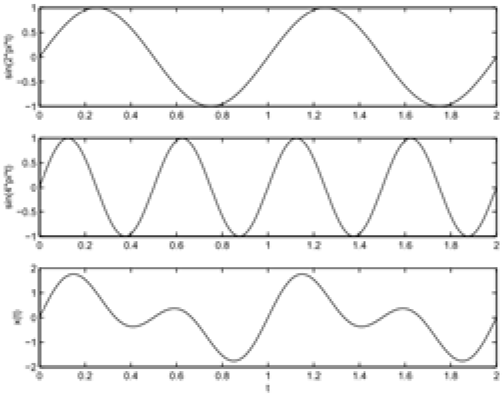

Figure 15: Combining Sinusoids

There are primarily two types of sirens known as the 'Rumbler' and the 'Wail.' The 'Wail siren emits sound in the frequency range from 500Hz to 1600Hz and the 'Rumbler' siren, typically found in the United States, emits sound from 125Hz to 400Hz (Maddern et al., 2011). This 'Rumbler' system in conjunction with a signal input such as a 'Wail' or 'Yelp' is what is typically used. For the purpose of the project and for simplicity, the 'Yelp' signal, with a period of 0.35s and frequency of up to 2kHz is used Figure 16 (Maddern, 2011; Miyazaki, 2013).

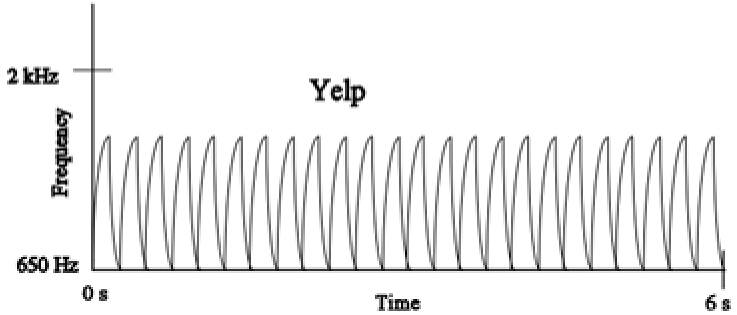

Figure 16: Yelp Waveform with a Cycle Rate of 240 Cycles per Minute

The microphones take the sound input by listening to the varying degrees of air pressure at a given time, but not the decomposition or discrete frequencies from the signal. It is, therefore, important to perform a Fast Fourier Transform FFT on the signal to first decompose the signal.

For this analysis, the team listened to the ‘Yelp’ signal for approximately 5s (4.096s) and performed an 8129-point Discrete Fourier Transform (DFT), which computes the DFT of the function using a Fast Fourier Transform (FFT) algorithm. The two-sided spectrum was first found by dividing each point of the resulting Fourier transform by the length of the signal (8129), and then found its complex magnitude. The single-sided amplitude spectrum was then found by selecting the first 4097 points and multiplied all the points within. Finally, the dominant harmonics (frequencies) were located based on the greater amplitudes. From this it could be determined if a siren had sounded in these 5s if the dominant harmonics are within the expected ‘Yelp’ siren range.

4.0 Design Development.

The following chapter outlines the development of the planar actuator design, and relevant analysis that guided further iterations. From the three actuation mechanisms previously described in section 2.3.2, wire and magnet-based actuators were selected for their design feasibility, performance, and safety. Dielectric Elastomers (DEAs) were not ideal for this design concept, as the plan was to have multiple actuators in different locations, increasing the number of high-voltage converters and safety hydrostatic isolation layers, reducing overall flexibility. Additionally, inverse piezoelectric actuators were not selected for their low displacements and forces at mid-range frequencies (Brochu, 2009).

The first actuator iteration consisted of racetrack-shaped coil windings for planar shear magnetic forces. The second iteration investigated the smart-material Pyralux and laser etching for creating planar high-density coil arrangements. Based on findings from these two iterations, the third iteration implemented planar springs with compact wire-based coil disks.

It is important to note that the magnetic analysis of this chapter required an initial input current. Testing revealed a non-constant current level across different frequencies. A current-to-frequency test was conducted to determine which current value to use for magnetic analysis in FEMM and Ansys Maxwell, the results of which are shown in Figure 17. The measurement setup consisted of the first-iteration actuator coil powered by a mono SparkFun class-D amplifier (TPA2005D1) with a 5.5V source. By sweeping A/C input frequencies between 1-1000 Hz, a maximum measured current of 0.37A occurred between 30Hz - 200Hz. This frequency range included the actuator target operating frequency, thus the following FEMM and Ansys models use an input current of 0.37A unless noted otherwise.

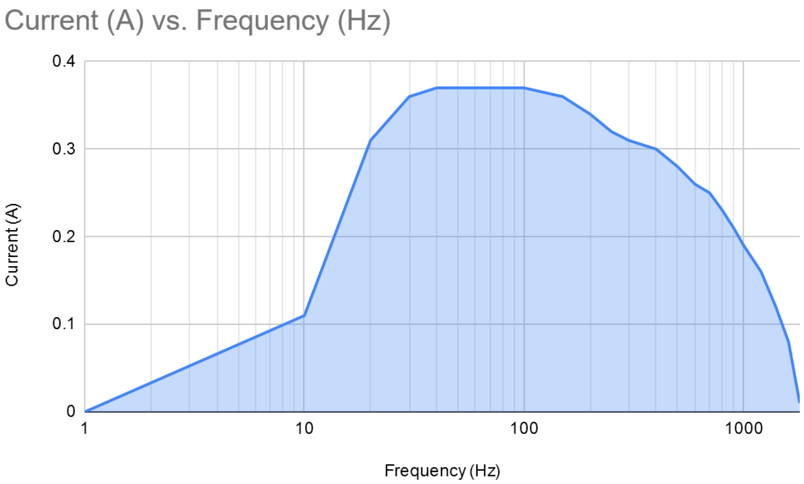

Figure 17: Current vs Frequency for 9v on 30 AWG Wire

4.1. Actuator Hardware Iterations

The following sections details the evolution of the actuator design, relevant magnetic analyses, and prototype fabrications that informed the design decision of the final design discussed in section 5.0.

4.1.1. Iteration 1: Racetrack

The first planar actuator iteration investigates the concept of shear magnetic forces generated between planar magnet and coil layers. Traditional magnet and coil actuators feature a wire voice-coil with magnets located within or surrounding the coils to generate axial forces along the voice-coil. When decreasing a voice-coil's height from a cylinder shell to a ring, axial forces on the moving magnet decrease significantly. An alternative approach used within smartphone haptic components is a two-layer assembly with staggered coils and magnets. The coil layer consists of alternating loops such that one coil creates repelling magnet forces while the other attracts when voltage flows, Figures 18 and 19. By using a racetrack coil shape, inspired by the iPhone 7's "Taptic Engine", the magnitude of the shear forces produced closely match that of planar forces from a non-staggered configuration. (U.S. Patent No. 9396629B1, 2016)

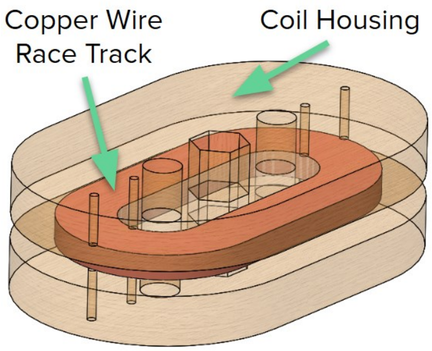

Figure 18: Large Racetrack Coil CAD

The racetrack coil design initially consisted of one individual racetrack, 40mm long by 20mm wide, and a coil-housing 10mm height, containing approximately 190 turns of 30 AWG copper wire. With three 3.2mm cube N40 Magnet, FEMM analysis showed an estimated magnetic shear force of 0.16N when placed above one coil channel.

As actuator height was a key parameter, the overall racetrack dimensions were reduced. By having multiple smaller racetracks within one actuator unit, the shear forces from each could be summed to creating similar forces to that of a larger single counterpart, but in a thinner profile. Racetrack dimensions were halved, resulting in a coil-housing height of 5mm and approximately 72 turns.

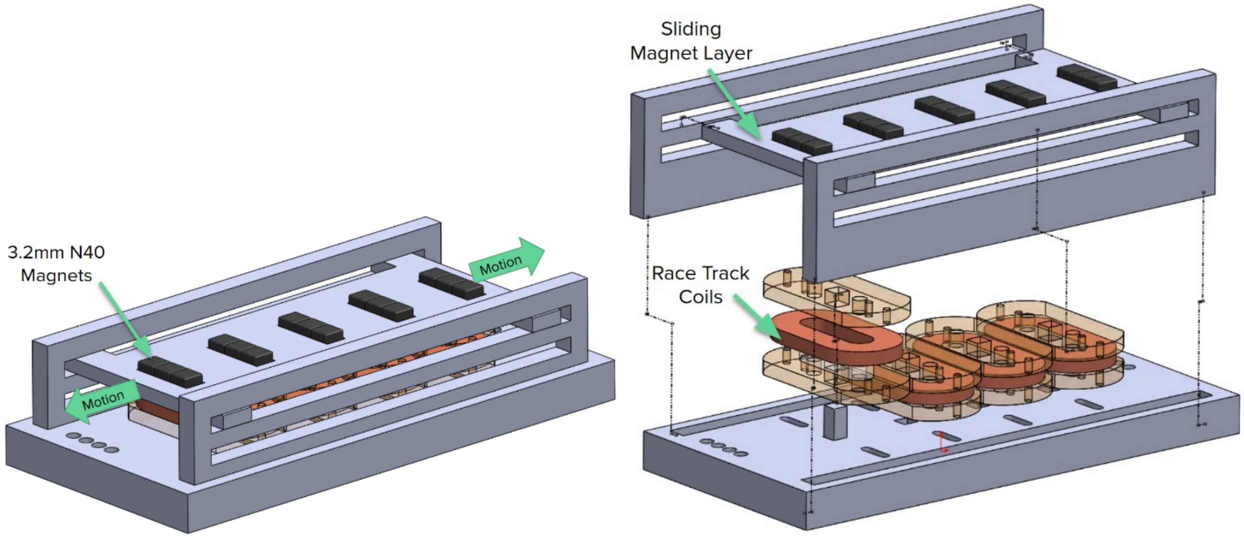

Figure 19: Racetrack Slide Assembly (Shear motion)

With four smaller racetracks placed in series, a summed magnetic shear force of 0.157N could be achieved. Figure 20 shows the magnetic fields created from the alternating loops and

Figure 21 shows the force generated from the 3.2mm cube N40 magnets. A magnet-holding layer allowed the staggered magnets to move as one rigid body, and sliding slots restricted the magnet layer's motion above the assembled racetrack coils, highlighted in Figure 18.

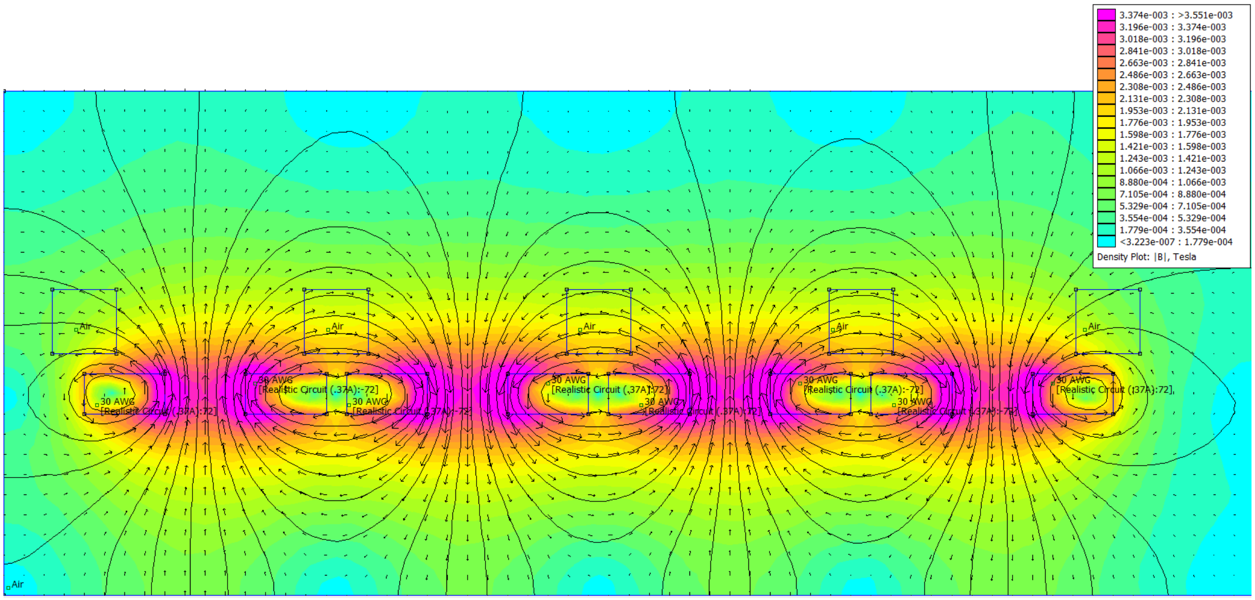

Figure 20: Racetrack FEMM - Coil Magnetic B-Field, No Magnet

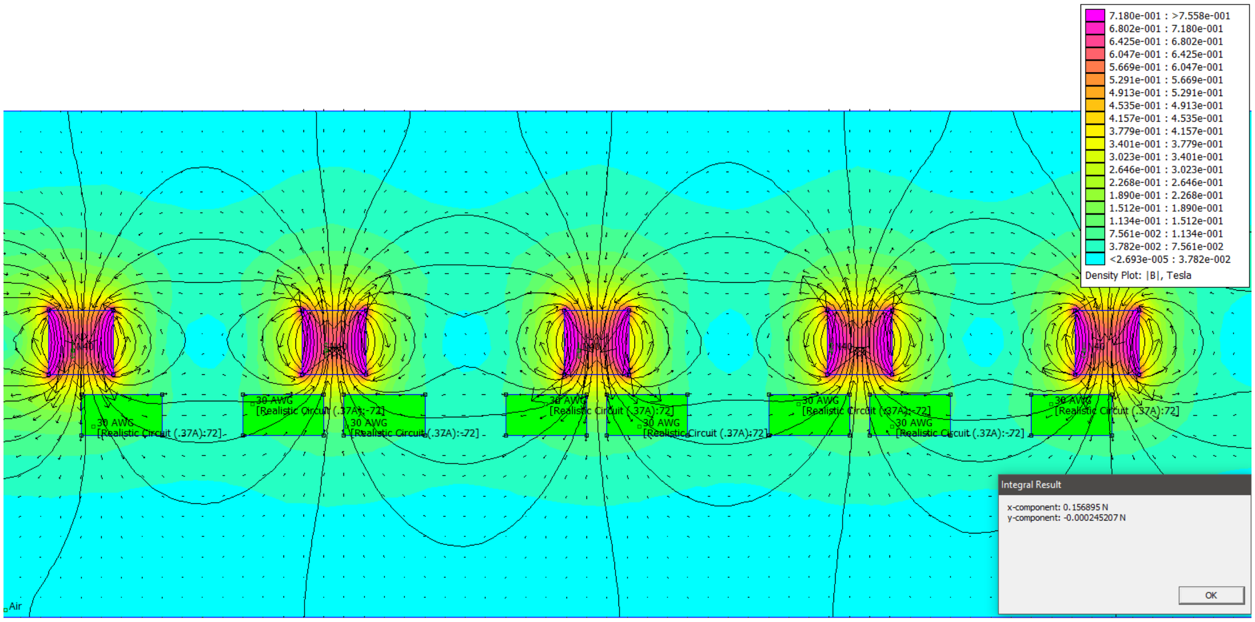

```
x-component: 0.156895 N
y-component: -0.000245207 N
```

Figure 21: Racetrack FEMM - Magnet and Coil Magnetic B-Field

During the fabrication of this iteration prototype, seen in Figure 22, the team encountered multiple issues. Using a Full Spectrum P-Series 48x36 Laser Cutter and Ultimaker 3 3D printers, components showed large dimensional variation due to small feature sizes, tolerance errors, and machine calibration issues. The design faced two additional problems: magnet assembly and overall complexity. Originally each magnet slot would consist of three magnet cubes with the three magnetic north poles all facing upward. The repulsive forces created between magnets in such a position required a change in magnet assembly and fixturing. Using a larger rectangular magnet with a z-axis magnetization would solve this issue, however the team valued having multiple smaller magnets for early prototyping to test different force magnitudes. Additionally, each actuator assembly unit would contain a total of 16 parts, including 4 individually wound racetrack coils. As the wearable design would require four to six actuator units total, it was determined that this design would be less feasible to manufacture. The following iterations looked for solutions with a lower number of parts and smaller assembly height.

Figure 22: Shear Racetrack Fabrication (Right: large coil, Middle and Left: slide framework)

4.1.2. Iteration 2: Flexible Copper-clad - Pyralux

The next iteration the team considered was to use a flexible PCB copper-clad sheet known as Pyralux to mimic physical wire coils. By etching wire paths in the Pyralux sheet, an electric current could theoretically pass through a layer of the sheet to create a magnetic field. By stacking multiple sheets of Pyralux together, a magnetic field could be created with similar strength but in smaller profile. Using FEMM analysis, the team discovered that 8 layers of Pyralux with a 0.37A excitation could produce a force of 0.2N shear horizontal force or 0.1N vertical force, depending on how the magnets were oriented to interface with the sheets. As each Pyralux layer has a 60 µm thickness, the coil height would total 480 µm in ideal conditions. An identical size N40 disc magnet would serve to apply the response force to the magnetic field. This analysis assumed the Pyralux would be etched to the equivalent diameter of 30 AWG wire. The FEMM magnetic analysis is shown below.

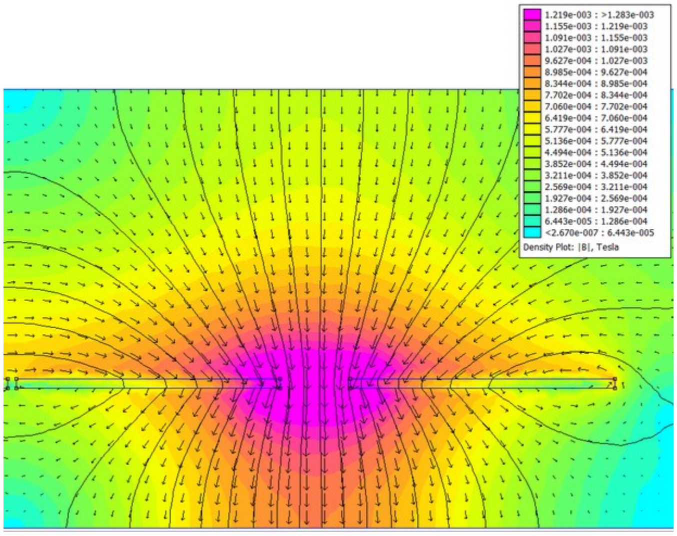

Figure 23: Pyralux Coil Magnetic B-Field Distribution

The team etched the Pyralux material using the LPKF ProtoLaser S4, which is normally used to etch rigid PCB boards. First, a 2D toolpath profile was drafted, then duplicated for 16 instances. This would serve to cut an entire sheet of 6-inch by 6-inch Pyralux with minimal stock material waste. The toolpath is shown below.

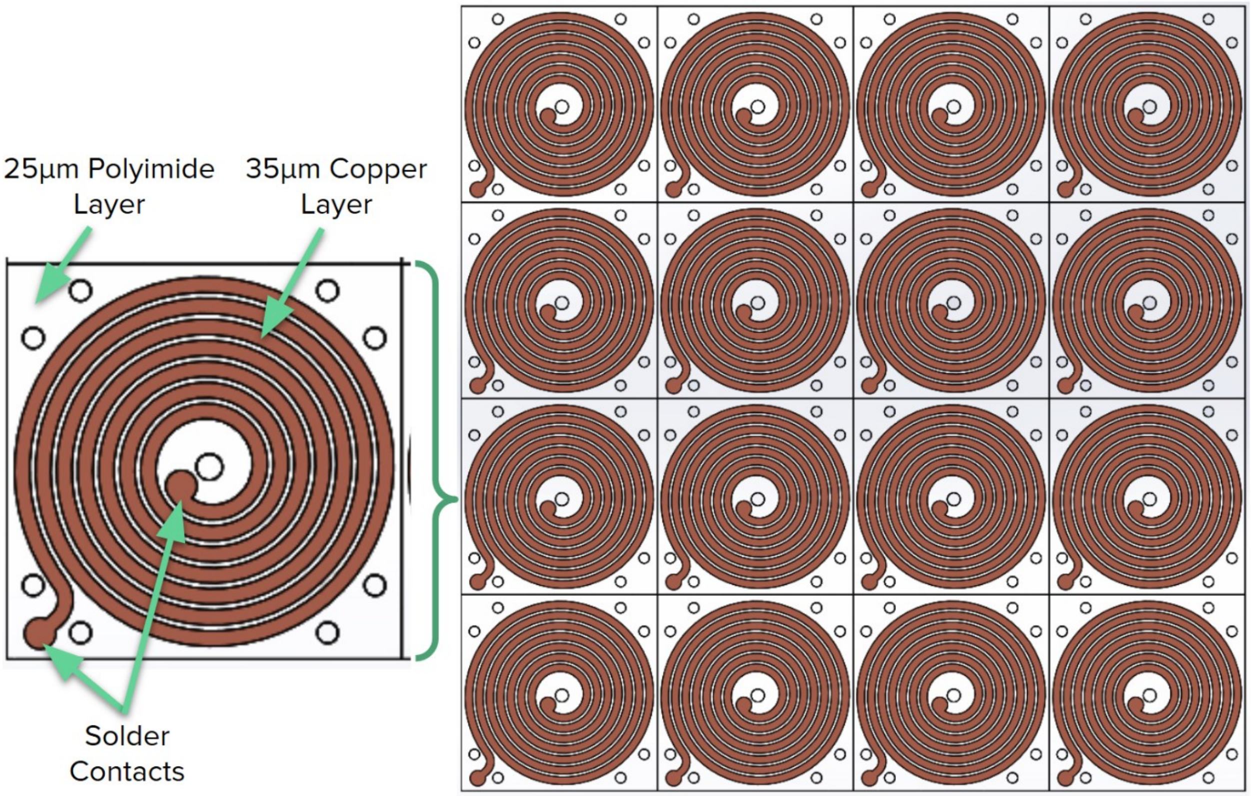

Figure 24: PCB Etching Path for ProtoLaser Coils

When fabricating the coils on the ProtoLaser, the team faced geometric scaling issues and the initial print came out smaller than expected. Edits were made to correct the scaling, then the print was run again. The results of the print are shown below. As noted in the Figure 25, the coils are very small and very thin.

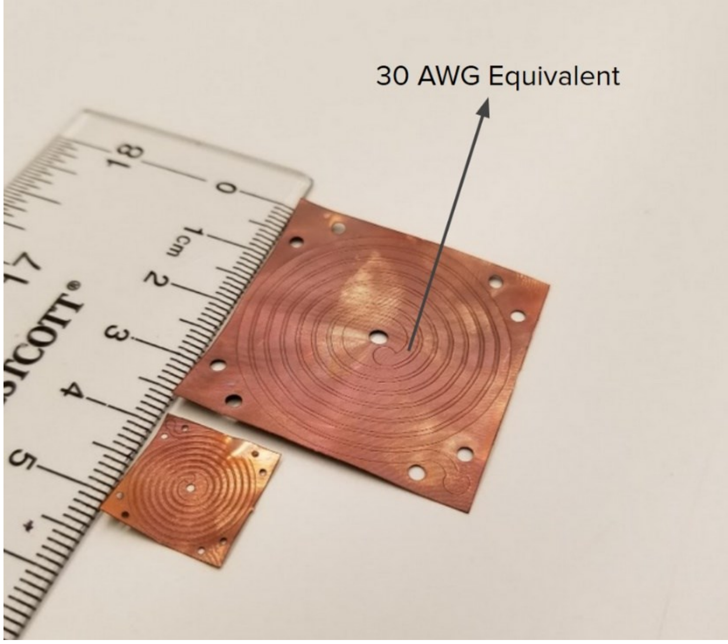

Figure 25: PCB Etched Pyralux Prototypes

The Pyralux planar coils seemed like it had potential, however the team ran into several issues with fabrication and assembly. First, even though the ProtoLaser left a noticeable imprint in the Pyralux sheet, the etching laser was not enough to fully remove the copper layer, thus losing the ability to restrict current flow and create a consistent magnetic field. Additionally, the team had difficulties finding a practical way to connect each sheet together into a continuous circuit. The etched contact pads were too small to reliably solder by hand and adding wires between the sheets would take a considerable amount of time and increase overall coil height. On top of connecting the layers in a circuit, the team would still need to physically hold the layers together, which also proved challenging. Potential ideas to achieve this included pins, rivets, and thread. Ultimately, it was deemed far too time-consuming to try to combine the layers. As a result, while the use of Pyralux-etched coils seemed promising on paper, the inability to reliably execute on fabrication doomed it to be only that.

4.1.3. Iteration 3: Planar Coil Spring

The third design iteration applied the findings from working with flexible copper-clad-based coils back to traditional magnet copper wire. Compared to Pyralux, magnet wire allowed for higher wire turn density at the cost of actuator flexibility. Planar springs were incorporated into the design at this stage, investigating actuator performance targeted at a specific spring resonance. The planar coil disk was placed within a 3D printed housing to the top half of the actuator. The bottom half included a housing array with seven N40 3.2mm cube magnets bonded to a tuned planar spring. Figure 26 highlights the arrangement of these components.

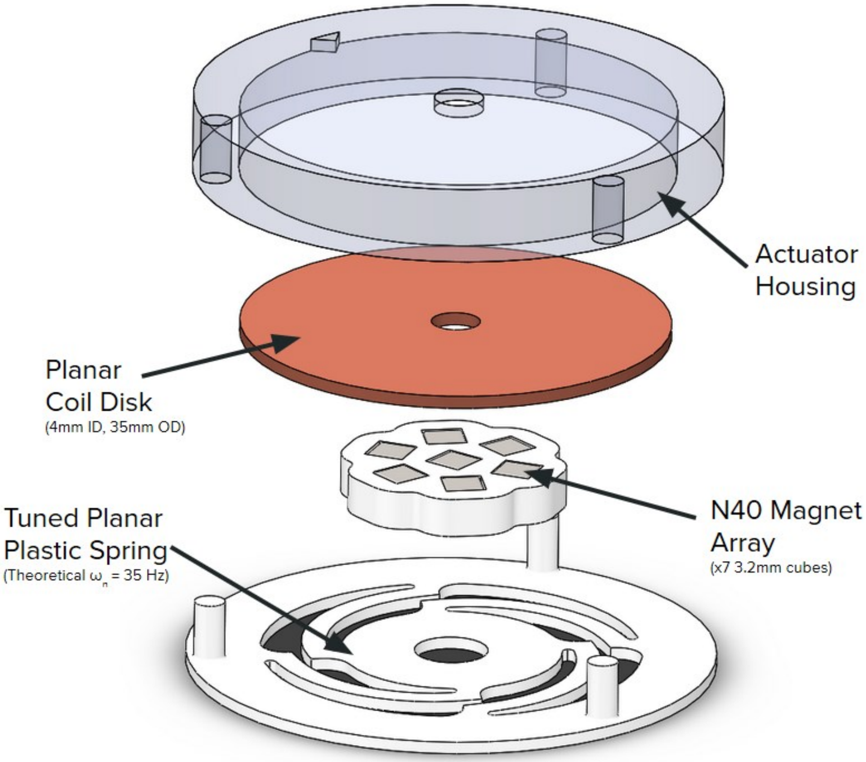

Figure 26: Planar Coil Actuator CAD - Exploded View

The wire-based coil disk required a rigid housing and silicone adhesive to retain its form. To mitigate the impacts of flexibility loss, a strong focus was placed on reducing the actuator footprint and reducing the outer diameter (OD). By combining FEMM and MATLAB, the coil disk geometry was optimized to obtain the critical relation between actuator force and coil OD. For prototyping and experiment flexibility, seven 3.2mm cube magnets were used. To analyze this in an 2D axisymmetric environment, the seven cube magnets were modeled as a disk magnet with the same magnetic volume (229.4 mm^3) and diameter footprint, a 0.9mm high and 18mm OD N40 magnet. Using a 2mm airgap, 1mm coil disk height and 2mm inner diameter, the OD was analyzed between 10mm and 50mm in steps of 1mm. The resulting force-to-OD relation is shown in Figure 27.

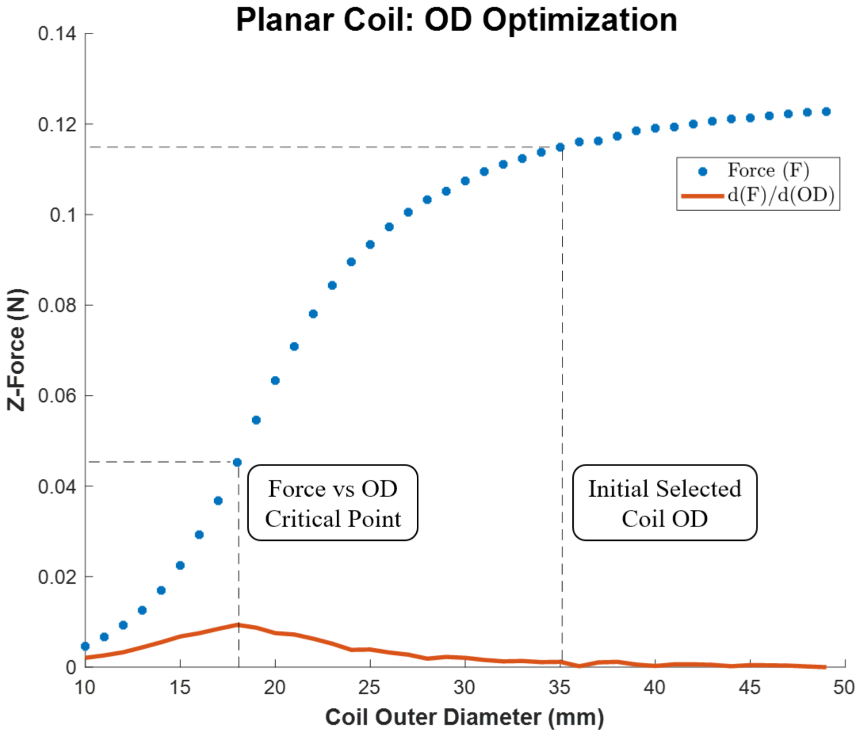

Figure 27: Planar Coil Outer Diameter (OD) Optimization

The blue line shows force while the orange line represents force change per change in OD. This reveals that at OD = 18mm, each additional turn provides the largest contribution to force. By setting the actuator OD a distance above this critical point, the actuator is considered to include a larger percentage of wire turns that generate the most force per turn. An OD of 35mm was selected to include this critical point and limit the addition of wire turns with little force contribution. The resulting FEMM, Figure 28 indicated a 0.115N for 240 turns with a 2mm airgap.

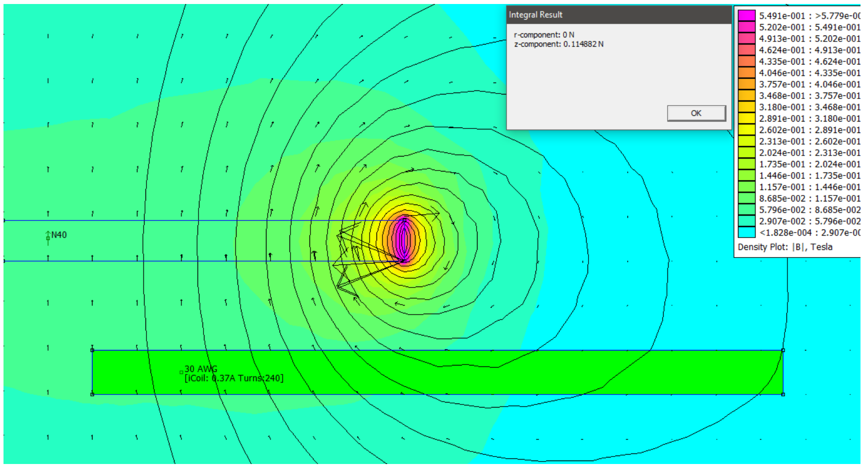
Integral Result

```
r-component: 0 N
z-component: 0.114882 N
```

Figure 28: 35mm Planar Coil FEMM & Resulting Coil Geometry (240 turns)

The manufacturing of a rigid copper coil geometry was the major challenge in the prototyping phase. To create the thin coil disks, a sewing bobbin-inspired tool fixture was designed. The first version of this bobbin consisted guiding two disks that snapped together on a central shaft with snap fits, Figure 29. Once wire was secured around the central shaft, the bobbin was mounted to the end of a hand drill for controlled winding, with silicone being brushed on the wires for disk adhesion. An ideal bobbin assembly with perfect parallelism would produce a 240-turn coil disk that is 4 wires height.

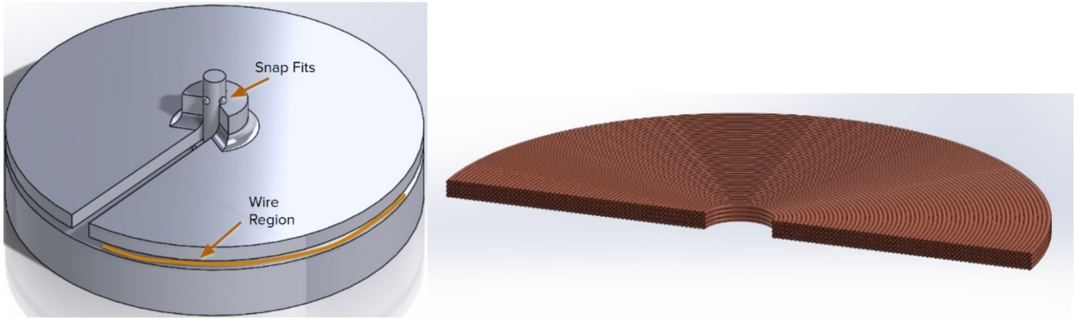

Figure 29: First Bobbin Design & Resulting Coil Geometry (240 turns)

The planar springs were fabricated on Ultimaker 3 printers for initial prototyping. From initial qualitative testing, a target natural frequency of 35 Hz was selected in hopes of increasing haptic perception. Because of this low frequency, Nylon Bridge was selected as the 3D print spring material for its low elastic modulus. Using ANSYS Structural for modal analysis, a four-arm spring geometry was tuned for 35 Hz, seen in Figure 30.

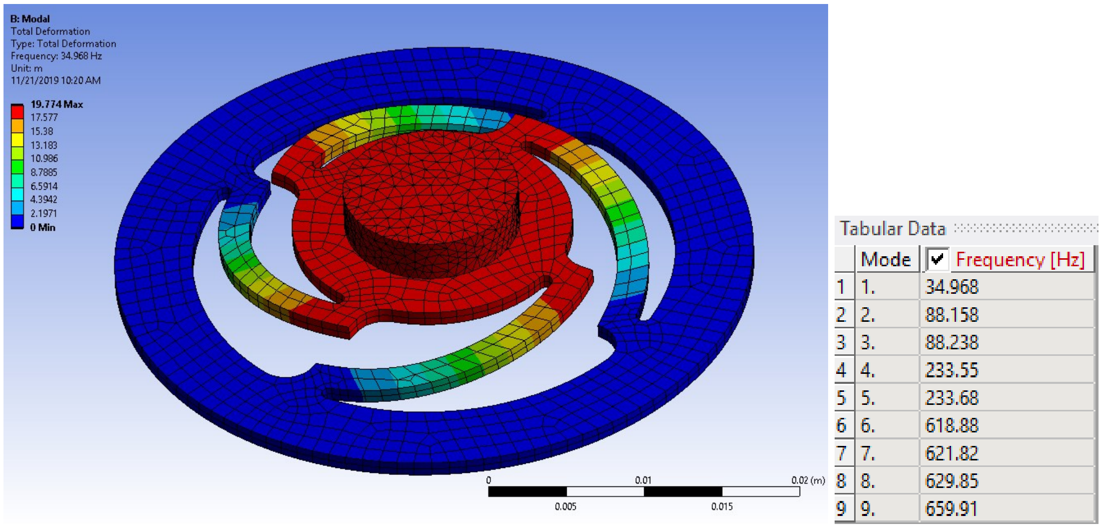

B: Modal
Total Deformation
Type: Total Deformation
Frequency: 34.968 Hz
Unit: m
11/21/2019 10:20 AM

	Mode	☑ Frequency [Hz]
1	1.	34.968
2	2.	88.158
3	3.	88.238
4	4.	233.55
5	5.	233.68
6	6.	618.88
7	7.	621.82
8	8.	629.85
9	9.	659.91

Figure 30: ANSYS Modal Analysis - Nylon Planar Spring

Once all 3D components printed and the coil disks wound, the cube magnets were inserted into the spring part. The final assembly, shown in Figure 31, had a total OD of 43 mm and a height of under 8 mm. Using a Polytec Scanning Vibrometer (PSV-400) laser scanner, the actual natural spring frequency was measured to be 118 Hz, differing greatly from the ANSYS estimates. This large discrepancy was caused by the ANSYS having spring constraints than differed from the physical model. The 3D printed spring geometry itself also experienced dimensional variations of up to 15% compared to the CAD model, altering the spring stiffness characteristics. Additionally, the high damping properties of 3D printed nylon overdamped the spring response, likely contributing to a higher perceived natural frequency (Senthilvelan &

Gnanamoorthy, 2006). These issues were considered for in the final design and are addressed in Chapter 5.0.

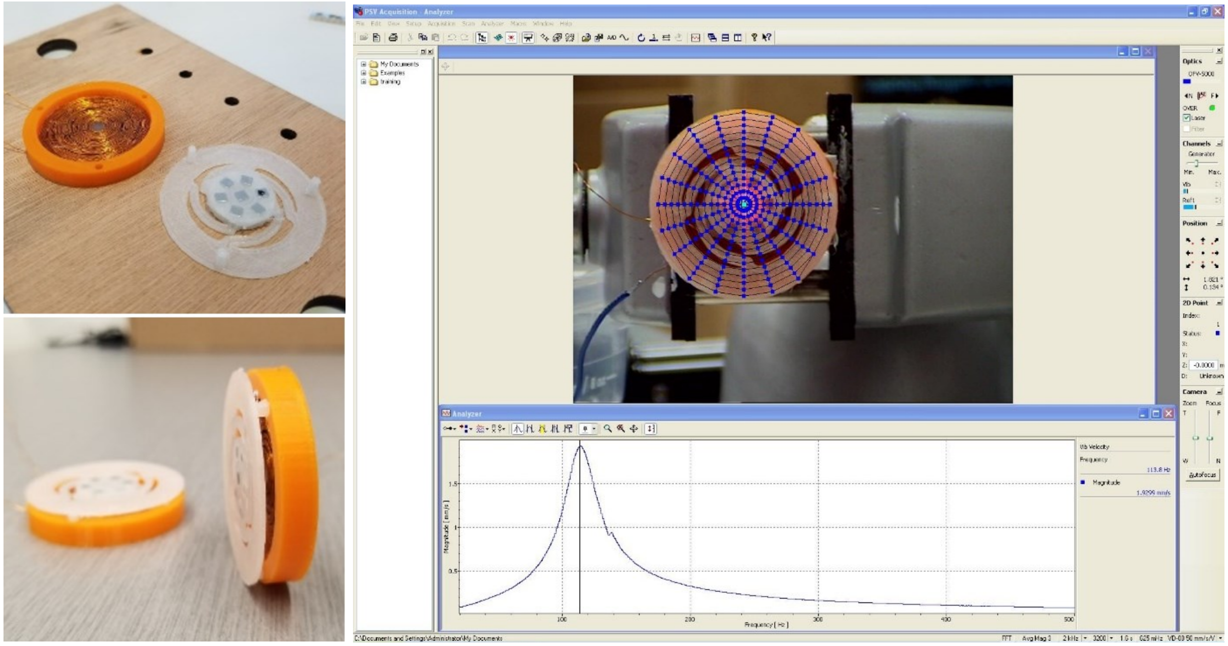

Vib Velocity
Frequency 113.8 Hz
Magnitude 1.9299 mm/s

Figure 31: Iteration 3 Hardware (left) & Natural Frequency Laser Scan (right)

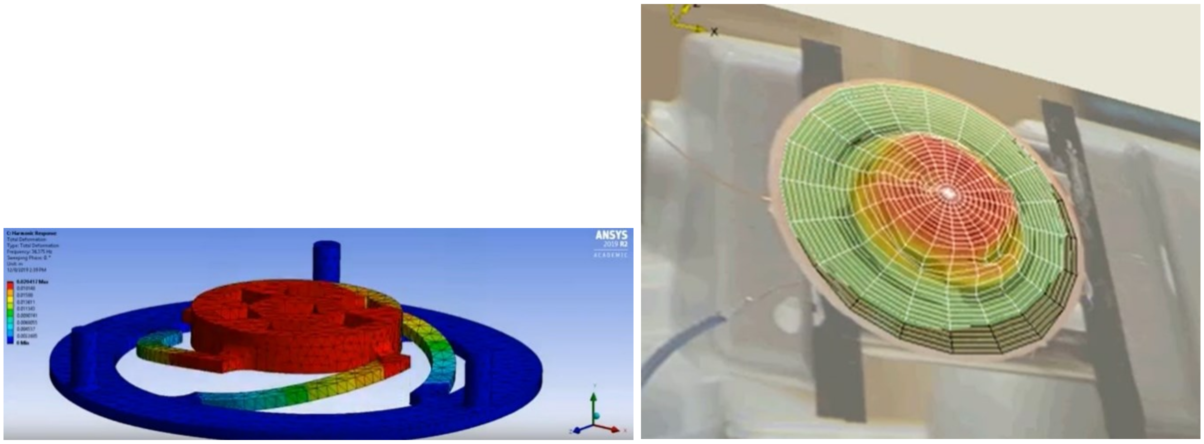

Figure 32: 3D Printed Nylon Spring Harmonic Results

4.2. Electrical and Software Iterations

The following shows the development process on the electrical aspect of this project.

4.2.1 Actuator Electrical Characteristics Validation

The impedance of the actuator was measured using the experimental setup outlined in Section 3.4.3 and the results were as follows:

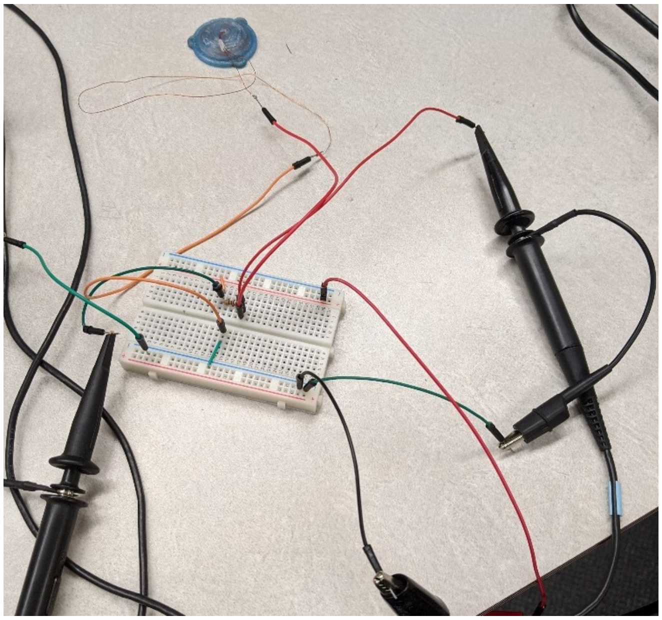

Figure 33: Impedance Experiment Setup

$$Z = \frac{V_{A2}}{I} = \frac{V_{A2}}{V_{A1} - V_{A2}} R_{ref}$$

$$I = \frac{V_{A2}}{Z}$$

At 167 Hz:

CH1 = 2.08 V

CH2 = 147 mV

$R_{ref} = 100\ \Omega$

$$Z = \left(\frac{0.147}{2.08 - 0.147}\right) V \times 100\ \Omega$$

Impedance of actuator at 167 Hz = 7.6 Ω

$$I = \frac{0.147\,V}{7.6\,\Omega}$$

Current consumption of actuator at 167 Hz = 19.34 mA

At 200 Hz:

CH1 = 2.08 V

CH2 = 184 mV

R_{ref} = 100 Ω

$$Z = \left(\frac{0.184}{2.08 - 0.184}\right)V \times 100\,\Omega$$

Impedance of actuator at 200 Hz = 9.7 Ω

$$I = \frac{0.184\,V}{9.7\,\Omega}$$

Current consumption of actuator at 200 Hz = 18.97 mA

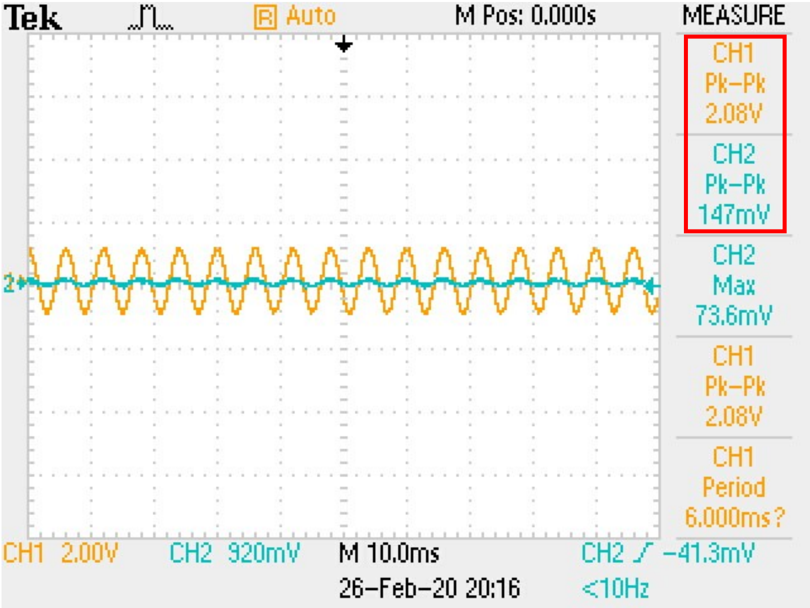

Figure 34: Oscilloscope Reading at 167Hz

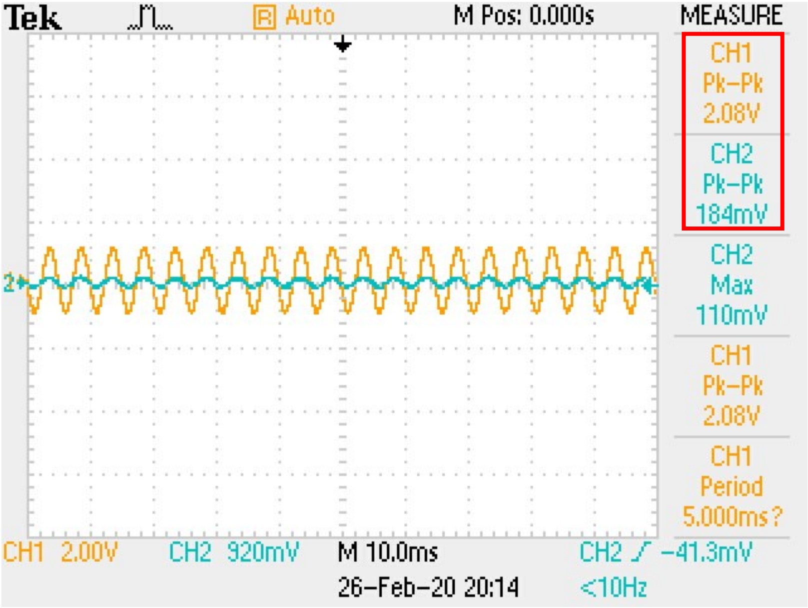

Figure 35: Oscilloscope Reading at 200Hz

For the second experiment, the total current passing through the system was recorded to be 21.8 mA without a resistor connected and 13.6 mA passing through the MOSFET and into the actuator with a 100 Ω resistor connected.

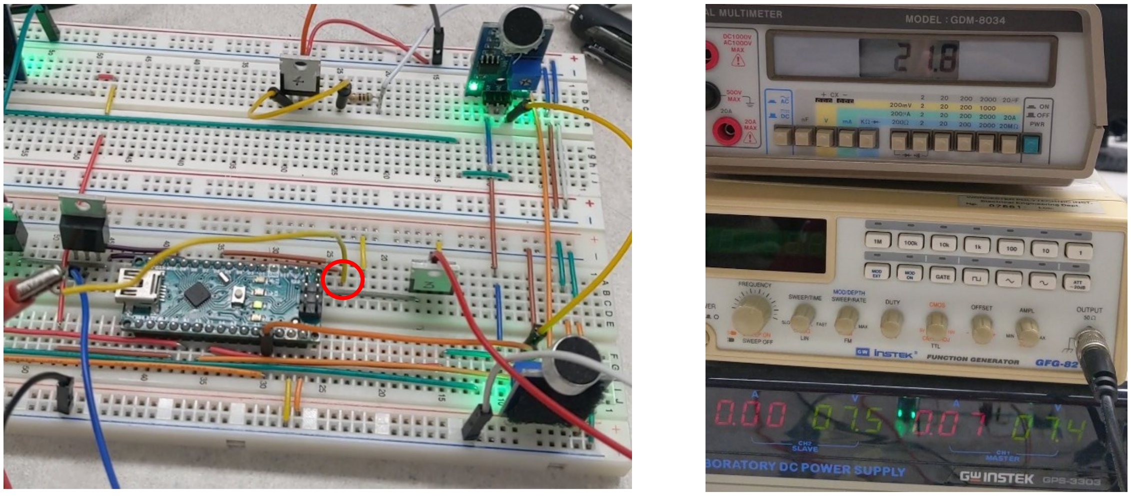

Figure 36: Circuit Setup and Recording at Point 1

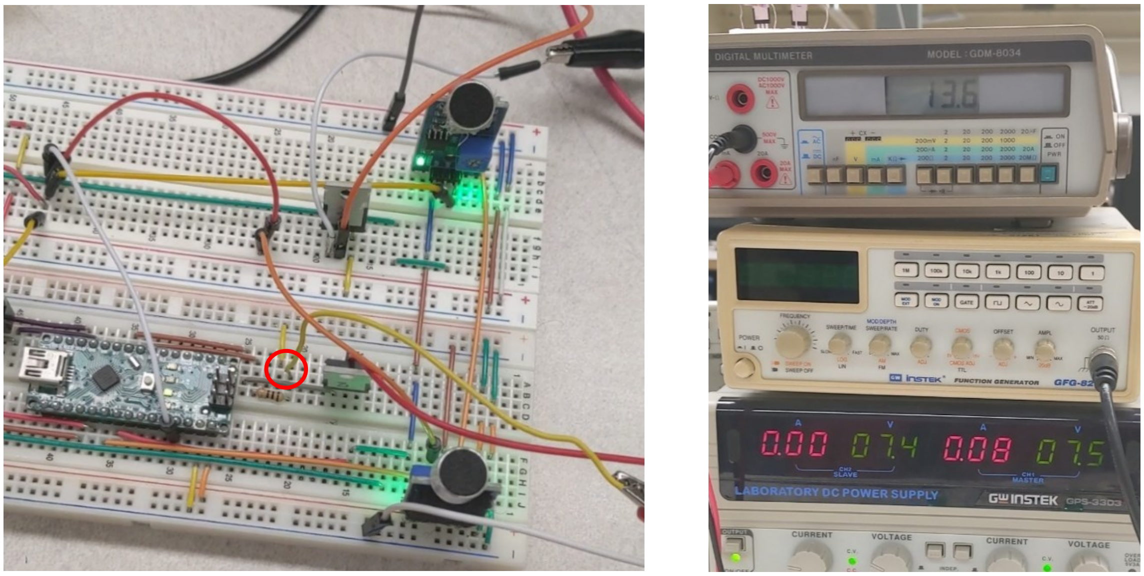

Figure 37: Circuit Setup and Recording at Point 2

The overall power consumption was calculated using the following equation:

$$P = V \times I$$

$$P = 7.4\,V \ \times 21.8\,mA$$

The total power consumption of the system was 0.161 W.

4.2.2 Single Microphone Testing

The team designed the input side of the device by analyzing the audio amplitude from the selected microphone. Ideally, a microphone with digital output was needed so the signal could be conveniently analyzed in Arduino. Additionally, the team need the microphone to be small and planar so that the whole system could be kept close to flushed with clothing.

The initial selection is the electret microphone amplifier with adjustable gain from Adafruit. This microphone amplifier comes with a 20-20kHz electret microphone soldered on, which allows all range of frequencies a human ear would catch to be recorded. It also works great with Arduino since its supply voltage could range from 2.4-5VDC.

The team then designed an amplitude imager to visualize the audio input signals from the microphone. By adjusting the potentiometer on the amplifier, the sensitivity of the microphone could be adjusted so that it would filter out most of the noise, and only pick up louder sounds. Figure 38 shows the microphone sensitivity testing process with the amplitude imager. The sample rate was set to be 50 milliseconds so that all sounds down to 20Hz could be picked up.

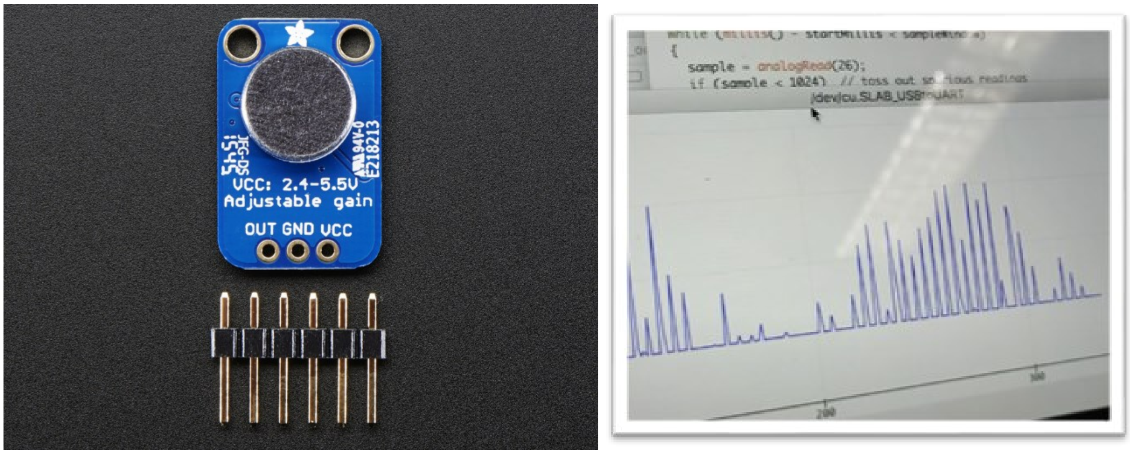

Figure 38: Microphone Selection & Signal Amplitude Serial Plot

4.2.3 Dual Microphones Testing

Two microphones were then tested to compare the amplitudes on both channels. Modifying the previous amplitude imager, inputs from both channels were able to be displayed on screen, shown in Figure 39. By moving the sound source from one side to the other, some clear differences in sound amplitudes could be seen. However, there is still a lot of noise in the system.

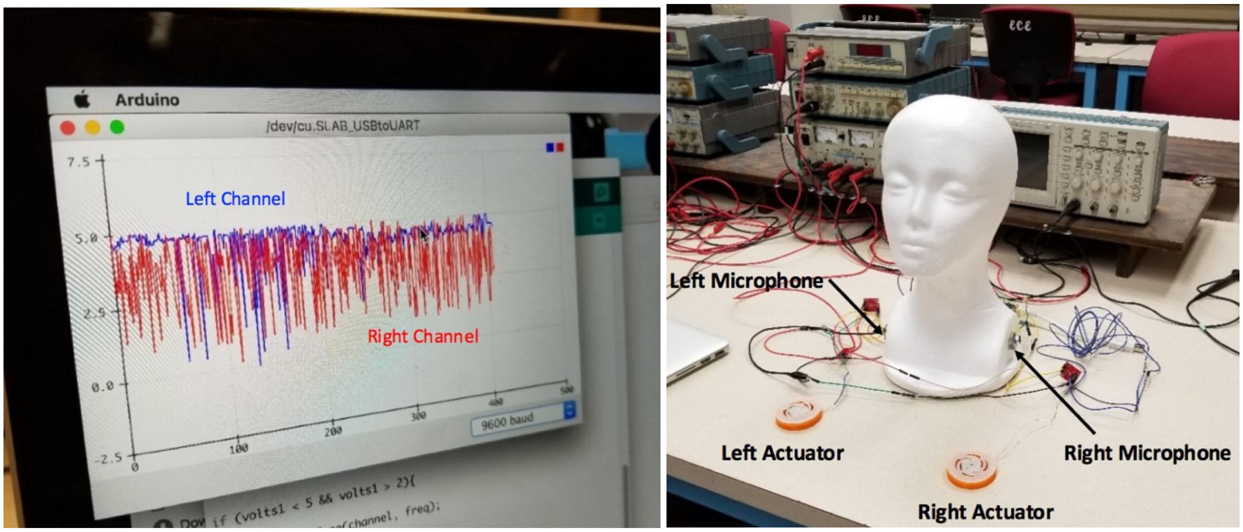

```
if (volts1 < 5 && volts1 > 2){
```

Figure 39: Dual Microphone Testing: Serial Plot and Set-up

The team then set up the two microphones on a mannequin head, show in Figure 39, to simulate the positions of the two microphones on the prototype assistive device, as well as to replicate damping caused by the human head itself. The microphone input sensitivities were then adjusted, respectively. By threshold gating, the actuators could be triggered at their resonance frequency when the input reaches the desired level.

4.2.4 Quad Microphones Set-up and Improvements

For increased directional resolution, the number of microphones increased to four. As the number of microphones is doubled, it becomes more difficult to distinguish the amplitudes from each microphone. Therefore, the team opted for new microphones with higher sensitivities. Figure 40 shows the testing process for the four-microphone array. However, the new microphones are a lot more unstable regarding amplitude readings. It was decided that the microphones would be calibrated n a controlled environment before further testing.

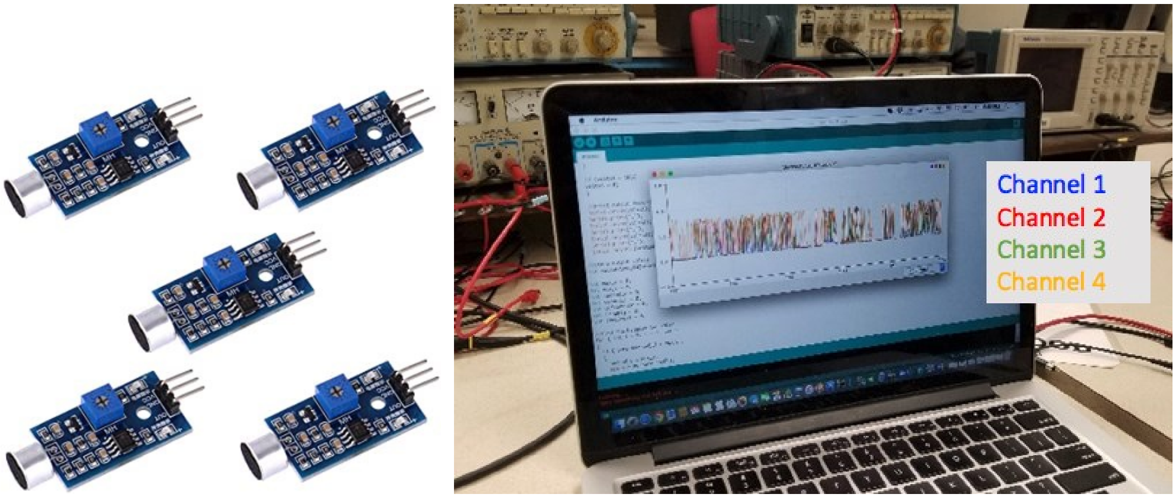

Figure 40: New Microphone Selection & Quad Microphone Serial Plot

To further distinguish the location of the sound source, the team decided to use an amplitude to frequency conversion to adjust the output frequencies to the actuators. When the sound amplitude reaches the set threshold, the actuators are triggered at their resonance frequency. The output frequency was gradually lowered when the sound amplitude decreased.

4.3 Microphone Housings

To provide more directionally, and protection for the pins and components attached to the microphone PCB, individual housings designed to cover the microphones. Figure 41 shows the first iteration of the housing. A half-shell design, the top of the microphone is covered while the bottom is open so that the housing can be placed over the microphone to secure it to the shirt. A small elastic band would be used to hold the housing in place over the microphone PCB, fixing it to the wearable. Openings at the front and back of the housing expose the microphone so it can pick up sounds, and so that the wires can connect to the pins. All the mics shown in the CAD models are the Anmbest Module LM393 microphones.

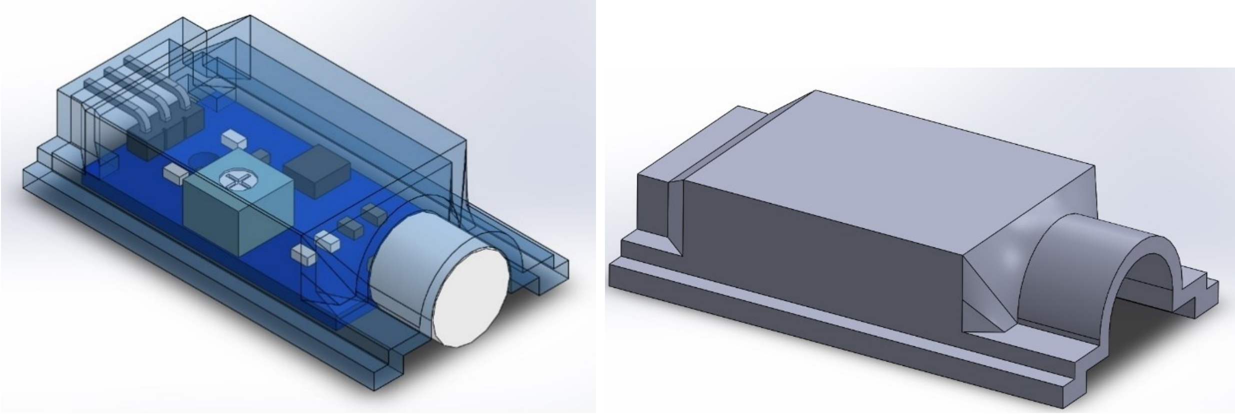

Figure 41: Microphone Housing 1

The housing design was revised for an adjusted microphone position, shown on the following page in Figure 42. The pins connecting the microphone to the PCB were bent to angle the microphone so it would be perpendicular from the surface of the wearable. This was to allow the PCB to lay flat on the shirt wearable, while the microphone could be pointing outward to capture sounds from specific directions. This iteration has an open front to reduce the amount of material used to manufacture the housing, while having a semi-circle shell to protect the microphone from being bent back down toward the shirt. However, this design left the pins connecting the microphone to the PCB exposed.

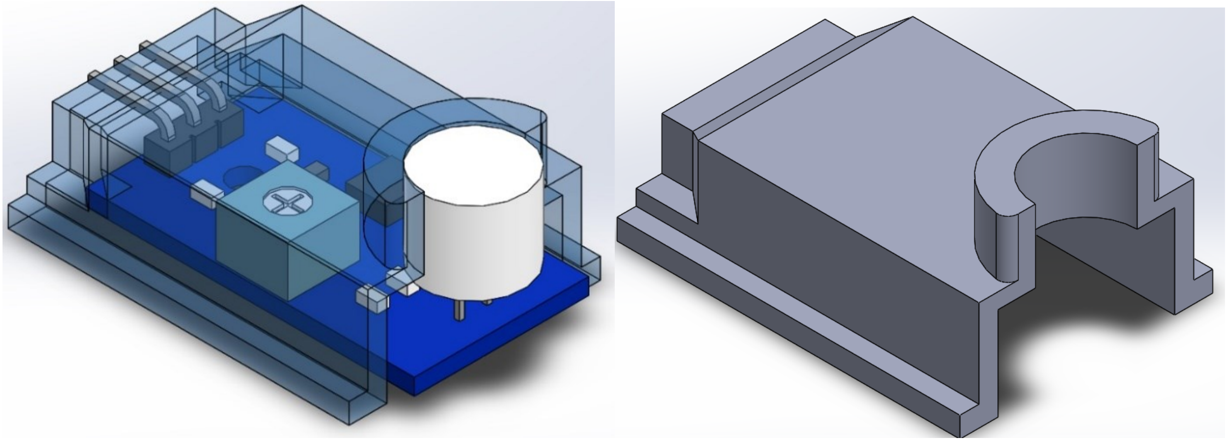

Figure 42: Microphone Housing 2, Vertical v1

The vertical microphone was kept and the housing was redesigned again. With each iteration, prototypes were manufactured using 3D printing to check their fit on the microphone PCB. The main challenge encountered during this design process was getting the sizing correct; the smaller a component was, the more difficult printing it became since smaller designs that require a higher accuracy are more sensitive to the effects of shrinkage. To account for this, the dimensions of the housing were increased assuming a 2.5% shrinkage when PLA filament cools.

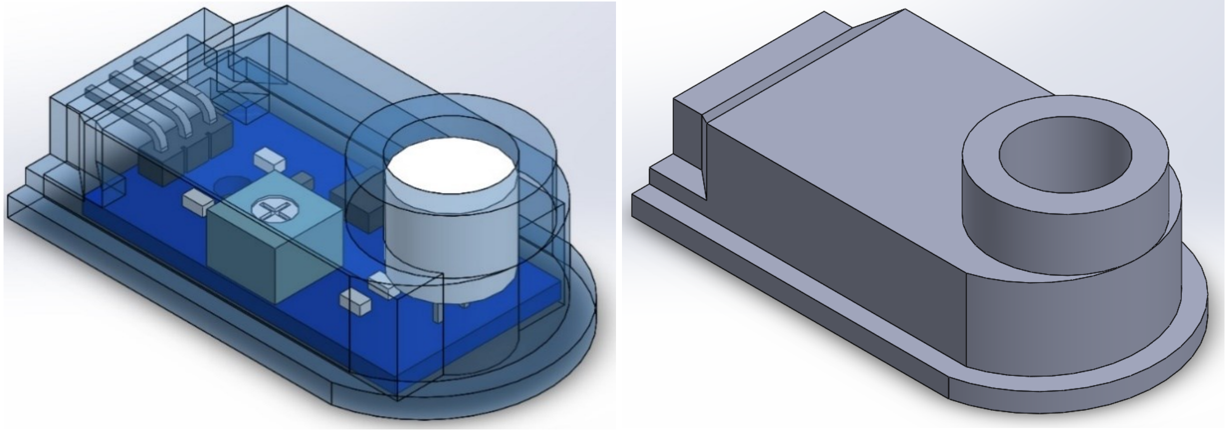

Figure 43: Microphone Housing 3, Vertical v2

The third iteration, pictured above in Figure 42, fully encases the microphone at the front of the PCB. The cylinder encasing the microphone was designed to extend beyond the top of the microphone to increase directionality. This feature made it more difficult to place the housing over the microphone so the design was altered for the final time, to make the opening level with the microphone again and adjust the shape of the housing to reduce its profile. The final housing design is shown below in Figure 44.

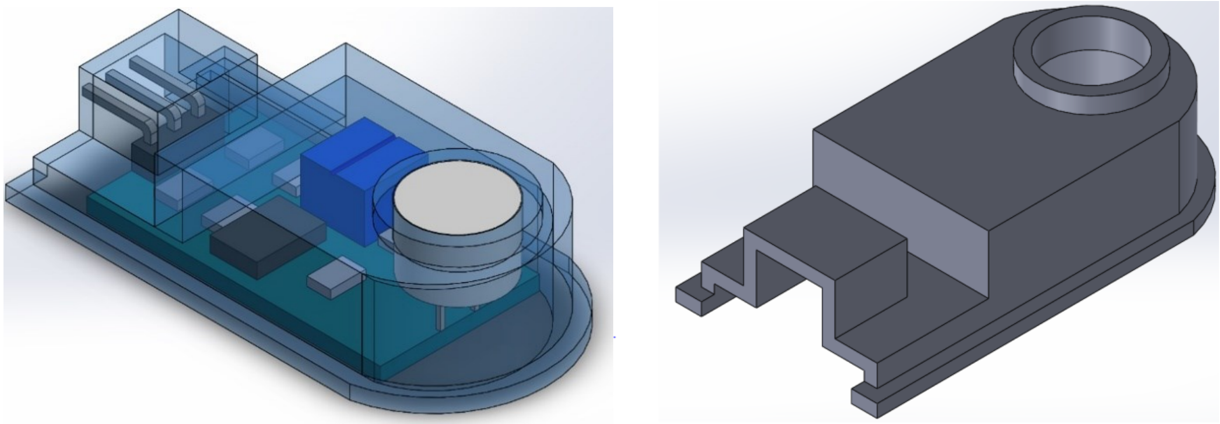

Figure 44: Microphone Housing 4, Vertical v3

5.0 Design Results

Using the finding from background literature and previous design iterations, the following sections describe the final design system, system components, component analysis, and component validation.

5.1. Wearable Arrangement

A mockup of the final design for the wearable device was created in SOLIDWORKS, shown below in Figure 45.

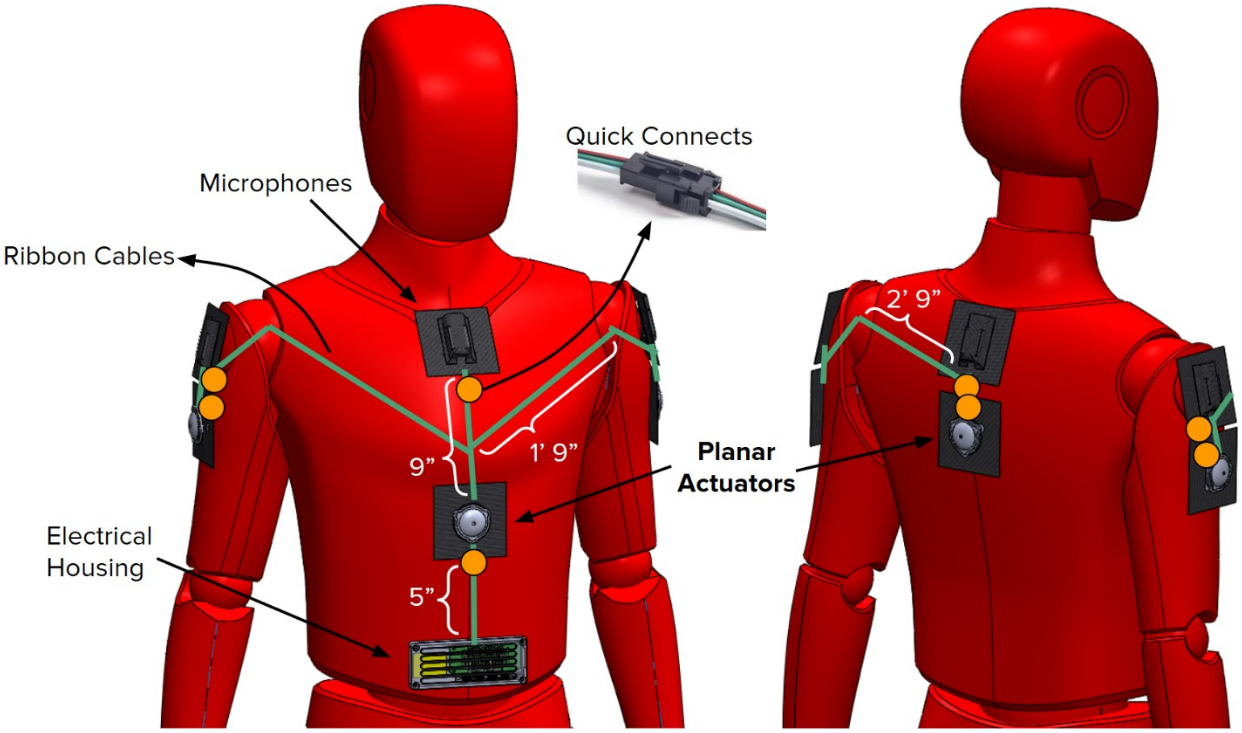

Figure 45: Wearable Arrangement SOLIDWORKS Model

The base of the wearable, which the electronic components and housings would be attached to, is a short-sleeve athletic shirt made of a lightweight and breathable polymer-spandex blend. Four planar, dome-shaped actuators are located on the upper back, torso and over the deltoid of both arms; this provides audio-spatial awareness in all major directions around the user. Four corresponding microphones are located on the collar of the shirt. Individual microphones for each actuator provide directionality by having comparable audio; the loudest audio input can be identified, which will trigger the corresponding actuator to indicate the direction a sound is coming from. The actuators and microphones are secured to the shirt using hook-and-loop tape, allowing them to be removed so the shirt can be washed.

Separate lengths of ribbon cable, represented by the green lines in Figure 45, connect the microphones to the actuators, and then connects to the electrical box located in pocket at the bottom front of the shirt. The electrical box contains a rechargeable power supply, processing chip and an On/Off switch for the wearable haptic system are located. The ribbon cable is held onto the shirt using elastic loops, and flaps secured with hook-and-loop tape to cover the wires. Quick connects connect the ribbon cable to the pins of the microphone PCBs and the wire leads soldered to the actuators. Quick connects allow the user to easily disconnect the wires from the components when they want to remove them from the shirt. The wearable is designed so the user is able to remove all electrical components so the shirt can be washed. To account for movement and fabric stretching, service loops are used to manage the wires and allow the lengths to adjust in different sections of the wearable as the user moves

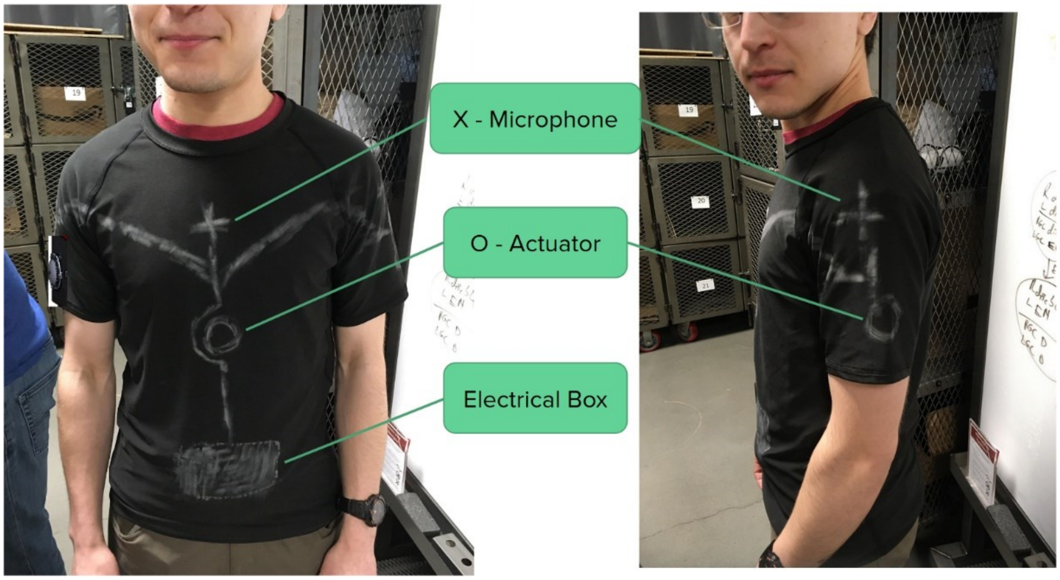

Figure 46: Marking Locations to Place Components on the Shirt Wearable

Prior to sewing on hook-and-loop tape, the placement of the components and path of the wires was marked on a prototype shirt, shown above in Figure 46.

5.2. Final Actuator Design

This section documents the final planar wearable actuator design, supporting analysis, and experimental validation.

5.2.1. Design Changes and Analysis

The final actuator prototype addresses previous issues of actuator size, force, component dimensional variability, and ideal material damping selection. By increasing the actuator's baseline mechanical performance, the overall actuator area footprint and height was further reduced. Figure 47, below, highlights the critical components discussed in this section.

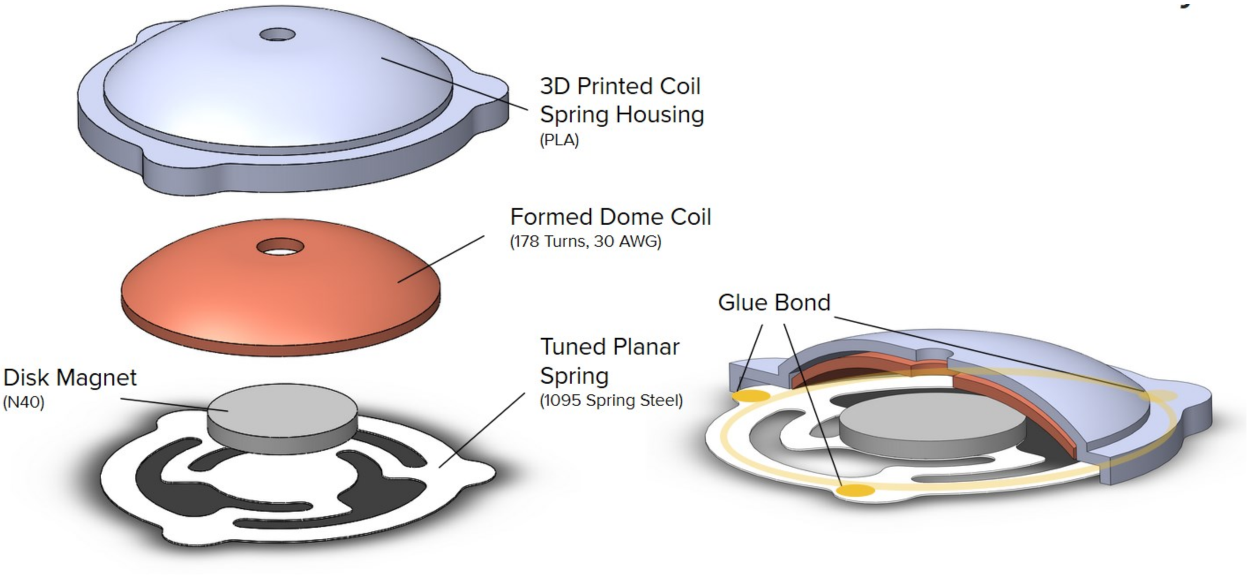

Figure 47: Dome Coil Components - Exploded view

A new spring material of 0.005" thick 1095 UNS G10950 spring steel was selected for its low damping properties and planar thickness. Since the primary mode of operation for the actuator is at resonance frequency, the team recognized that the required magnetic force input would be lower than the previous iteration by optimizing the spring material and design. As the magnetic force is dependent on current magnitude, the actuator input current was re-analyzed for a four-actuator arrangement, detailed further in section 4.2.3. The results of this electrical analysis concluded that the minimum current input for resonance operation was 0.0251 Amps instead of the previous 0.37 Amps. This change greatly reduced the magnetic forces per cycle, but accounts for the cumulative inertial output force of the actuator, detailed later in this section.

During this time, the team discovered a method to decrease the magnetic force to coil OD relationship from Figure 48. Instead of having a planar copper coil armature positioned below a disk magnet, the planar coil could be transformed into a dome formation. This increases the proximity between coil wires and the magnet itself, contributing to additional forces. Using a thin disk N40 Magnet, the analysis in Figure 48 found a significantly reduced force drop-off across dome coil ODs. Such results indicate that reducing the dome coil's OD, and number of turns, would not significantly decrease the force output. This relationship was more desirable as the variability in magnetic force was less impacted by the physical coil geometry tolerances, increasing the assembly's robustness. An actuator airgap of 2 mm was left between the corner of the magnet and dome coil geometry to account for assembly tolerances and actuator stroke. Following these results, Figure 48, a minimum actuator coil OD of 27mm was selected due to assembly and actuation dimensional clearances with a magnetic force of 0.0076 N.

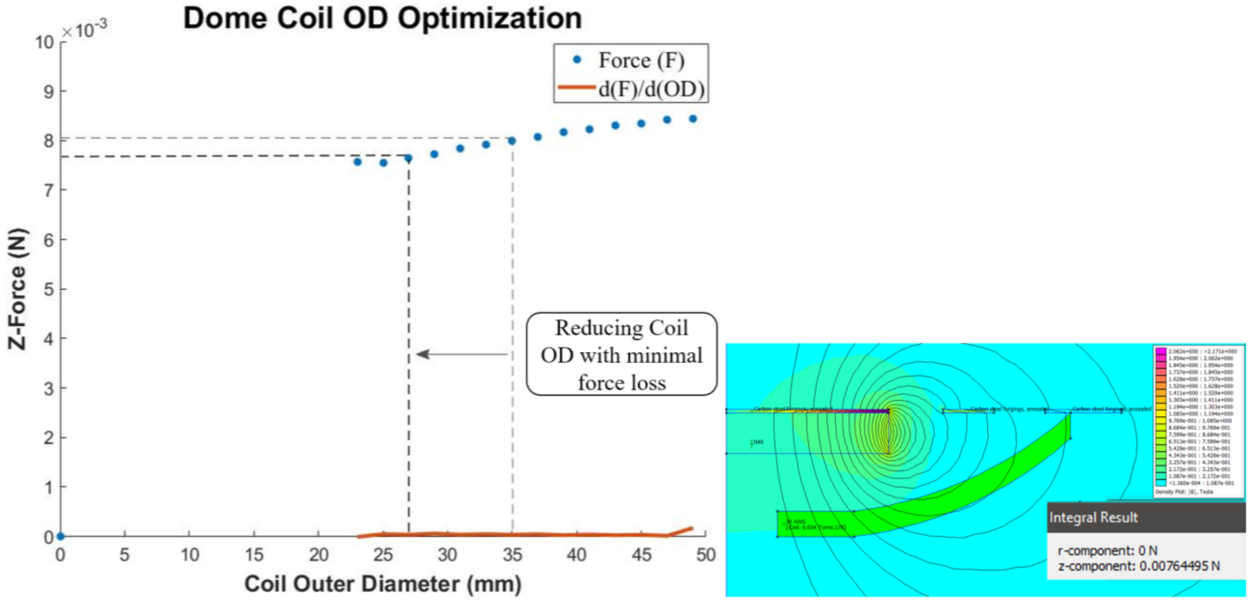

Integral Result

r-component: 0 N

z-component: 0.00764495 N

Figure 48: Dome Coil OD-to-Force Analysis (left) and FEMM Magnetics for 27mm OD (right)

The team conducted further analysis using ANSYS Maxwell for in-depth 3D magnetic analysis. Using the same dimensions, materials, and electrical excitations, the force applied on the excited coils was recorded. The results, shown in Figure 49, estimate an applied magnetic force of 0.00595 N.

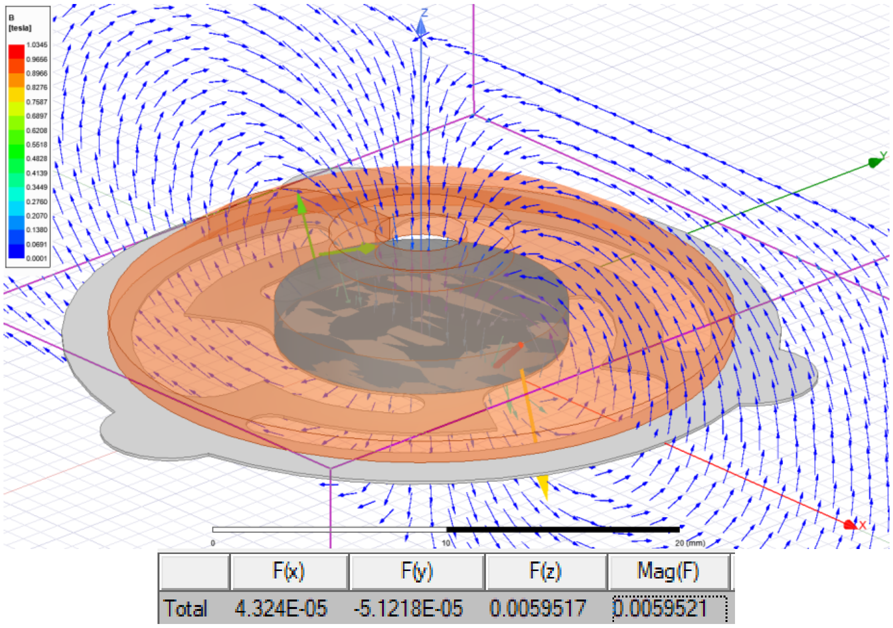

	F(x)	F(y)	F(z)	Mag(F)
Total	4.324E-05	-5.1218E-05	0.0059517	0.0059521

Figure 49: ANSYS Maxwell - 3D Magnetic Force Analysis

Using the average of the FEMM and Maxwell results (0.00678 N) as the input cycle force, the team conducted a modal harmonic analysis to determine the primary mode frequency and magnet dynamics. The planar spring geometry was optimized during this time to achieve vibration modes within the target haptic range of 160-250 Hz. The number of spring lever arms were reduced from four to three to reduce the number of undesirable torsional modes. In ANSYS Structural, force was applied on the magnet center plate with the spring tabs and outer edge constrained. From the analysis shown in Figure 49, the final spring geometry had a first mode of 168.6 Hz. The harmonic results also report displacement, velocity, and acceleration data. Measuring at the moving magnet location, the magnet expected peak displacement, velocity, and acceleration are summarized in Table 1.

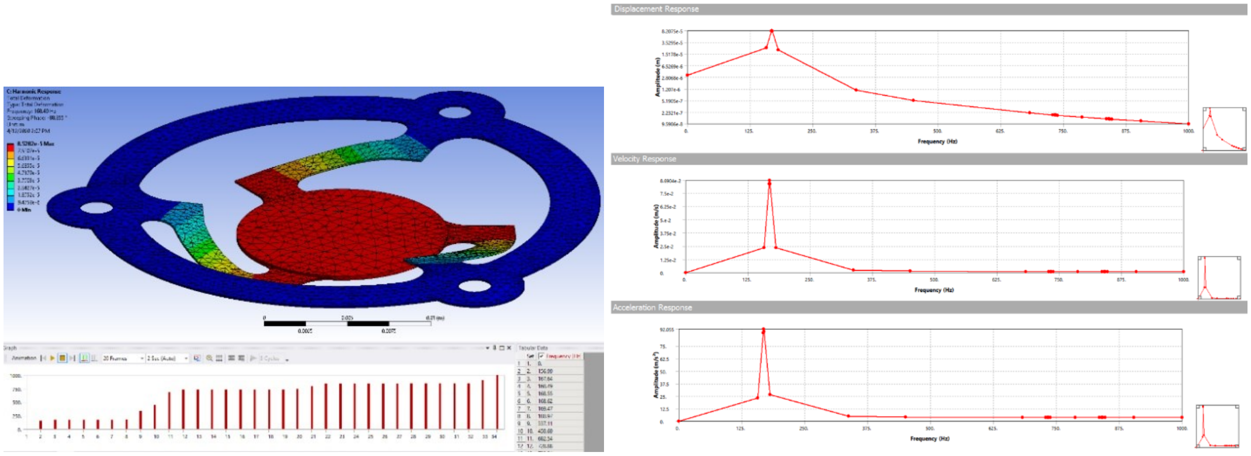

Figure 50: ANSYS Structural - Planar Spring Steel Harmonic Analysis

Table 2: Final Analysis Results Summary

First Mode	$M_1 = 169\ Hz$
Peak Displacement	$\delta = 0.082\ mm$
Peak Velocity	$V = 86.9\ mm/s$
Peak Acceleration	$A = 92040\ mm/s^2$
Magnet Mass	$m = 1.51\ g$
Time per stroke	$t = 2.97\ ms$

With the results above, the cumulative inertial output force of the actuator can be theoretically calculated. Using the impulse equation of $F_{ave}\Delta t = m\Delta v$, the average actuator force output per stroke was calculated to be 0.0442 N. Note that the magnetic input force per stroke is 0.0068 N. Provided time to approach resonance, the actuator is able to store momentum and exert a force 6.51X larger than its input force at steady state. The team quantified this force magnification to be the theoretical resonant effectiveness of the final spring actuator system.

5.2.2. Fabrication

Part fabrication began once the magnet and armature coil position and geometry were defined. The dome coil was created in two steps, first wound as a flat coil and then pressed into a dome form. The bobbin winding device was modified for improved coil-thickness tolerance and reduce the parallelism issues seen in section 4.3. As shown in shown in Figure 51, the addition of a hitch pin hole in the base tower and top body provided a rigid gap constraint, while the longer pole and slot transition fit further restricted angular displacements between the bodies.

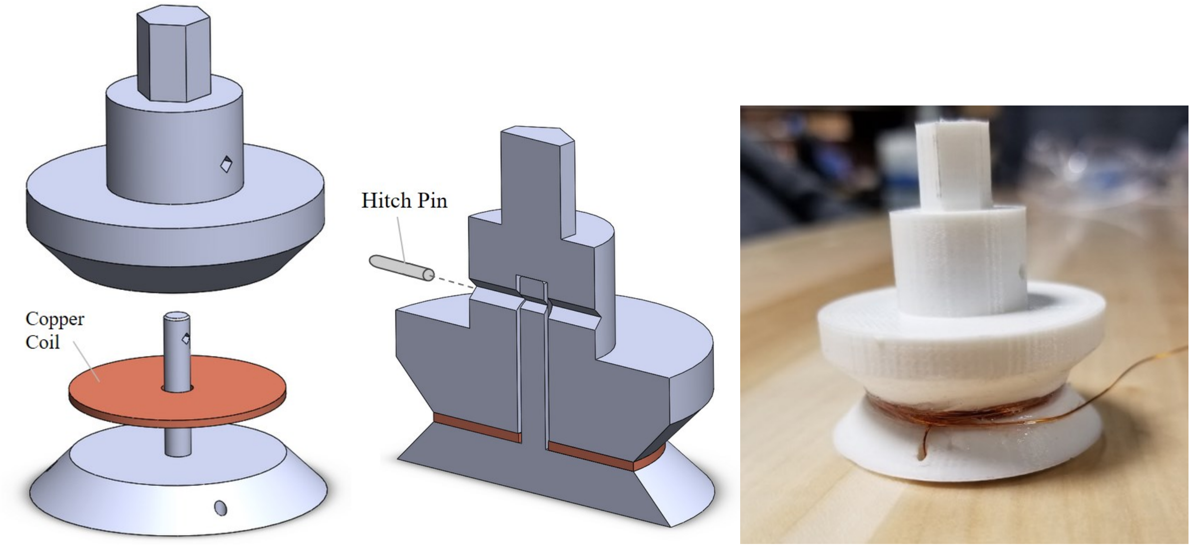

Figure 51: Final Bobbin Coil-Winding Design

Silicone was applied during the winding processes, thus the flat coils were removed and placed into a dome-pressing geometry before curing. The press assembly consisted of two 3D printed parts including a negative-image gap for the coil to fill and the coil housing itself, seen in Figure 52. After clamping for 24 hours, the coil domes were removed and already attached to the coil housing.

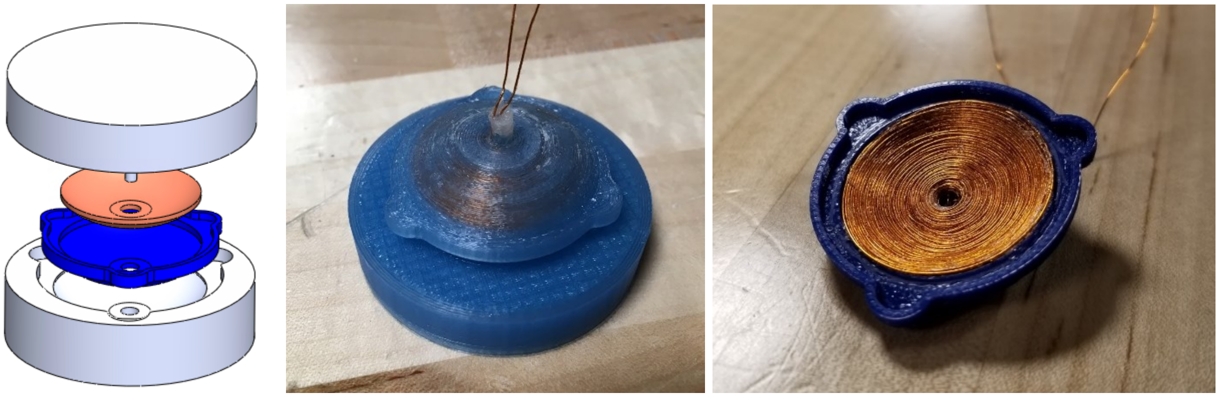

Figure 52: Coil Dome Press-Mold Assembly

The spring geometry derived from harmonic analysis was laser cut from 0.005” thick 1095 UNS G10950 spring steel on an OMAX 5555 JetMachining Center water cutter with the help of the Bose’s makerspace in Framingham, MA. To further investigate the effects of material damping in resonant systems, a set of Polycarbonate springs were also cut for testing purposes. The magnets were then attached with epoxy to the springs, and the spring edges were similarly adhered to the 3D-printed dome coil housing.

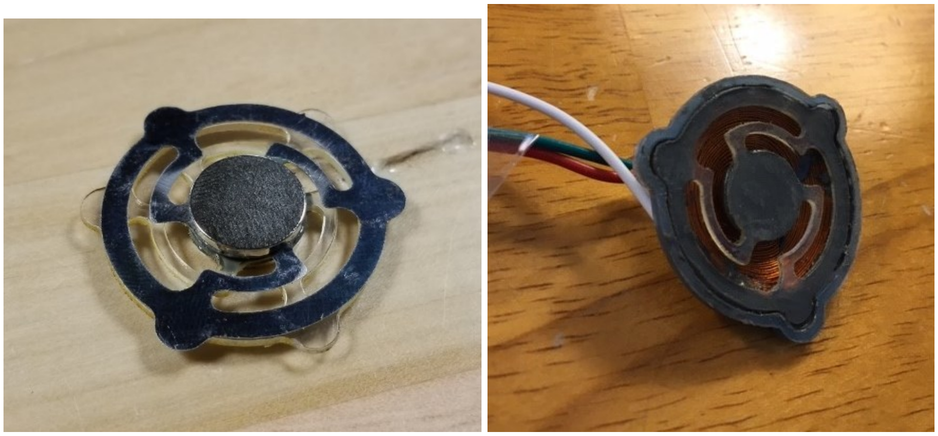

Figure 53: Fabricated Planar Spring & Magnet (left) and Assembled Actuator (right)

5.2.3. Experiments and Validation

To validate the harmonic resonance analysis conducted in ANSYS Structural, a Polytec Scanning Vibrometer (PSV-400) laser scanner was used to measure the spring displacement profile of the fabricated actuators. Actuators were rigidly fixtured on an air-bearing isolation table with the measurement focus on the spring center, shown in Figure 54. Note that the actuators were excited at a different current than the current of the final electrical current due to scanner availability. Thus, the following scan results are interpreted for their modal results rather than a complete harmonic response.

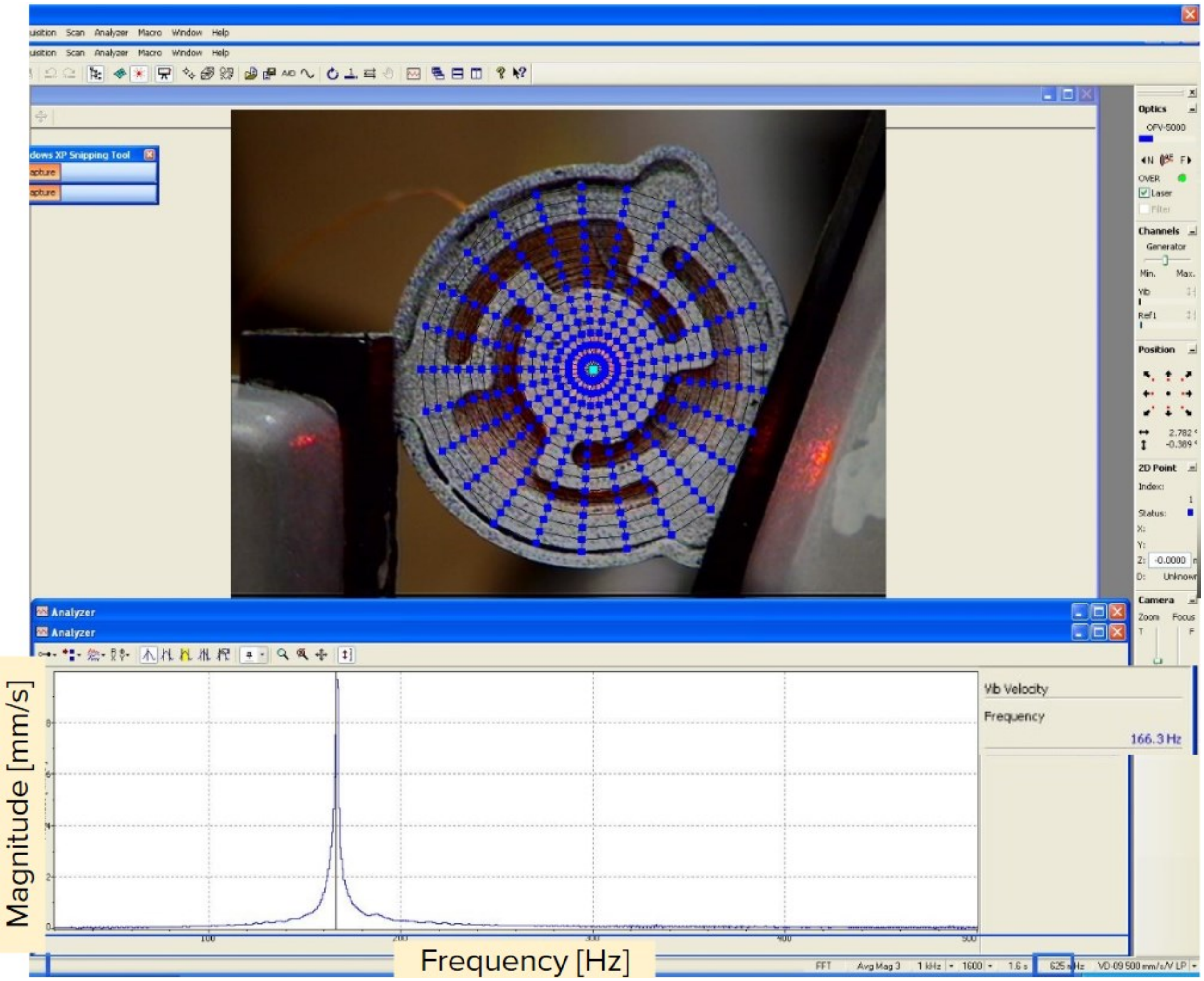

Figure 54: Laser Scan Measurements of Actuator Modal Response

From the results above, the first primary mode for the actuator spring-magnet was measured as 164 Hz, sufficiently close to the theoretical 169 Hz mode predicted in ANSYS Structural. By probing multiple points across the actuator base, a 3D displacement profile is also seen below in Figure 55 for the peak stroke (left) and mid stroke (right). The displacement profile of the stroke peak aligns with the expectation that the spring center and magnet are the dynamic components of the system.

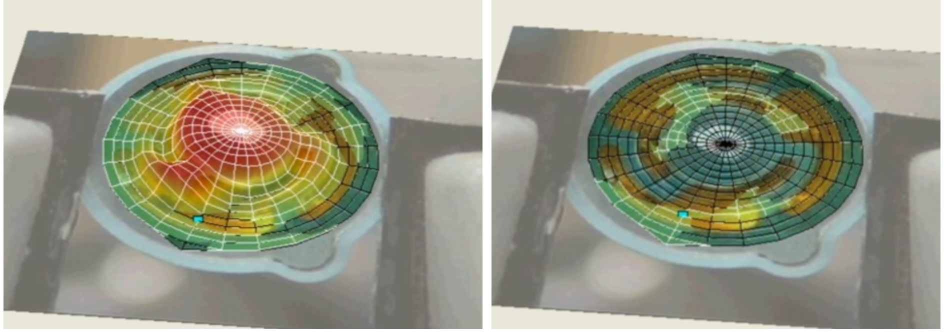

Figure 55: Laser Scan Displacement Maps - Peak Stroke (Left) and Mid Stroke (Right)

5.3 Final Circuit System Design and Signal Processing

The team settled on the final design of the circuit as depicted in Figures 56 and 57 below. It is complete with an electret microphone amplifier MAD4466 with adjustable gain from Adafruit, a 1k Ω resistor and a 7.4 V lithium polymer battery. The team also took the initiative to integrate a diode into the design because the actuator is partially an inductor. Consequently, without a diode across the actuator, if the transistor shuts off quickly, then the voltage across the actuator will get larger to ensure the continuity of current flow. This will probably result in destroying the transistor.

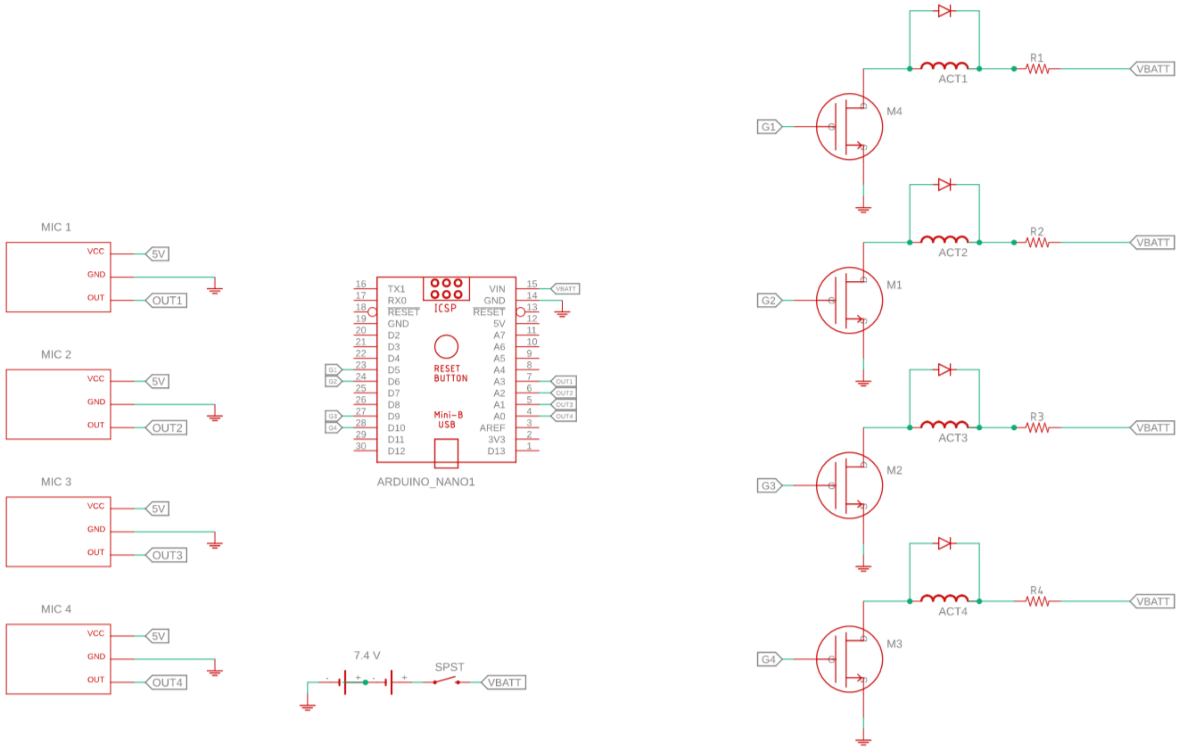

Figure 56: Schematic of Complete Electrical Design

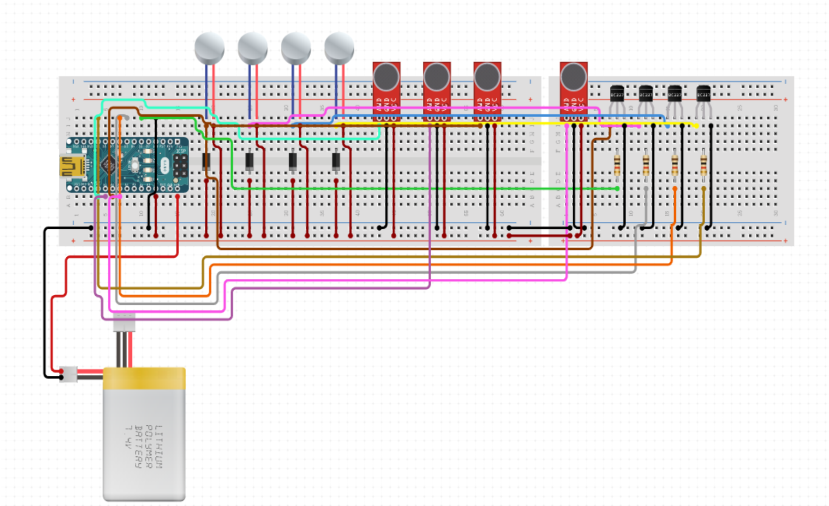

Figure 57: Complete Electrical Design

Upon testing the completed circuit design the team noticed a few discrepancies in performance. First, when a sound was directed towards a specific microphone the corresponding actuator would respond, but inconsistently. In other instances when the sound was directed toward a specific microphone, an actuator that was connected to a different microphone would respond. The team began to iterate the design further as seen in the analysis to draw some conclusions from observations. The team first narrowed down the problem to the microphones which were found to be uncalibrated omnidirectional MEMS microphones of unknown sensitivity with a digital output. The team came to this conclusion after drafting up a short experiment to analyze the microphones responses. Provided that there was no datasheet given for this particular brand, the team had no accurate or sure way of adjusting the threshold to be at the same level for all microphones. The potentiometer on the microphones was the only way of making any adjustments, but proved to be faulty when the threshold values differed from each other when the potentiometer was positioned at either extreme (there were no distinct increments on the potentiometer dial) with the same environmental settings (values were recorded in a sound proof chamber to simulate a ‘quiet’ environment). Additionally, the team discovered that using omnidirectional microphones may not have been the best solution to solve this specific problem. This added an additional layer of complexity to the system because the team had to detect sound origin. Since the system is designed to create directionality, a unidirectional microphone is more suitable for this application because they are optimized when selective pickup and rejection of room acoustics, background noise and leakage are of utmost importance. A unidirectional microphone with a cardioid pattern would have been more ideal since it is sensitive to sounds arriving from a broad angle in front of the microphone with decreased sensitivity of 6 dB at the sides and 15-25 dB at the rear. With the particular array orientation, the team designed, 360° would be accounted for with the implementation of four unidirectional microphones.

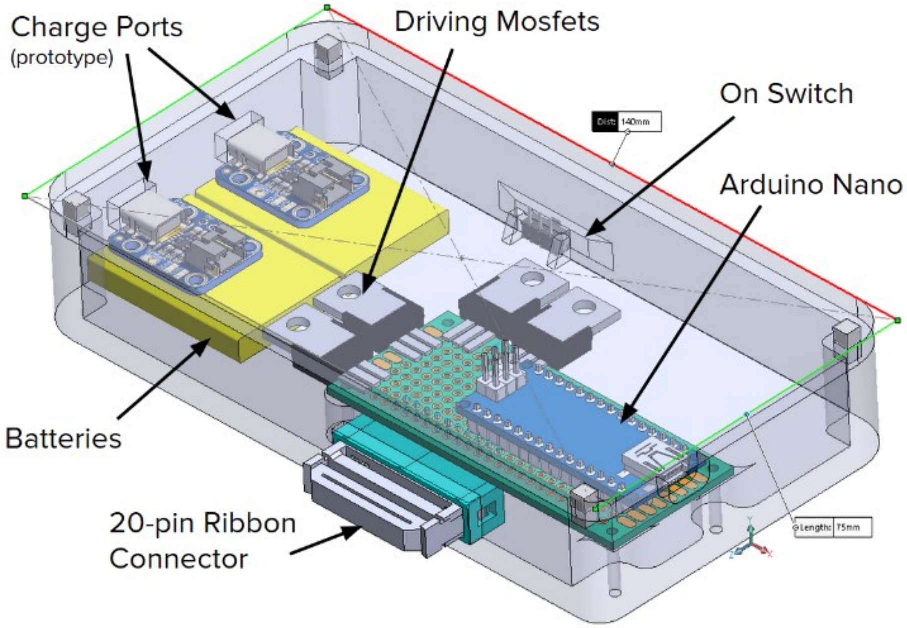

Figure 58: Compact Electrical Components and Housing

The team designed a box to house all electrical components. To follow the theme of magnetics, the lid was held on to the box by four cube magnets at each corner. Inside the box, there were the Mosfets and the Arduino Nano attached to a protoboard. Rechargeable batteries and a on/off switch for the system were also included.

Most connections in the box were to be achieved through wire wrapping. Additionally, to make the box easily attached and detached, all external connections, from the microphones and actuators, would be routed to a 20 pin ribbon connector.

The team had successfully prototyped the box, but due to time constraints and unforeseen circumstances, were not able to complete the assembly of the box.

Table 3: BOM for Haptic Wearable

PART NAME	QTY	UNIT COST	TOTAL COST
Arduino Nano	1	$22.00	$22.00
Diode Rectifier 1A 50V	4	$1.95	$7.80
Lithium Polymer Battery 7.4V	1	$15.95	$15.95
Electret Microphone Breakout	4	$6.95	$27.80
N-Channel Power Mosfet 30A 60V	4	$1.80	$7.20
100 Ohm Resistor	4	$0.10	$0.40
USB Mini-B Cable	1	$3.11	$3.11
Breakout board 1.18" x 2.75"	1	$0.03	$0.03
Headers & Wire Housing 20P R/A 4Wall GLDFL	2	$0.95	$1.90
Headers & Wire Housings 20P IDC Socket	2	$1.81	$3.62
Flat Cables 0.050 20 Cond. 28 AWG Round 1pc = 1ft	2	$0.80	$1.60
Headers & Wire Housings .100" Single Row Screw Machine Socket Strip	8	$1.08	$8.64
Adafruit Accessories Break-away 0.1 2x20-pin Strip Dual Male Header	2	$0.95	$1.90
3Pin LED Connector Kit - includes 20 Sets 3Pin Male Female Plug LED Connector Pigtail, 32.8ft 3Pin RGB Extension Cable Line Wire Cord, 20 LED Strip Clips for WS2812B WS2812 WS2811 LED Strip Light	1	$13.98	$13.98
Ninepeak - 3 Inches Black Sew on Hook and Loop Style, 2 Yards	1	$8.99	$8.99
Holure Men's Cool Dry Compression T-Shirt (Large)	1	$11.98	$11.98
	Total		$136.90

One objective of this project was to provide an accessible alternative assistive device. Because of this, the total prototype cost and Bill of Materials (BOM) is relevant and shown in Table 3. Note that for mass production, material costs would be reduced due to bulk ordering.

6.0. Conclusions and Future Work

The following sections discuss the goals presented in this paper, the primary findings through research and design development, and the impact potential of haptic technology on sensory assistance. Future work for the project is then discussed for further development.

6.1. Conclusion and Impact

The driving goal in this project was to design and fabricate a planar wearable assistive device to enable alternative modes of hearing through haptic vibrations. The resulting device prototype used four planar actuator and four microphones spatially arranged on a shirt wearable to associate audio source directionality to spatial haptic feedback. Magnet and coil-based haptic actuators were selected for their increase frequency performance and electrical safety compared to DEA and Piezoelectric smart material alternatives. The final planar actuator design consisted of a planar spring designed for resonant operation with an excited dome coil geometry to optimize actuator size and force output. The four microphones compared measured audio amplitudes via a microcontroller to assess directionality and trigger the actuators.

Current DHH assistive devices are often costly, dependent of the audio vestibular nerve, and can involve invasive procedures. With further work in this field, haptic technology can enable new options for users with sensory needs. With the system designed in this paper, hard of hearing users may have a new mode of identifying audio safety alerts and audio social cues from their environment. By aligning the system's inputs and outputs in the spatial domain, the haptics can more effectively communicating audio directionality.

6.2. Project Limitations

Due to the COVID-19 pandemic, all courses and project work at Worcester Polytechnic Institute were moved online in order to protect the health of WPI students, faculty and staff, and the surrounding Worcester community. Without access to campus lab resources or the ability to meet in person to collaborate, late-stage project work was limited to simulations, refining code, research, and some test procedures.

A test procedure was created to measure the inertial force output of the actuators, and designed for the equipment available, using a MATLAB strain gauge code, signal generator and oscilloscope. A test procedure to observe the output of the microphones used in the wearable design, to collect data for spectral analysis, was also designed for what equipment was available. This MQP project's advisor, Professor Joe Stabile, was unable to perform these tests however, the team nonetheless reevaluated and devised an algorithm for the spectral analysis after collecting the data in section 3.4.4 as seen in Appendix IV.

One of the MQP team member had access to a 3D printer at home and was able to print the final design of the microphone housings, allowing for the microphones to be tested with the housings on them.

6.3. Future Work

This leaves the team with a list of future work if the project were to be picked up in the future. This included several tasks to complete initially planned work as well as further validate and iterate on the design.

While preliminary wiring of quick-connect interfaces and cutting of ribbon cables was done, the wiring of the microphones, actuators, and microprocessor would need to be completed. This network combined with the proper code to run the device would allow the full network to function together as intended. From there, additional tuning of microphones and troubleshooting would be in order. Additionally, this network would need to be fully integrated into the shirt so the device could be easily worn by the user. As noted in section 5, wire pathing was planned on the shirt. The next step would be to trace pre-planned wire paths to sew the wirings and electronics onto the shirt. This would result in a fully wearable and integrated device. The team also would advise looking into new microphones that better addressed the sensitivity and directionality need of the wearable.

Additional testing of the device would also serve to further validate and improve the design. First, the team had designed testing procedures for the sensitivity and directionality of the microphones. These procedures can be found in Appendix II and should be done to fine-tune the microphone sensitivities. The team would also advise further testing the potential of the actuator spring. Since the device was tuned specifically to ring at precisely the resonant frequency of the spring, the team hypothesized that this may lead to a shorter product lifespan. Therefore, cyclic loading and fatigue analysis would serve to validate the lifespan of the device.

Additional adjustments to the code of the device would also serve to improve device performance. By adding frequency filtering to the code, this would allow the microcontroller to interpret signals more effectively from the microphones with higher accuracy. With the aid of Tahvorn George, a WPI undergraduate student specializing in Signals and Communications and Computer engineering, an Analog comparator circuit design is presented in Appendix I. The work presented there reflects Tahvorn's Major Qualifying Project capstone and was done in collaboration with the project team and advisor.

For manufacturability, a more formal manufacturing process should be devised to more efficiently assembly actuators and improve prototype cycle time. Initial actuator assembly would take two to three team members approximately 30 minutes of hands-on time plus 16 hours of curing time to fully assembly one actuator. A more efficient process would save manufacturers substantial time and money in work hours.

Since there was no exact way to ensure the same results in terms of the same number of turns and precise geometry each time in the manufacturing process of the actuators, the team observed that the resonant frequency of each individual actuator was impacted and varied across the range of 167Hz and 209Hz. Consequently, this influenced the power consumption of the entire system and the team's initiatives of making it more energy efficient. Implementing dynamic tracking in the design to compensate for the variation in resonant frequency often seen in LRAs would remedy this inconsistent performance. This is done by taking advantage of the back-EMF generated by the actuator to determine the resonant frequency that a LRA driver can detect and send to the auto-resonance engine in each cycle. If the frequency is too high, the driver will adjust the output frequency to be lower, or higher, if the frequency is too low. An example of this implementation can be seen in the block diagram of a DRV2605 by Texas Instruments in Figure 59 (Burk, 2013).

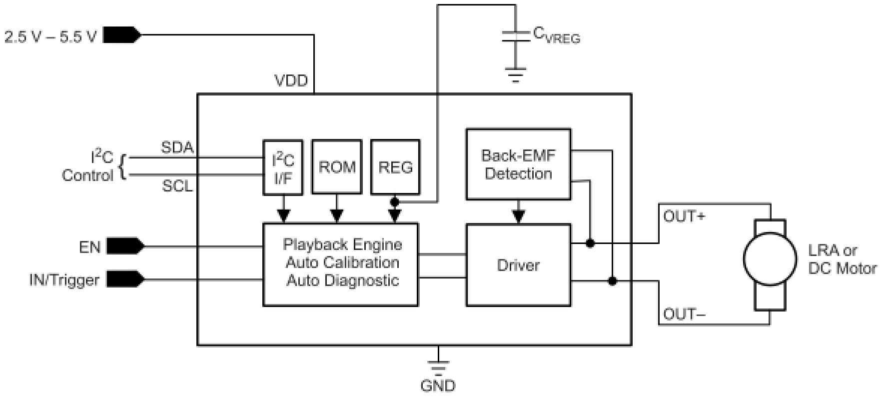

Figure 59: DRV2605 Block Diagram

Replacing the microcontroller and breakout board in the electronics housing with a dedicated, custom-made microchip would also significantly lower the profile of the device.

Rather than having a box roughly the size of a smartphone to hold all the required electronics, the team could replace the box with a smaller microchip and batteries to achieve a more compact product.

References

Angione, F. Novak, C. Imeson, C. et al. (2016). Study of a low frequency emergency siren in comparison to traditional siren technology. *Proceedings of Meetings on Acoustics*, *29*(1) 1-13. https://doi.org/10.1121/2.0000601

Baek, Y., Myung, R., & Yim, J. (2006). Have you ever missed a call while moving? The optimal vibration frequency for perception in mobile environments. *WSEAS Transactions on Communications*, *5*(10), 1981-1985.

Bartlett, B. (1987). Choosing the right Microphone by Understanding Design Tradeoffs. *Journal of Audio Engineering Society, 35*(11) 924-944.

Brochu, P., & Pei, Q. (2010). Advances in dielectric elastomers for actuators and artificial muscles. *Macromolecular rapid communications*, *31*(1), 10-36.

Burk, B. (2013). Benefits of Auto-Resonance Tracking (SLOA188), *Texas Instruments,* 1-9.

Center for Disease Control and Prevention. (2019). *Types of Hearing Loss* https://www.cdc.gov/ncbddd/hearingloss/types.html

De Rossi, D., Carpi, F., Carbonaro, N., Tognetti, A., & Scilingo, E. P. (2011). Electroactive polymer patches for wearable haptic interfaces. *2011 Annual International Conference of the IEEE Engineering in Medicine and Biology Society*, 8369-8372.

Eagleman, D. (2015, March). *Can we create new senses for humans?* [Address]. TEDxVancouverBC, Vancouver, British Colombia, Canada. https://www.ted.com/talks/david_eagleman_can_we_create_new_senses_for_humans?

Eid, M. A., & Al Osman, H. (2015). Affective haptics: Current research and future directions. *IEEE Access*, *4*, 26-40.

European Commission. (2008). Directorate-General for Health & Consumers, Scientific Committee on Emerging and Newly Identified Health Risks. *Green facts: Personal music players & hearing. European Commission, Luxembourg*.

Findlater, L., Chinh, B., Jain, D., Froehlich, J., Kushalnagar, R., & Lin, A. C. (2019). Deaf and Hard-of-hearing Individuals' Preferences for Wearable and Mobile Sound Awareness Technologies. *Proceedings of the 2019 CHI Conference on Human Factors in Computing Systems* 1-13.https://doi.org/10.1145/3290605.3300276

Fragoulis, D. K., & Avaritsiotis, J. N. (2001). A Siren Detection System based on Mechanical Resonant Filters. *Sensors, 1*, 121-137.

Frisoli, A. W. P., & Ryu, J. H. (2012). *Technical Area Overview Report for the IEEE Technical Committee on Haptics*. Technical Report, IEEE Technical Committee for Haptics (TCH): Vancouver, BC, Canada.

Goertz, R. C. (1952). Fundamentals of general-purpose remote manipulators. *Nucleonics*, *10*(11), 36-42.

Gorissen, B., Chishiro, T., Shimomura, S., Reynaerts, D., De Volder, M., & Konishi, S. (2014). Flexible pneumatic twisting actuators and their application to tilting micromirrors. *Sensors and Actuators A: Physical*, *216,* 426-431.

Hitt, R., Punch, J. L., & Smith, S. W. (2019). Hearing loss and Quality of Life, *Journal of Communication Disorders*, (78) 33-45. https://doi.org/10.1016/j.jcomdis.2019.01.001

Hoffmann, R., Spagnol, S., Kristjánsson, Á., & Unnthorsson, R. (2018). Evaluation of an audio-haptic sensory substitution device for enhancing spatial awareness for the visually impaired. *Optometry and Vision Science*, *95*(9), 757.

Instron, (2020). *What is Tensile Testing*? https://www.instron.us/our-company/library/test-types/tensile-test

Jackson, C. W., Wegner, J. R., & Turnbull, A. P. (2010). Family quality of life following early identification of deafness. *Language, speech, and hearing services in schools*. *41*(2), 194-205. https://doi.org/10.1044/0161-1461(2009/07-0093)

Kulkarni, S. (2002). *Frequency Domain and Fourier Transforms*. 1-21. https://www.princeton.edu/~cuff/ele201/kulkarni.html

Laszlo, C. A. (1994). Engineering aspects of assistive device technologies for hard of hearing and deaf people. *Canadian Acoustics 22*(3), 77-8.

Lewis, A. (2018). Back EMF Phase Relationships in Moving-Coil Loudspeakers (Part 2) *Acme Sound, LLC,* 14-17.

Maddern, A. Privopoulos, E., & Howard, C. (2011). Emergency Vehicle Auditory Warning Signals: Physical and Psychoacoustic Considerations. *Proceedings of Acoustics,* 1-5.

Mahamud S., & Zishan S. R. (2017). Watch IT: An Assistive Device for Deaf and Hearing Impaired. *4th International Conference on Advances in Electrical Engineering (ICAEE) Proceedings*, 556-60. https://doi.org/10.1109/ICAEE.2017.8255418

Massie, T. H., & Salisbury, J. K. (1994). The phantom haptic interface: A device for probing virtual objects. *Proceedings of the ASME winter annual meeting, symposium on haptic interfaces for virtual environment and teleoperator systems, 55*(1), 295-300.

Mielke M., Grunewald A., & Bruck R. (2013). An Assistive Technology for Hearing-Impaired Persons: Analysis, Requirements and Architecture. *35th Annual International Conference of the IEEE EMBS,* 4702-4705. https://doi.org/10.1109/EMBC.2013.6610597

Miyazaki, T., Kitazono, Y., & Shimakawa, M. (2013). Ambulance Siren Detector using FFT on dsPIC. *Proceedings of the 1st IEEE/IIAE International Conference on Intelligent Systems and Image Processing,* 266-269. https://doi.org/10.12792/icisip2013.052

National Institute of Deafness and Other Communication. (1997). *Presbycusis* https://www.nidcd.nih.gov/sites/default/files/Content%20Images/presbycusis.pdf

Precision Microdrives. (2015). *Vibration Motors – ERMs and LRAs*. https://www.precisionmicrodrives.com/vibration-motors/vibration-motors-erms-and-lras/

Scola, C. F., & Bolanos Ortega, M. D., (2010). *Direction of arrival estimation – A two microphones approach* [Master's Thesis, Blekinge Institute of Technology].

Senthilvelan, S.; Gnanamoorthy, R. (2006). Damping characteristics of unreinforced, glass and carbon fiber reinforced nylon 6/6 spur gears. *Polymer Testing*, *25*(1), 56-62.

Center for Disease Control and Prevention, (2019). *Types of Hearing Loss*, https://www.cdc.gov/ncbddd/hearingloss/types.html

UCSF Health (2020). "FAQ: Cochlear Implants." UCSF Health. https://www.ucsfhealth.org/education/faq-cochlear-implants

Wang, F. (2014). Haptic Energy Consumption (SLOA194), *Texas Instruments,* 1-17.

Weber, D. (2016). *U.S. Patent No. 9396629B1*. Washington, DC: U.S. Patent and Trademark Office.

World Health Organization. (2020). *Deafness and hearing loss*. https://www.who.int/news-room/fact-sheets/detail/deafness-and-hearing-loss

Yim, J., Myung, R., & Lee, B. (2007). The mobile phone's optimal vibration frequency in mobile environments. *International Conference on Usability and Internationalization*, 646-652.

Mathscinotes. (2016, June 7). A Simple Frequency-to-Voltage Converter, Retrieved from https://www.mathscinotes.com/2014/03/a-simple-frequency-to-voltage-converter/

A Simple Frequency-to-Voltage Converter, (2016, June 7). Retrieved from https://www.mathscinotes.com/2014/03/a-simple-frequency-to-voltage-converter/

Lewis, J. (2013, March 27). Analog and digital MEMS microphone design considerations -. Retrieved from https://www.eetimes.com/analog-and-digital-mems-microphone-design-considerations/#

NIDCD (2017). "Cochlear Implants" National Institute on Deafness and Other Communication Disorders. https://www.nidcd.nih.gov/health/cochlear-implants

De Pietro, MaryAnn (2020). "Does medicare cover hearing aids?" Medical News Today. https://www.medicalnewstoday.com/articles/does-medicare-cover-hearing-aids

Mroz, Mandy (2019). "Hearing aid prices." Healthy Hearing. https://www.healthyhearing.com/help/hearing-aids/prices

Atcherson, R. et al. (2015). "Hearing Assistive and Access Technology." *Plural Publishing.* http://zu.edu.jo/UploadFile/Library/E_Books/Files/LibraryFile_91640_34.pdf

National Research Council (US) Committee on Disability Determination for Individuals with Hearing Impairments (2004). "Basics of Sound, the Ear, and Hearing." *NCBI.* https://www.ncbi.nlm.nih.gov/books/NBK207834/

Appendix I – Analog comparator circuit

The following section is the work of Tahvorn George, a WPI undergraduate student specializing in Signals and Communications and Computer engineering. The work was done in fulfillment of a Major Qualifying Project capstone and was done in collaboration with the project team and advisor.

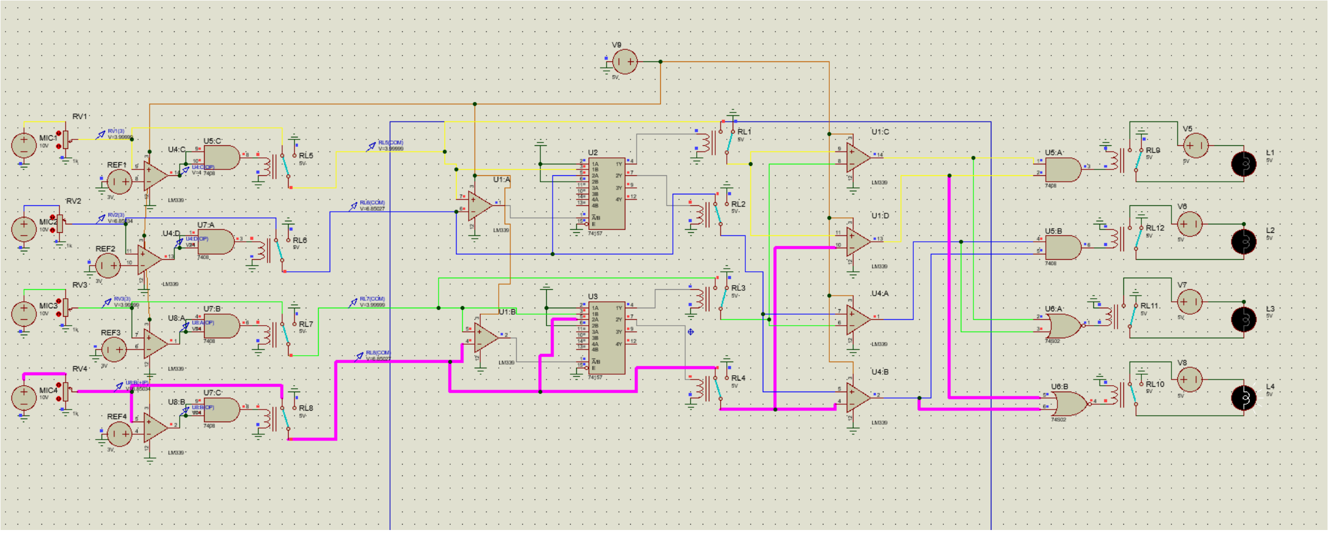

Components list:

Each integrated circuit (IC) was chosen as their supply voltage (2-36V) is within the range of a portable cell, each has low supply current draw and an operating temperature approximately -55C to 125C. Additionally, each IC has both a through-hole and surface mount package in order to use the larger component for proto-board testing and its smaller counterparts for compact PCB design.

LM339

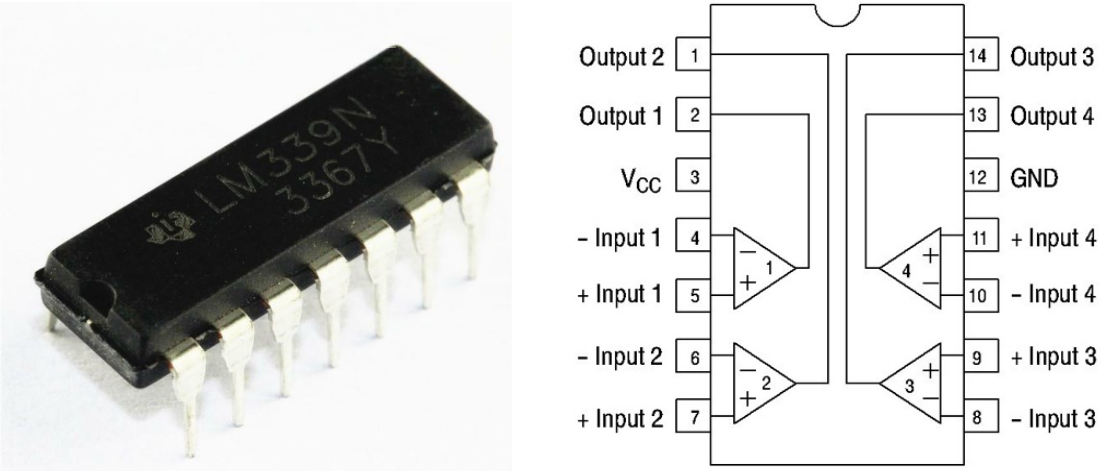

Schematic of LM339

The LM339 is an integrated circuit that houses 4 differential comparators. These comparators will be used to compare different input signals and determine the higher voltage.

LM7408/DM7402

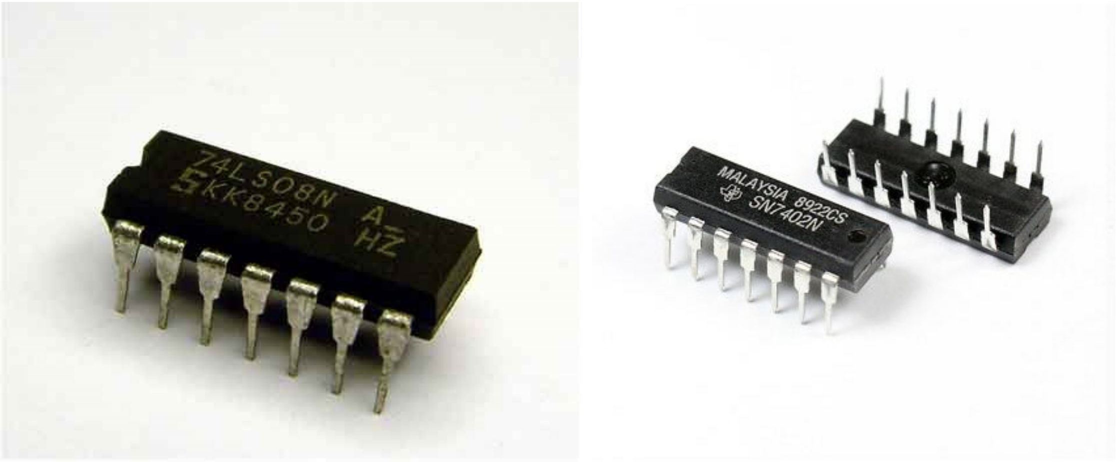

Schematic of logic gate ICs

These ICs are a dual two-input AND gate (7408) and a quad two-input NOR gate (7402). These devices perform logic functions dependent on their inputs and are determined by their truth table depicted below.

AND		
Input		Output
A	B	Y
0	0	1
0	1	1
1	0	1
1	1	0

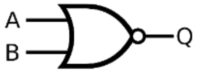

NOR		
Input		Output
A	B	Y
0	0	1
0	1	0
1	0	0
1	1	0

MC74HC157

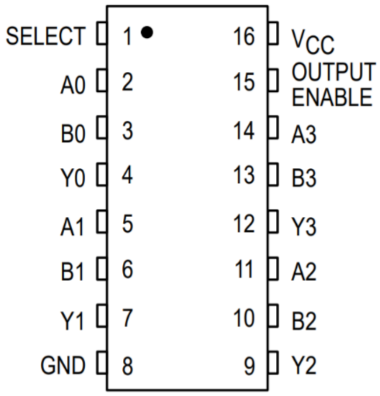

Schematic of logic level Multiplexer

The MC74HC157 is a logic level data selector/multiplexer. This device will be used to select/carry forward the dominant voltage from the comparator circuitry.

Circuit operation

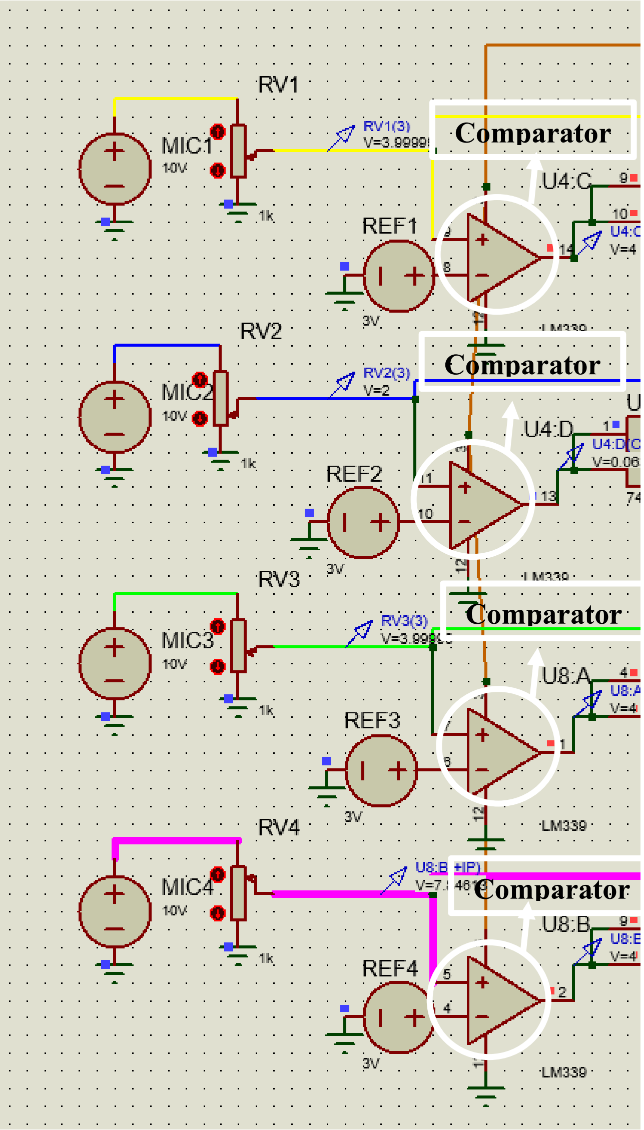

Input threshold section of comparator

In this circuit, the output of the microphones 1-4 (yellow, blue, green and pink) are set to: 3.9V, 2V, 3.9V and 7.8V respectively. MIC4 (the thickest wire, pink) was chosen as the dominant (loudest) microphone.

Beginning at the inputs, MIC1-MIC4 are DC voltage sources with a potentiometer for ease of simulation and voltage control. Each microphone will be connected to a comparator with a threshold voltage of 3V. This threshold voltage was arbitrarily chosen but can be simply swapped with any value depending on the specifications of the microphone. This comparator circuit is used to ensure that only amplitudes above a certain value will be compared. This reduces the chance of any errors that may arise in the system as well as false positives for an actuator to energize.

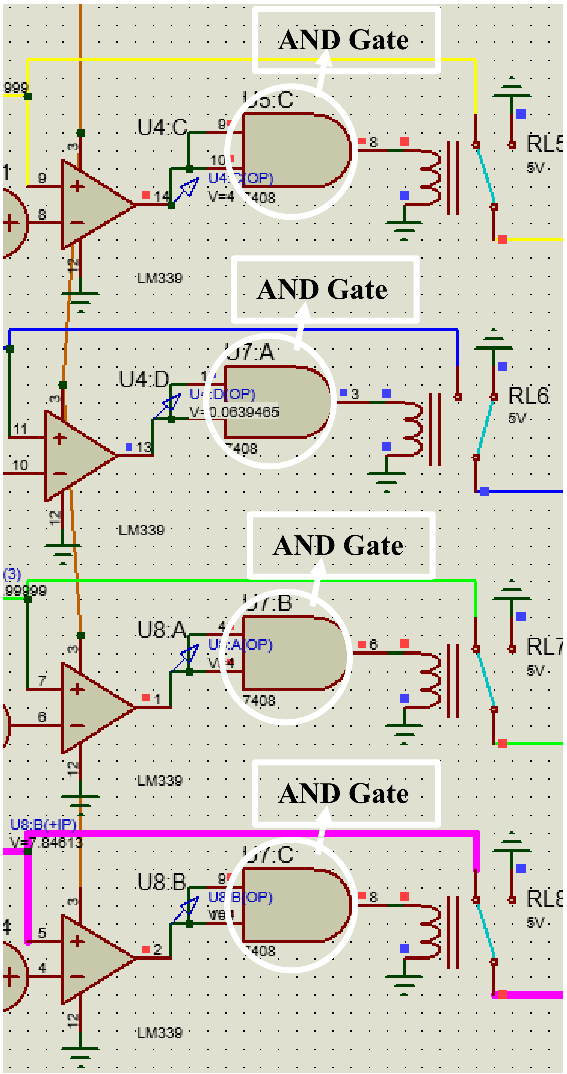

Continuation of input threshold section

Since the output of a comparator is a logic 0V or 5V, the output of the LM339 comparator is connected to inputs A and B of an LM7408 AND gate. If the comparator outputs 5V (i.e the microphone's output is of a desired amplitude), the LM7408 will then activate a relay to carry forward the voltage comparison to a second stage of LM339 circuits.

The results from MIC1 and MIC2 and MIC3 and MIC4 are compared in the voltage comparator U1:A and U1:B respectively. Odd numbered microphones are connected at the non-inverting input and even numbered microphones at the inverting input. If the odd numbered value is larger, the output of U1A/B will be ~5V. If the even numbered microphone is larger, the output of U1A/B will be ~0V.

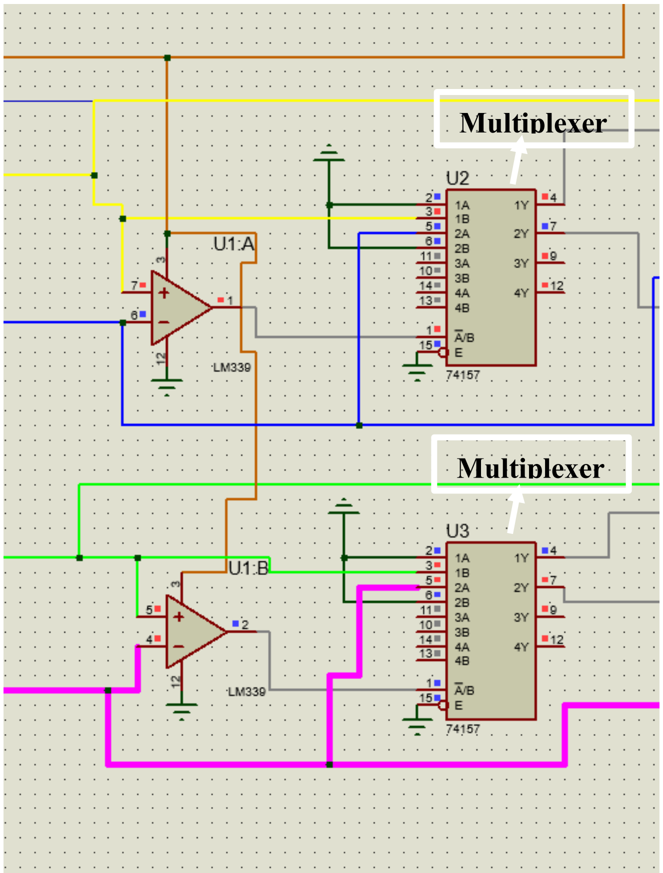

Stage one comparator

The output of the comparators are connected to the select pins (Pin 1/ ~A/B) of 74157 multiplexer, U2 and U3 respectively. If the select pin is ~0V, the multiplexer will output 5V to pin 4/2Y (Once the input of 2A is greater than 500mV, meaning the microphone must be active) and if the select pin was set to 5V, the multiplexer would output 5V to output 1Y (Once the input of 1B is greater than 500mV, meaning the microphone must be active).

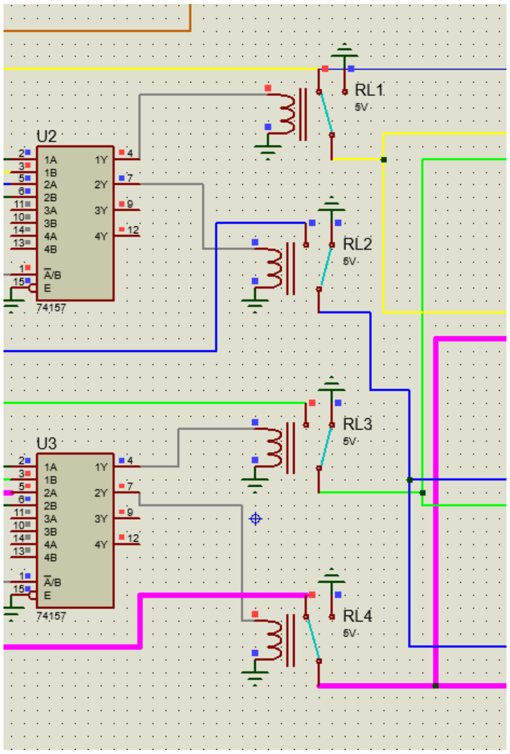

Relay system to carry forward dominant signals

The 5V output of the multiplexer will be used to turn on the corresponding relays to carry forward the dominant signal.

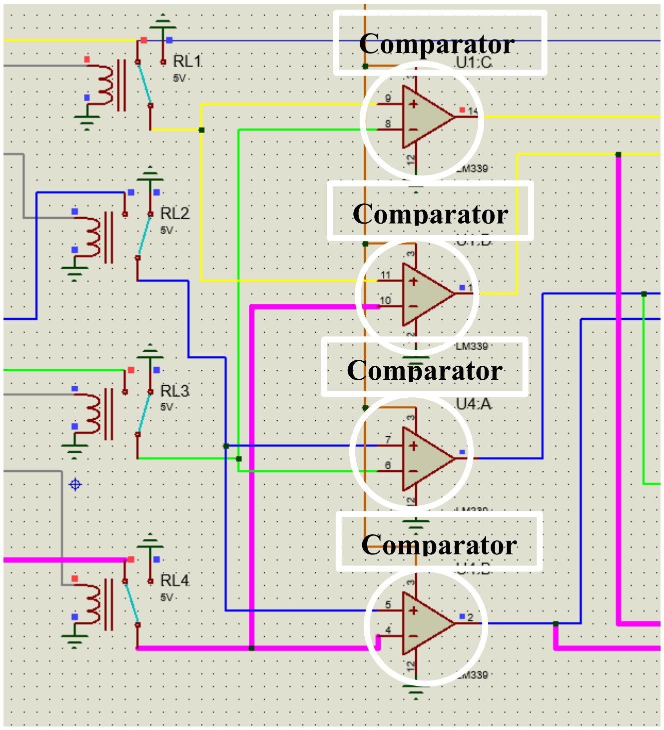

Stage two of comparators

These two winning signals are then carried into a secondary stage of comparators (U1:C & U1:D, U4:A & U4:B) that will be used to compare signals 1&3, 1&4, 2&3, 2&4 respectively with microphones 1 and 2 being on the non-inverting input (If 1 or 2 is higher, output is 5V) and microphones 3 and 4 being on the inverting input (If 3 or 4 is higher, output is 0V).

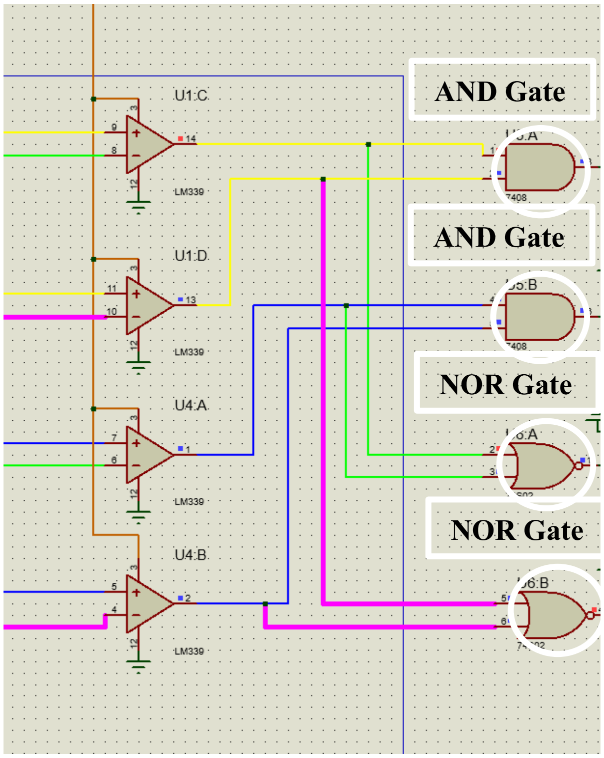

Logic gate check of winning signal

A series of logic gates (2 AND gates and 2 NOR gates) are then used to decode which signal was the winning signal out of all 4 inputs.

The logic tables are as follows (1 = 5V, 0 = GND)

U5:A

U1:C	U1:D	OUT
0	0	0
0	1	0
1	0	0
1	1	1

U5:B

U4:A	U4:B	OUT
0	0	0
0	1	0
1	0	0
1	1	1

U6:A

U1:C	U4:A	OUT
0	0	1
0	1	0
1	0	0
1	1	0

U6:B

U1:D	U4:B	OUT
0	0	1
0	1	0
1	0	0
1	1	0

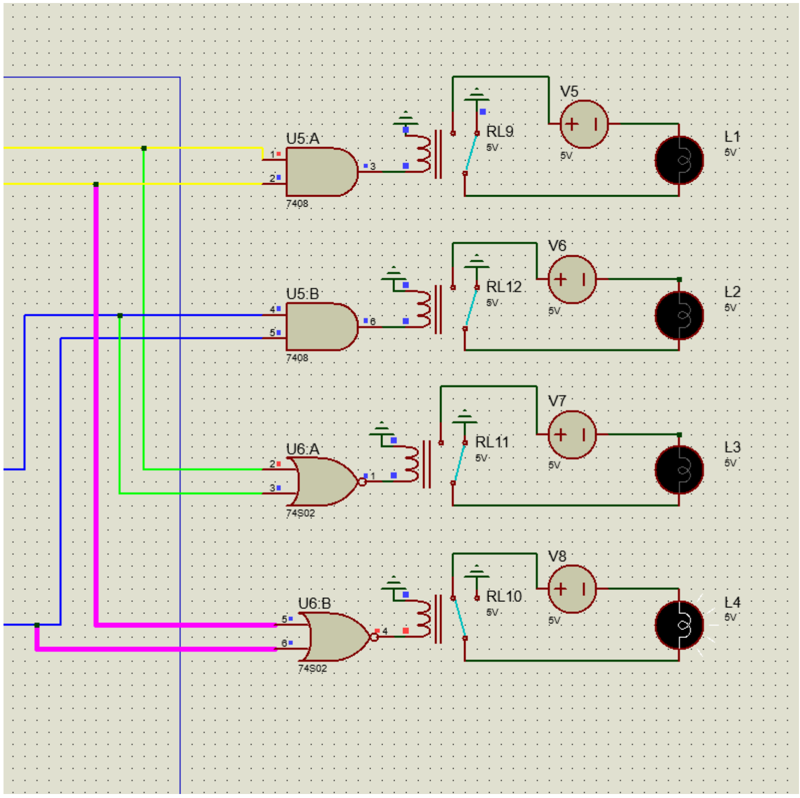

Winning signal turning on corresponding circuit

The output of these logic gates will then turn on a relay to close the actuator circuit (which is being replaced by a lightbulb). Since MIC4's output was the highest voltage at 7.8V, the fourth comparator circuit (comprising of L4) will activate.

Analog Comparator Circuit Recommendations

Some components in this circuit were chosen due to the lack of available components within the simulator. For example, a relay was used as a switching device in this circuit, however, a relay is an electromechanical device that is prone to mechanical failure and magnetic interference. A solid-state relay would be ideal for use in a circuit such as this. A solid-state relay has no moving parts and has a lower current consumption as there is no need to energize a coil to close a contact in a solid-state relay. Also, an analog switch multiplexer may replace the need for a data selector multiplexer and relay/solid-state relay combination. An analog switch multiplexer will output (depending on the select pin) the selected input value rather than a logic value of 5V or 0V, removing the need for a relay system to carry the signal forward (as the analog switch multiplexer performs this task as well), therefore reducing overall power consumption and extending performance time.

Appendix II – Experiment Procedures

Microphone Spectral Analysis

Aim: To observe the output of the microphone, which will be used as input for spectral analysis.

Background: The most common siren signals are in the form of a 'Wail' or 'Yelp.' However, both of these signals have different features such as the range of frequencies and their corresponding amplitudes in regards to sound. The 'Wail' is commonly seen at a frequency of 4.11s at a sound pressure of 130dB whereas the 'Yelp' is commonly seen at a frequency of 0.35s at a sound pressure of 130dB. The average sound pressure of 'noise' in urban environments is around 60dB. An auditory warning signal of 130dB in a noise-rich environment is effective within the range of 8-12m (Skeiber, et al, 1978). As a control, microphone testing and calibration is normally conducted at a 1kHz sine frequency of 94dB at 1 meter distance from the sound source.

Materials:

1. Microphone
2. Arduino (10-bit ADC) Values from 0-1023
3. dB source (link to files are included as hyperlinks in procedure)
4. Decibel meter *(Decibel X strongly recommended. Link to download for iPhone here)*
5. Measuring tape
6. Hearing protection

Procedure:

After uploading the Arduino code to the microcontroller and inputting the MATLAB code, conduct the following procedure:

1. Measure the sound pressure level (SPL) of the room when it is 'quiet'. Record the value.
2. Connect the microphone as shown in the circuit diagram (Figure 14).
3. Measure a distance of 1m between the receiver (microphone) and the source (dB output)
4. Turn on the circuit (Figure 14) and run the program.
5. Emit a 1kHz sine signal to the receiver and record the distance of the source from the system. The signal can be found here.
   (Note: Signal should be turned up to 94db SPL. Wear protective gear.)
6. Listen for 20 seconds.
7. Repeat steps 1 through 6 positioning the microphone at 45°, 90°,135°, 180°, 225°, 270°, and 315° from the sound source.
8. Repeat steps 1 through 6 with this input (Siren Wail)
   (Note: Signal should be turned up to 130db SPL. Wear protective gear)
9. Repeat steps 1 through 6 with this input (Siren Yelp)
   (Note: Signal should be turned up to 130db SPL. Wear protective gear)
10. Repeat steps 1 through 6 with this input (White Noise)
    (Note: Signal should be turned up to 66db SPL. Wear protective gear)
11. Repeat steps 1 through 8 for all inputs at distances 5m, 10m, 15m, 20m.
12. Record data.

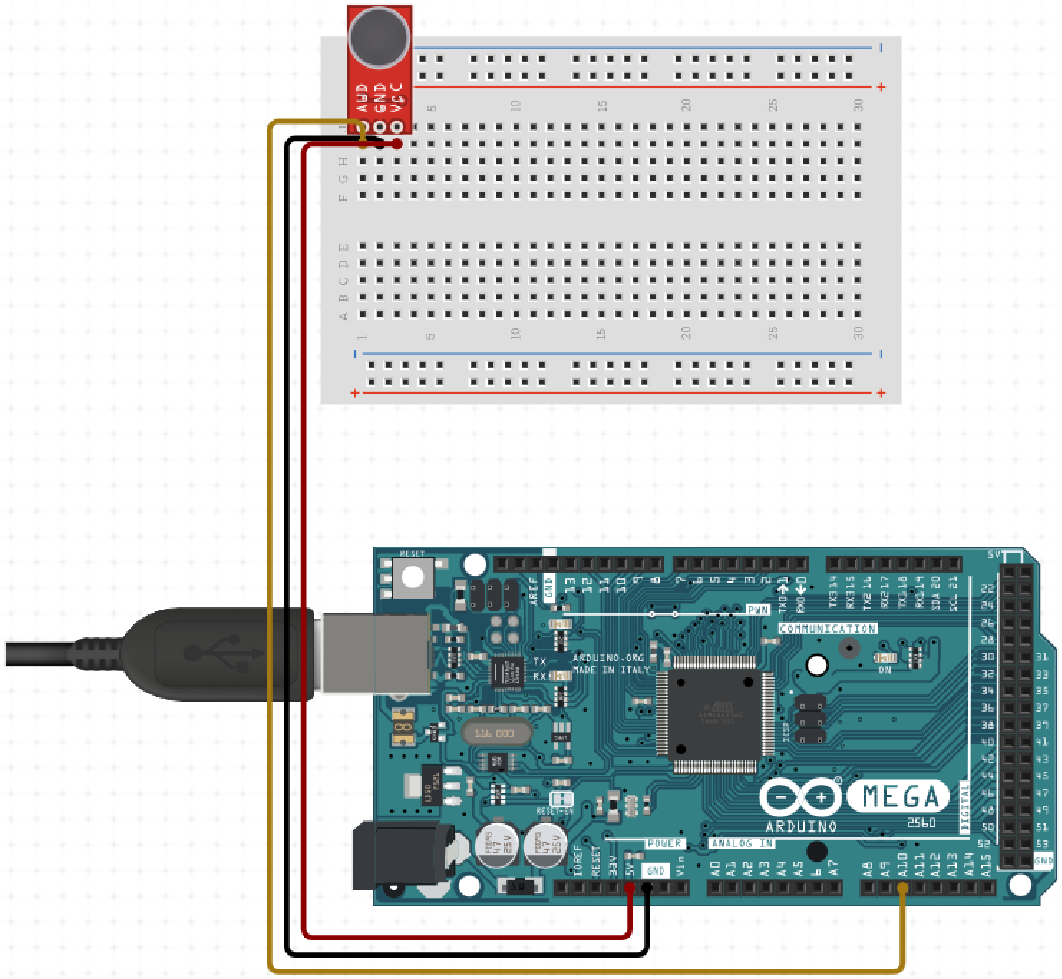

Microphone test set-up

Actuator Force Output Test Procedures

Objective: Measure inertial force output of the actuator per-stroke

Background:

The actuator force amplitude is the inertial force output per stroke. The analysis and calculations expect this force to be around 0.045 N

For adhering the actuator potential methods include: hot-glue / superglue, could put tape on strain gauge bar to prevent damage.

Equipment: Tensile tester, MATLAB & Arduino - Strain gauge,
spring steel actuator, nylon actuator, signal generator, oscilloscope

Procedures:

1. Connect a spring steel actuator to an AC source (signal generator)
2. Set the signal input to the sine wave and the value to 100Hz.
3. Measure the current entering the actuator coils at this frequency such that the current is 0.0215 Amps. (*This simulates the electrical excitation of the 4-actuator circuit with mosfets*)
4. Once the actuator is resonating, adhere the actuator to the end of the strain gauge surface such that the magnet is facing up. The magnet should be the moving component.
5. Setup a frequency excitation sweep between 20 - 500 Hz
    a. *If frequency sweep is not possible, measure at 40Hz, 80 Hz, 165 Hz, 330 Hz, and 500 Hz*
6. Using the strain gauge MATLAB/Arduino code, excite the actuator using the frequency sweep above and record the force output.
7. Measure, read, and record force values to identify the peak force.

Appendix III – Electrical and FEMM Code

Arduino Code for Microphone test:

```
#include <TimerOne.h>

long int i =0;

void setup(){

  Serial.begin(2000000);
  Timer1.initialize(200); // 5 KHz interrupts
  Timer1.attachInterrupt(getValue);
}

void loop(){
}

void getValue() {

    int sensorValue = analogread(0);
    Serial.print(sensorValue);
    Serial.print(" ");
```

MATLAB Code for Microphone test:

```
s = serialport('COM5',2000000);
format longG
t_start = now;
data = read(s,225000,"string");
d_start = datetime(t_start,'ConvertFrom','datenum')
t_end = now;
d_end = datetime(t_end,'ConvertFrom','datenum')

data = split(data);

data_numbers = zeros(75000,1);
for i=1:75000
   data_numbers(i) = str2double(data(i));
end
```

FEMM Dome Optimization Code:

```
disp('Framework adapted from the FEMM Tutorial "Wound Copper Coil with an
Iron Core" by David Meeker');
disp(' ');
disp('axisymmetric magnetostatic problem');
addpath('C:\Programs\femm42\mfiles');
m_OD = 12.7;
m_height = 1.6;
c_height = 1; % (all lengths in mm)
c_ID = 4;
c_OD_min = 20;
c_OD_max = 40;
step = 2;
```

```
MagClear = 2.25;
SpringT = 0.127*1;
Shield = .5;
c_OD = c_OD_min;
figure; hold on;
forcey = zeros(40, 1);
diameterV = zeros(40,1);
while c_OD<=c_OD_max
    openfemm;
    newdocument(0);
    mi_probdef(0, 'millimeters', 'axi', 1.e-8, 0, 30);
    mi_drawrectangle([0 MagClear; (m_OD/2) (MagClear+m_height)]);
    mi_drawline([c_ID/2 (0);c_ID/2 (0-1)]);
    mi_drawline([c_OD/2 (m_height+MagClear-1);c_OD/2 (m_height+MagClear)]);
    mi_drawline([c_ID/2 (0);(c_ID/2+3) (0)]);
    mi_drawline([c_ID/2 (0-1);(c_ID/2+3) (0-1)]);
    mi_addarc((c_ID/2+3), (0), c_OD/2, (m_height+MagClear), 35, 2);
    mi_addarc((c_ID/2+3), (0-1), c_OD/2, (m_height+MagClear-1), 35, 2);
    mi_drawrectangle([0 (MagClear+m_height); (m_OD/2)
(MagClear+m_height+SpringT)]);
    mi_drawrectangle([(c_OD/2-1) (MagClear+m_height); (c_OD/2+2)
(MagClear+m_height+SpringT)]);
    mi_drawrectangle([(c_OD/2-5) (MagClear+m_height); (c_OD/2-3)
(MagClear+m_height+SpringT)]);
    mi_drawarc([0 -35; 0 35], 180, 2.5);
    mi_addsegment([0 -35; 0 35]);
    mi_addblocklabel(2.25,-.5);
    mi_addblocklabel(1,(MagClear/2+1.5));
    mi_addblocklabel(10,10);
    mi_addblocklabel(1,(MagClear+m_height+SpringT/2));
    mi_addblocklabel(c_OD/2,(MagClear+m_height+SpringT/2));
    mi_addblocklabel(c_OD/2-4,(MagClear+m_height+SpringT/2));
    muo = pi*4.e-7;
    mi_addboundprop('Asymptotic', 0, 0, 0, 0, 0, 0, 1/(muo*0.2), 0, 2);
    mi_selectarcsegment(200,0);
    mi_setarcsegmentprop(2.5, 'Asymptotic', 0, 0);
    mi_addmaterial('Air', 1, 1, 0, 0, 0, 0, 0, 1, 0, 0, 0);
    mi_getmaterial('30 AWG')
    mi_getmaterial('N40')
    mi_getmaterial('Carbon steel forgings, annealed')
    Amps=0.0251; %Amps
    c_30AWG_OD = 0.254;
    width = ((c_OD-c_ID)/2);
    turns = (c_height/c_30AWG_OD)*(width/c_30AWG_OD);
    CoilLabel=sprintf('iCoil: %4.2fA Turns', Amps);
    mi_addcircprop(CoilLabel, Amps, 1);
    mi_selectlabel(1,(MagClear/2+1.5));
    mi_setblockprop('N40', 0, 1, '<None>', -270, 0, 0);
    mi_clearselected
    mi_selectlabel(2.25,-.5);
    mi_setblockprop('30 AWG', 0, 1, CoilLabel, 0, 0, turns);
    mi_clearselected
    mi_selectlabel(10,10);
    mi_setblockprop('Air', 0, 1, '<None>', 0, 0, 0);
    mi_clearselected
    mi_selectlabel(1,(MagClear+m_height+SpringT/2));
    mi_setblockprop('Carbon steel forgings, annealed', 0, 1, '<None>',0,0,0);
```

```
    mi_clearselected
    mi_selectlabel(c_OD/2,(MagClear+m_height+SpringT/2));
    mi_setblockprop('Carbon steel forgings, annealed', 0, 1, '<None>',0,0,0);
    mi_clearselected
    mi_selectlabel(c_OD/2-4,(MagClear+m_height+SpringT/2));
    mi_setblockprop('Carbon steel forgings, annealed', 0, 1, '<None>',0,0,0);
    mi_clearselected
    mi_zoomnatural
    mi_saveas('coil.fem');
    mi_analyze
    mi_loadsolution
    mo_selectblock(2.25,-.5);
    coil_F.r = mo_blockintegral(11);
    coil_F.z = mo_blockintegral(12);
    mi_clearselected
    fprintf('Force on %f1 mm OD Coils (%f2 Turns) is F.r=%f2 N and F.z=%f3
N',c_OD,turns,coil_F.r, coil_F.z);
    disp(' ');
    coil_F.z_plot(c_OD) = mo_blockintegral(12);
    i=1;
    for i = 1:40
        if (forcey(i,1) == 0)
            forcey(i,1) = coil_F.z_plot(c_OD);
            diameterV(i,1) = c_OD;
            break
        end
    end
    disp(forcey)
    coil_F.z_plot(c_OD)
    c_OD = c_OD + step;
end
f=fit(forcey,diameterV,'poly2');
disp(f)
for j = 1:40
    x(j) = j;
end
disp(diameterV)
dydx = diff(forcey) ./ diff(diameterV);
disp(dydx)
dydx2 = [ dydx; 0];
plot(diameterV,forcey,'*','LineWidth',3)
plot(diameterV,dydx2,'LineWidth',3)
title('Dome Coil OD Optimization')
xlabel('Coil Outer Diameter (mm)')
ylabel('Z-Force (N)')
hold off
vals = mo_getcircuitproperties('icoil');
L = vals(3)/vals(1);
fprintf('The self-inductance of the coil is %f mH\n',L*1000);
closefemm
```

Appendix IV – Future Work for Spectral Analysis

1. Sample the sound pressure through microphones with sampling frequency equal to 3200 Hz in order to abide by the Nyquist sampling rate, which is equal to two times the highest frequency of the input signal to be depicted, since there is a possibility that the harmonic is going to be located up to 1600Hz for the 'Wail' and 'Yelp' siren signals without the "Rumbler" configuration.

2. Sample 64 values and thereby, apply a 64-point FFT (Total sampling period = 20ms since 64*(1/3200)). The amplitudes and phases will be obtained about each 50Hz bandwidth (3200/64).

   The bandwidth is derived from the following equation:
   Bandwidth = sampling rate/number of points of FFT

3. 32 amplitudes can be obtained from the 64-point FFT and stored, since in

4. 3200 Hz window, the resulting spectrum of the FFT is symmetrical about the halfway point of that window.

5. Perform this action 16 times with a sampling frequency of 3.125 Hz. Then, perform a 16-point FFT for each of the 32 pitch frequencies from the initial frequency spectrum obtained by the 64-point FFTs, with the input signal being the 16 amplitudes that were calculated for each frequency value.

6. Consequently, the amplitudes and phases of amplitude change can be obtained about each 0.1953125 Hz bandwidth (3.125/16). By using the obtained numerical values, determine whether the input sound is the sirens you would like to detect ('Wail' and 'Yelp' signals) by looking at the amplitudes and phases of amplitude change for each pitch frequency. The figure below displays the overall processing method that was described.

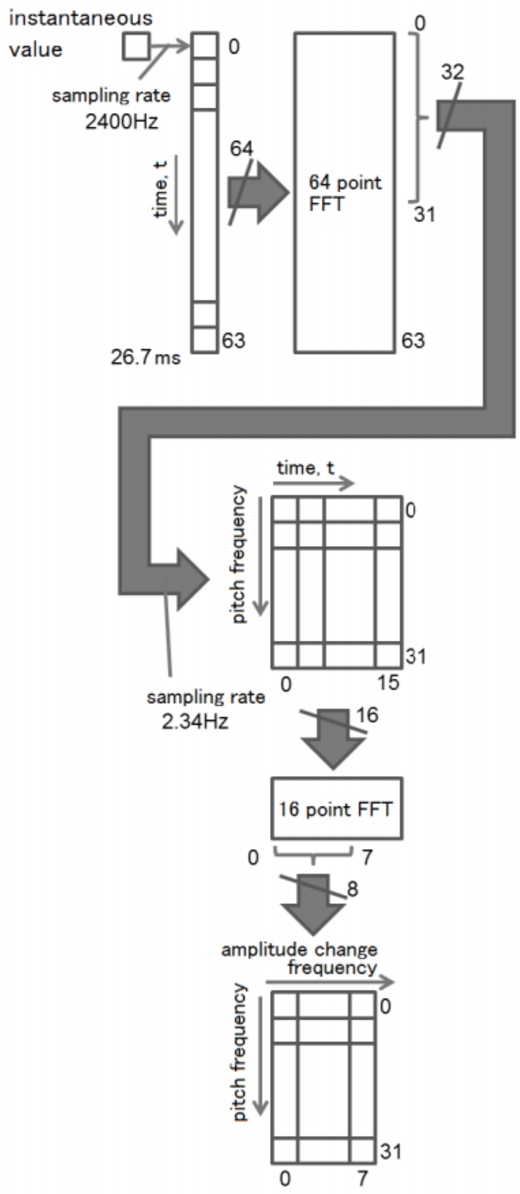

Figure 60: Flow of Analyzing Periodicity